UNIVERSITÀ DEGLI STUDI DI VERONA

DEPARTMENT OF

Diagnostic and Public Health

GRADUATE SCHOOL OF

Natural Sciences and Engineering

DOCTORAL PROGRAM IN

Nanoscience and Advanced Technologies

XXXV CYCLE

CZTS-based photovoltaic devices by non-vacuum techniques

S.S.D. CHIM/03

Coordinator: Prof. Adolfo Speghini

Academic Tutor: Prof. Alessandro Romeo

Industrial Tutor: Dott. Luigi Guerrini

Doctoral Student: Dott.ssa Solidea Zanetti

CZTS-based photovoltaic devices by non-vacuum techniques.

Solidea Zanetti

PhD Thesis

Verona 2023

A scientist in his laboratory is not a mere technician: he is also a child confronting natural phenomena that impress him as though they were fairy tales.

Marie Curie

ABSTRACT OF DISSERTATION

The primary benefit of thin-film photovoltaic devices is that they require less active material, a secondary benefit is that they are ideally suited for the creation of large modules. Last but not least they allow, if a flexible substrate is provided, to fabricate light-weight, flexible and foldable modules. These qualities provide them a guaranteed path to lowering the €/W cost of PV modules, and if they attain high efficiencies, they will be able to obtain a sizable market share.

The copper-indium-gallium-selenium alloy $CuInGaSe_2$ (CIGS) thin-film technology has the highest conversion efficiency (above 23%), but its industrial development could be restricted by the current rate of global indium production.

A possible rival to current solar cell technology is the Cu_2ZnSnS_4 (CZTS) solar cell. The CZTS's absorption coefficient is on the order of 10^4 cm^{-1}: the straight band gap is within the 1.0-1.5 eV region which is ideal for solar cells. One micrometre thick film may effectively function as photocurrent generator and absorb nearly all of the photons in the solar spectrum. As a result, the cost of a solar cell's material can be significantly decreased by utilizing elements that are abundant on Earth. Making a CZTS film involves several different processes, including spray deposition of the precursor and subsequent sulfurization, or reactive co-evaporation, or precursor evaporation and subsequent sulfurization, or spray pyrolysis, or co-sputtering, or PLD (pulsed laser deposition), or sol-gel, or spin coating, or and electrodeposition and so on.

This thesis details several investigations into the effects of CZTS manufacturing settings (by non-vacuum processes), such as drying time and annealing temperatures and, on the structure and optical characteristics.

In the first chapter the project is presented, with also a brief introduction to renewable energy, the physical principles of how a photovoltaic cell work and the structure of kesterite. Chapter II introduces different strategies for the preparation of CZTS based solar cells.

The third chapter illustrates the several characterisation techniques applied in this work. The subsequent chapters present the results of extensive research on the synthesis, characterization, and optimization of kesterite thin films and their application as absorber layers in photovoltaic devices. The study covers various aspects such as deposition techniques, post-deposition treatments, device fabrication and optimization, and analyses the impact of these factors on the photovoltaic performance of finished solar cells.

Drying time and annealing temperature was shown to affect the stoichiometry and the morphology of the compound, generating secondary phases. This strongly influences the final efficiency of the devices and the behaviour under accelerated stability test.

The present thesis provides a contribution in the understanding of low-cost non-vacuum preparation of kesterite absorbers.

We obtained a final efficiency of 7.1% by doping with germanium, and over 8% with a doping solution of cadmium (this result is under patent approval).

Acknowledgment

The PhD thesis work is one of the most challenging, because it is the result of a training course in which one chose to personally put oneself on the line. It is with a heart full of gratitude that I write this acknowledgement for my PhD thesis. The journey of obtaining a PhD is a long and arduous one, but I am so grateful for the support and encouragement that I have received from each along the way.

First and foremost, I want to express my immense gratitude to Isopan and Manni Group for providing me with the resources and opportunities to conduct my research. Your unwavering support and encouragement have been greatly appreciated, and I am so grateful for the opportunities that you have provided me. I want to thank Giuseppe Manni, an enlightened entrepreneur who quietly wrote important pages of philanthropy in Italy and worldwide, a supporter of research and development.

Thank you to Doctor Enrico Frizzera for this great opportunity for personal growth. I'm also grateful to Doctor Luigi Guerrini and Ing. Rocco Traini, two pillars of Isopan S.p.a., for believing in me and encouraging me to embark on this path of higher education.

I want to extend my sincerest thanks Professor Alessandro Romeo. Your guidance, support, and encouragement have been instrumental in shaping my research and ensuring the success of my PhD journey. Your expertise in the field and insightful advice have been invaluable, and I am so grateful for the opportunities that you have provided me. Thank you to all the LAPS laboratory for their assistance at every stage of the research project and for welcoming me: Elisa Artegiani, Prabeesh Punathil, Narges Torabi.

To my parents, I want to say thank you for being my constant source of support and encouragement. Your love and support have been a source of strength during the most challenging moments of my PhD journey and

for my life, and I am so grateful for everything that you have done for me.
I want to thank Luca for his unwavering support and encouragement. Your support has meant the world to me in the last 9 years, and I am so grateful for everything that you have done and you do for me every day.
Thanks to my family, uncles and cousins who never left my life and who believed in me: Mirko, Bea, Fabiola&Sisters, Christian.
Thanks to Fabiano for the logo and for being my disinterested friend for so long.
Thanks to my lifelong friends: Giulia, Lara, Elena, Cristina, Francesca Stefano and thanks to new friends like Alessia with whom I shared the joys and sorrows of this experience.
I also want to express my gratitude to my company colleagues: I appreciate your camaraderie, support, and encouragement, and I am so grateful for the positive impact that each of you have had on my life: Chiara&Marco, Daniela, the laboratory guys and the production colleagues, Olga, Elisa e Oli.
This thesis would not have been possible without the support and guidance of each of you. I am so grateful for everything that you have done for me, and for the positive energy you have given me.

The center for technological platforms (CPT) at the University of Verona, in the person of Dr. Marco Giarola, is thankfully acknowledged for Raman and XRD measurements. Dr. Edmondo Gilioli at IMEM (CNR) Parma, is thankfully acknowledged for the thickness measurements. Dott. Lorenzo Arrizza at the Microscopy Centre of the University of L'Aquila is thankfully acknowledged for the EDXS/SEM measurements. Mr. Paolo Bernardi at the Department of Neurosciences, Biomedicine and movement Sciences is thankfully acknowledged for SEM measurements.

Contents

Chapter I

Chapter II

Chapter III

Chapter IV

Chapter V

Chapter VI

Chapter I
Introduction

1.1 The project

In June 2018 Isopan S.p.A. started a collaboration and a research project with Professor Alessandro Romeo and his LAPS laboratory (Laboratory for photovoltaics and solid-state physics).
The aim of the project was the fabrication of photovoltaic cells to be applied on the insulating panels produced in Isopan; the PV cells will be based on an alternative non-toxic absorber material. Kesterite class of materials, based on Cu-Zn-Sn-S/Se, has been identified as one of the ideal candidates for thin-film solar cells.

Given the preliminary state of research and the variety of materials and approaches available, the ultimate goal of the project is to arrive at the fabrication of a thin-film photovoltaic cell based on the Cu_2ZnSnS_4 (CZTS) compound, a much-studied material that has already yielded good results and fewer safety problems than similar compounds.

1.2 Isopan and Manni Group

Isopan S.p.A. is a company that is part of the Manni Group holding company, together with Manni Sipre, Manni Inox, Manni Energy and Manni Green Tech; it is a leader in Italy in the production of insulated metal panels with high thermal insulation power for walls and roofs on the main national and international markets.

Figure 1. Manni Group Headquarter in Verona.

These panels are often referred to as sandwich panels, since they are composite materials made up of a layered structure consisting of a single or double load-bearing sheet of thin metal materials (usually steel or aluminium), with high resistance (called skins or faces), with a central insulating material called core and consisting of rigid polyurethane foam or mineral wool in between. Thanks to their composition, these structural elements guarantee lightweight but at the same time rigid and resistant products and show good thermal and acoustic insulation as well as good fire and weather resistance.

Figure 2. A sandwich panel.

These properties make them suitable for use in industrial, civil, commercial, livestock and cold logistics construction.

The company has been present on the Italian territory since the 1980s with two production plants, one in Verona (Trevenzuolo) and one in Frosinone (Patrica); over the years it has expanded its market also thanks to the inauguration of new international offices in Spain, Romania, Germany and in 2015 in Russia and Mexico. The company's future is designed and thought using three drivers, the main protagonist being sustainability. Sustainability refers to a method of conducting business that allows for growth in accordance with the social and environmental context in which we operate. Our chance to contribute to the battle against climate change and the shift to a circular economy model, in which suppliers are also participating, is made possible by our ongoing market presence. The company advocates for an industrialisation that is more inclusive to use resources more effectively and have a smaller negative impact on the environment. Scientific research expenditures encourage advancement along the whole manufacturing chain, resulting in goods with minimal environmental impact and low carbon emissions. The intention is to employ more secure and healthful materials[1]. By examining light absorption and carrier collection in thin-film PV systems, this dissertation advances the objective of ubiquitous, cost-effective solar energy utilization.

1.3 A question of Energy

What has been happening climatically in the world in recent years is there for all to see. The rapid melting of glaciers resulting in catastrophes, rising global temperatures in both summer and winter and increasingly frequent fires are upsetting the balance of nature and increasing the risk of extinction of many forms of life on Earth, as well as disrupting human life.

The main cause of this drastic climate change has been identified as the increase in heat-trapping greenhouse gases in the atmosphere; the level of CO_2 in the atmosphere continues to rise, reaching a new record in 2019. Electricity generation and the burning of fossil fuels have contributed to the increase in global emissions: unfortunately, most electricity is still generated by burning coal, oil or gas, producing

carbon dioxide and nitrogen oxide, among the most powerful greenhouse gases that envelop the Earth and trap heat[2].

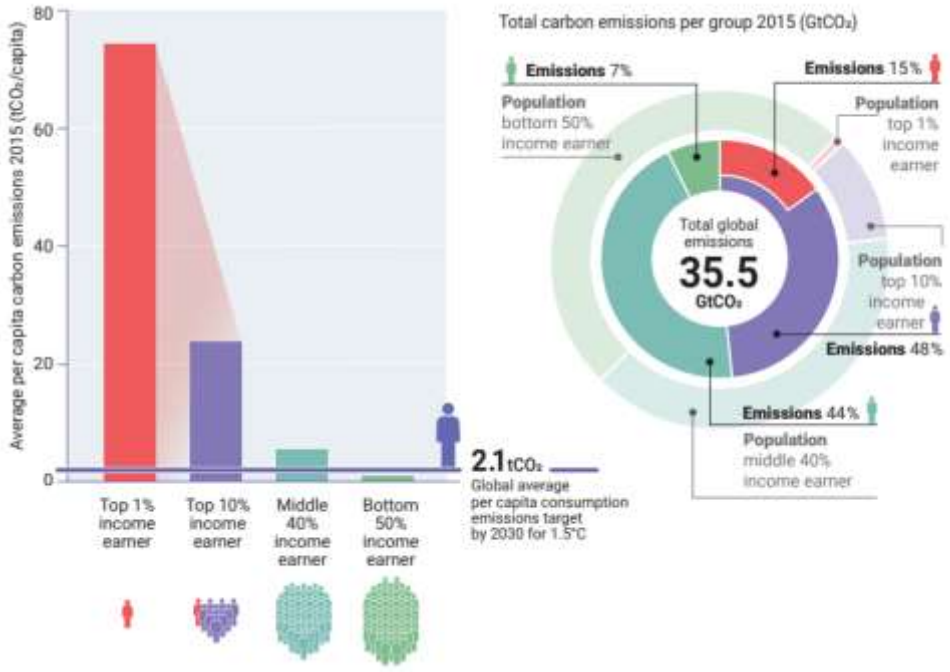

Figure 3. Carbon emissions per group.

[3]

The lifestyle of each of us has a big impact on our planet and the UN's Campaign for Individual Action promotes fundamental actions that each of us should follow to help limit global warming as climate change is not reversible. The 2030 Agenda is an important milestone for sustainable development; it has been adopted by all member countries of the United Nations and sets targets in 17 areas, goals to be achieved by 2030. Sustainable and renewable energy is one of those goals[4]

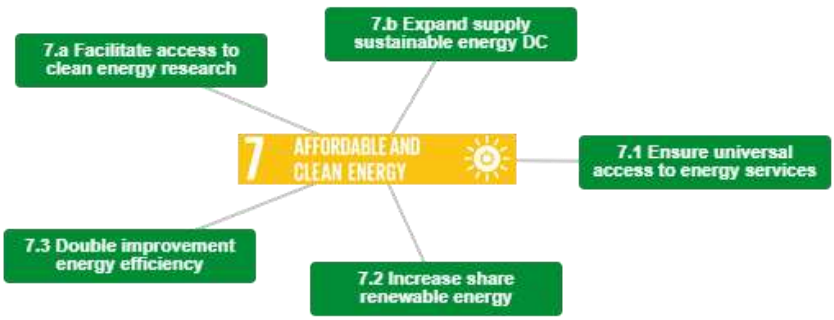

Figure 4. Sustainable development goals from the agenda 2030.

1.4 Renewable energies and photovoltaic

Renewable energies are obtained from inexhaustible natural sources and generate clean electricity without contributing to climate change.

Renewable energy is crucial for being able to reduce the amount of CO_2 that we are pumping into the atmosphere and in the oceans to be able to mitigate dangerous levels of climate change. Climate change mitigation is a huge concern for governments around the world and with ever-increasing energy demand, especially in newly industrialized countries, we need to look for different ways of producing energy that is sustainable for future generations.

Globally, both economic activity and energy demand in 2021 exceed 2019 levels (+1.3% and +0.4%, respectively), and the CO_2 rebound in 2021 (+5.9%) more than offsets the decline in 2020 (-4.9%). In Europe, energy inflation is reaching unprecedented levels in 2022, with the Ukrainian war adding pressure to already tight markets[5].

The energy system has been radically transformed since the industrial revolution. This can be clearly seen from the graph shown here, which graphically represents global energy consumption since 1800.

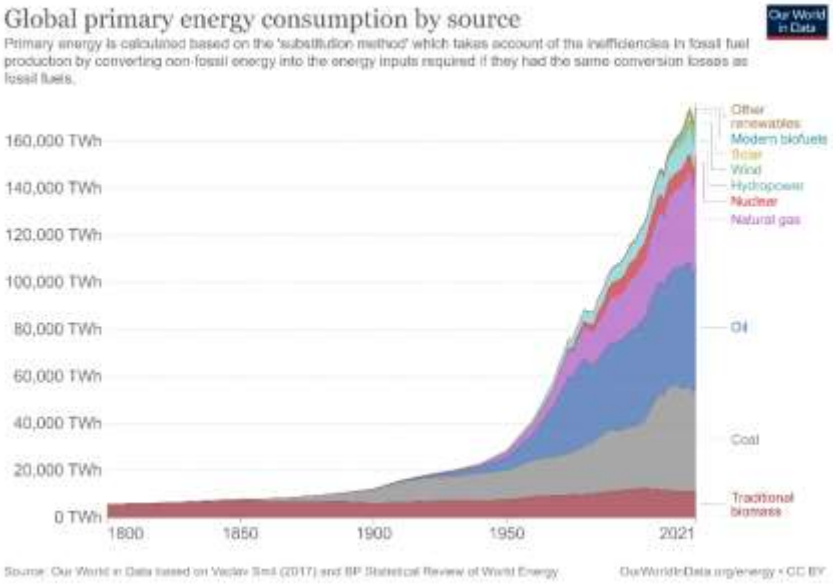

Figure 5. Global primary energy consumption by source.

Demand for energy is growing in many countries around the world as people become wealthier and populations increase.

If this increase in demand is not offset by improvements in energy efficiency elsewhere, our global energy consumption will continue to grow year by year. Growing energy consumption makes the challenge of shifting our energy systems from fossil fuels to low-carbon energy sources more difficult: new low-carbon energy must meet this additional demand and seek to replace existing fossil fuels in the energy mix.

According to the Energy Information Administration, Renewable Energy Sources are defined as fuels that can be easily made or "renewed." We can never use up renewable fuels.

Solar energy is mostly used for heating. Alternatively, solar photons can be used to generate charge carriers in semiconductor junctions and generate electricity directly, i.e. solar cells, or to realise the photochemical or photoelectrochemical production of hydrogen by splitting water molecules. Substantial progress in the development of different type of solar cells has reduced the costs of photovoltaic energy, which are competitive with those of energy produced by burning fossil fuels. Clean energy production supports environmental sustainability and helps societies become more self-sustainable.

1.5 The physics of solar cells

The bulk of solar cells, as well as most other electronic devices like lasers and bipolar junction transistors, are built on p-n junctions. The development of the transistor in the late 1940s and early 1950s resulted in a large portion of the theory of solid-state semiconductors. A voltage or current applied to a material in one area of the device can vary the conductivity significantly in another area of the device. Solar cells are simply huge diodes that have been tuned to absorb light, and they are based on p-n junction devices. The family of bipolar junction devices, which also comprises diodes and bipolar junction transistors (BJTs), contains solar cells as a result [6].

A current source and a rectifying diode connected in parallel can be used to mimic an ideal solar cell. A diode is an electrical component having two terminals that exclusively conducts electricity in one direction. A perfect diode will have infinite resistance in the

opposite direction and zero resistance in one direction; the most prevalent kind of diode is a semiconductor diode.

Semiconductor materials are fundamental for the physics of solar cells, they belong to different groups of the periodic table; their properties in fact depend on their atomic structure and change from group to group. Semiconductors can also be a combination of elements from different groups of the periodic table, generally from group IV or the result of a combination of atoms from groups III and V (the III-V semiconductors), or combinations of atoms from groups II and VI (the II-VI semiconductors).

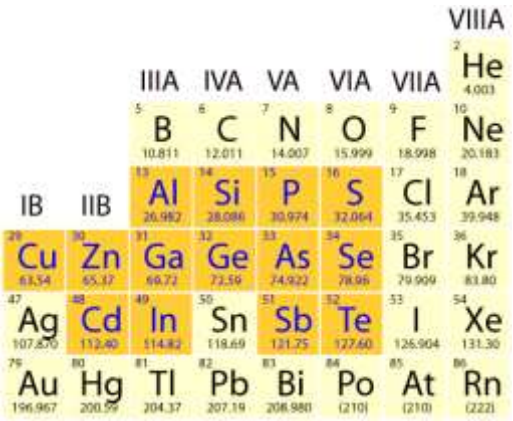

Figure 6. Semiconductor elements on the periodic table.

The most common elements for semiconductor materials are shown in blue. A semiconductor can be of a single element, such as Si or Ge, a compound, such as GaAs, InP or CdTe, or an alloy, for example as $Si_xGe_{(1-x)}$ or $Al_xGa_{(1-x)}As$ (x is the fraction of the particular element its ranges is from 0 to 1) [7].

The simplicity with which conductivity may be altered gives semiconductors a wide range of uses. While the impurity concentration may be very low, on the scale of parts per billion, the addition of even very small quantities of impurities, also known as dopants, can modify the material conductivity by orders of magnitude [6].

Covalent bonds originate between atoms of the same element or among atoms of different elements with comparable outer-shell electron configurations. Each electron spends approximately the same amount of time on each nucleus; both electrons, however, spend the majority of their time between the two nuclei, both nuclei's force of attraction for electrons maintains the two atoms together. Because electrons are trapped in their respective structures at low temperatures, they are not available for

conduction. Thermal vibrations may disrupt covalent bonds at higher temperatures; when a bond is broken or partially broken, a free electron can participate in current conduction. An electron deficiency remains in the covalent bond; this deficiency may be supplied by one of the adjacent electrons, resulting in a change in the position of the deficiency. As a result, we may think of this loss as a particle identical to an electron; this imaginary particle is called "hole"; it has a positive charge and goes in the opposite direction as an electron under the influence of an applied electric field. As a result, the electron and hole both contribute to the overall electric current. A hole is comparable to the notion of a bubble in a liquid [8].

The least amount of energy needed to liberate an electron from its bound state and into a condition where it may conduct electricity is known as a semiconductor's band gap. A "band diagram" is a representation of the band structure of a semiconductor, which displays the energy of the electrons on the y-axis.

The energy difference between the bound state and the free state, or between the valence band and conduction band, is known as the band gap energy (E_G).

The electron is free to roam about the semiconductor and take part in conduction once it has been promoted into the conduction band.

Yet, an extra conduction process will also be possible when an electron is excited into the conduction band: an electron-free area is left behind when an electron is excited to the conduction band. It is possible for an electron from an adjacent atom to enter this open position. This electron moves, leaving an empty place [9].

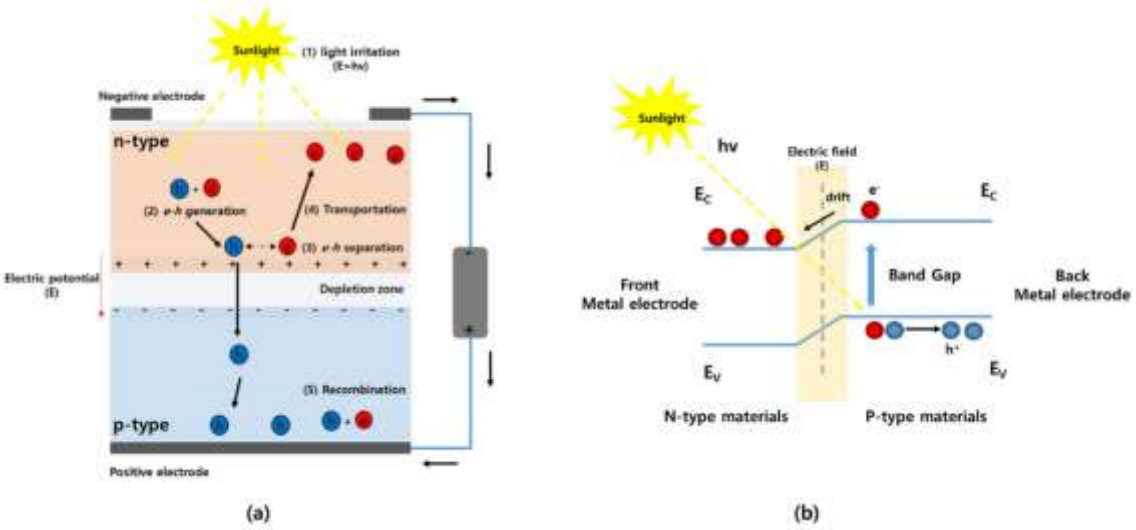

Figure 7.Schematic representations of a p-n junction (a); formation of a depletion region (b).

It seems as though a positive charge is traveling across the crystal lattice due to the space left behind by the electrons, which permits a covalent bond to pass from one electron to another [9].

Free carriers are produced in both bands because of the thermal excitation of a carrier from the valence band to the conduction band. The intrinsic carrier concentration, abbreviated n_i, is the quantity of these carriers. Intrinsic material is semiconductor material that hasn't had impurities introduced to it to alter the carrier concentrations. The band gap and temperature of the material both influence this quantity of carriers. The intrinsic carrier concentration will rise as the temperature rises because it increases the likelihood that an electron will be excited into the conduction band: this directly relates to the effectiveness of solar cells.

By "doping" a crystal lattice with additional atoms, it is possible to change the ratio of electrons and holes in the structure. The creation of "n-type" semiconductor material involves the usage of atoms with one additional valence electron.

When a p-doped semiconductor and an n-doped semiconductor are in contact they form a *p-n junction* [10]. Thus, by combining suitable semiconductors with n-type and p-type properties, interfaces can be created [11]. A solar cell's ability to function depends on the light being absorbed and the creation of an electron hole pair. [6].

The charge inside the crystal, the electric field it produces, and the electric potential it creates are all related by Poisson's equation. This is represented by this equation:

$$-\frac{d^2\varphi}{dx^2} = \frac{dE}{dx} = \frac{\rho}{\varepsilon}$$

Where ρ is the charge density in the crystal and ε is an intrinsic property of the material (measure of the resistance to the electric field, the permittivity).

This ionized acceptor atoms have negative charge and ionized donor atoms have an excess of positive charge because holes in the valence band contribute a positive charge and electrons in the conduction band contribute a negative charge. The total charge density ρ in a doped semiconductor is then provided by this equation:

$$\rho = q(p - n + N_D^+ - N_A^-)$$

q is the fundamental unit of charge multiplied by the algebraic sum of the charge carrier densities and the ionized impurities concentrations [12].

Photons incident on the surface of a semiconductor are either reflected from the top surface, absorbed in the material, or transmitted through the material if neither of the above two processes occurs. Reflection and transmission are often regarded as loss processes in photovoltaic systems since photons that are not absorbed do not produce electricity. If the photon is absorbed, it may excite an electron from the valence band to the conduction band. The energy of a photon is an important element in deciding whether it is absorbed or transmitted. As a result, only if the photon has enough energy (more than the energy gap) the electron will be stimulated from the valence band into the conduction band.

How far into a material light of a specific wavelength may travel before it is absorbed depends on the substance's absorption coefficient. Light is only weakly absorbed in materials with low absorption coefficients, and if the material is thin enough, it will look transparent to that wavelength. [13].

Not only electrons with energy already near to the band gap but also other particles can interact with the photon as its energy rises. As a result, more electrons have the potential to interact with the photon and cause it to be absorbed [13].

The Shockley solar cell equation offers a formula for the relationship between the current through a diode and voltage and describes the equivalent I-V characteristic.

$$I = I_{ph} - I_0\left(e^{\frac{qV}{k_bT}} - 1\right)$$

[14]

Where q (>0) corresponds to the electron charge, k_B is the Boltzmann constant, T the temperature (absolute), V the voltage of the cell, I_{ph} the photocurrent and I_o the saturation current of the diode.

Two crucial processes are involved in the production of "light-generated current," the current produced by a solar cell. To form electron-hole pairs, incoming photons must first be absorbed; if the incident photon has an energy larger than the band gap, electron-hole pairs will be produced in the solar cell. However, since they are meta-stable, electrons in p-type materials and holes in n-type materials can only persist for about as long as the minority carrier lifetime before recombining. By utilizing a p-n junction to spatially separate the electron and the hole, a second process—the collection (separation) of these carriers—prevents this recombination. The electric field (E) present at the p-n junction acts to separate the carriers forming a *depletion region*. The electric field at the p-n junction sweeps the light-generated minority carrier across the junction, where it becomes a majority carrier, if the minority carrier ever makes it there. The light-generated carriers flow across the external circuit if the solar cell's emitter and base are connected (i.e., if the solar cell is shorted)[11].

Power generation is not a result of the gathering of light-generated carriers alone. Both a voltage and a current must be produced in order to produce electricity. The "photovoltaic effect" is a mechanism that creates voltage in a solar cell. Moving electrons to the n-type side of the junction and holes to the p-type side is a result of the p-n junction's collection of light-generated carriers. Since the carriers leave the device as light-generated current through a short circuit, there is no charge build-up.

It is possible to observe the effect of the current-voltage properties of a p-n junction of a solar cell through the J-V curve. The graph below represents the condition of the device with and without illumination, as already mentioned the solar cell has the same properties of a diode.

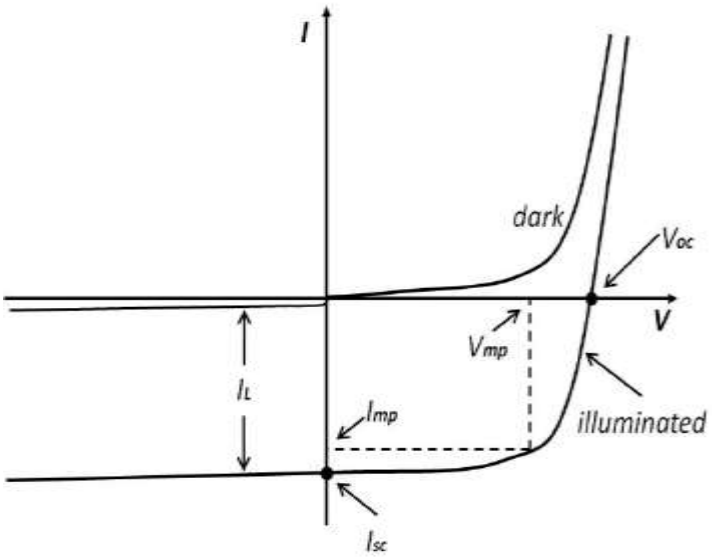

Figure 8. I-V characteristics of a perfect diode solar cell in both the dark and light conditions.

[15]

The impact of the light is to move the IV curve towards the fourth quadrant, where the diode may be powered. The typical "dark" currents in a diode are increased when a cell is illuminated, and this results in the diode law (where the light generated current is I_L).

$$I = I_0 \left[exp\left(\frac{qV}{nkT}\right) - 1 \right] - I_L$$

[11]

The photogenerated current I_L is typically described in terms of quantum efficiency or spectrum response since it is intimately connected to the photon flux impinge on the cell and depends on light wavelength; it is often independent of the applied voltage. The photogenerated current I_L and the short circuit current I_{sc} are identical in the ideal situation, and the greatest voltage that may be generated in an open condition (no current through the cells) is the V_{oc} (open circuit voltage) that is equal to:

$$V_{oc} = \frac{k_B T}{q} ln\left(1 + \frac{I_L}{I_0}\right)$$

It is simple to calculate the fill factor FF by the voltage V_m and current I_m at which the cell generates its maximum power P_{max}.

$$FF = \left(\frac{V_m \cdot I_m}{V_{OC} \cdot I_{sc}}\right)$$

[16]

This is a factor that, along with V_{oc} and I_{sc}, defines the solar cell's maximum power output. The area of the biggest rectangle that will fit in the IV curve and a graphic representation of the FF. This is a diagram of the FF [17].

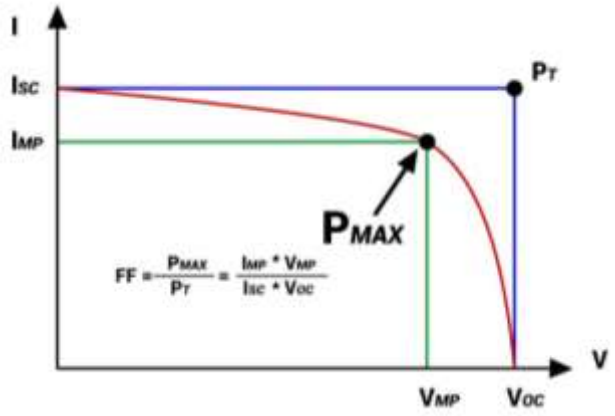

Figure 9. Fill Factor representation.

[18]

A solar cell with a greater voltage has a bigger potential FF because the "rounded" section of the IV curve occupies less space, and FF is a measure of how "square" the IV curve is. By differentiating the power from a solar cell with respect to voltage and locating the point when this equals zero, the maximum theoretical FF from a solar cell can be found [17].

$$\frac{d(IV)}{d(V)} = 0$$

[17]

To evaluate how well one solar cell performs in comparison to another, the efficiency is another criterion that is most frequently used: is defined as the ratio of solar cell energy output to solar energy input. The efficiency depends on solar cell temperature and on the spectrum and intensity of the incident light in addition to how well the solar cell performs itself. To evaluate the performance of different devices, it is necessary to

precisely regulate the conditions in which efficiency is assessed. At a temperature of 25°C and at AM1.5[1] circumstances, terrestrial solar cells are measured. In AM0 circumstances, solar cells designed for space application are measured [19].

The efficiency of a solar cell is defined as the proportion of incident power converted to electricity and is calculated as follows:

$$\eta = \frac{V_{OC} I_{SC} FF}{P_{in}}$$

With

η: efficiency

V_{OC}: open circuit voltage;

I_{SC}: short circuit current;

FF: fill factor

[19]

[1] The direct optical route length through the Earth's atmosphere is determined by the air mass coefficient, which is represented as a ratio to the path length vertically upwards, or at the zenith. When the solar radiation has passed through the atmosphere, the air mass coefficient may be utilized to assist describe the solar spectrum.
The syntax "AM" followed by a number is frequently used to refer to the air mass coefficient, which is frequently used to describe the performance of solar cells under standardized settings. Almost always, when describing terrestrial power-generating panels, "AM1.5" is used [86].

1.6 The second-generation photovoltaic cells: thin films

The production of solar cells utilizes a variety of processes, including material modification. Photovoltaics have grown to play a significant role in the continuing energy transition over the past ten years. The evolution of that product has been greatly influenced by developments in manufacturing processes and material science. Photovoltaics must yet overcome a few obstacles before they can deliver more cheap and clean energy. The focus of research in this area is on printable solar cell components like quantum dots, graphene or intermediate band gap cells, and efficient photovoltaic systems like multi-junction cells[20].

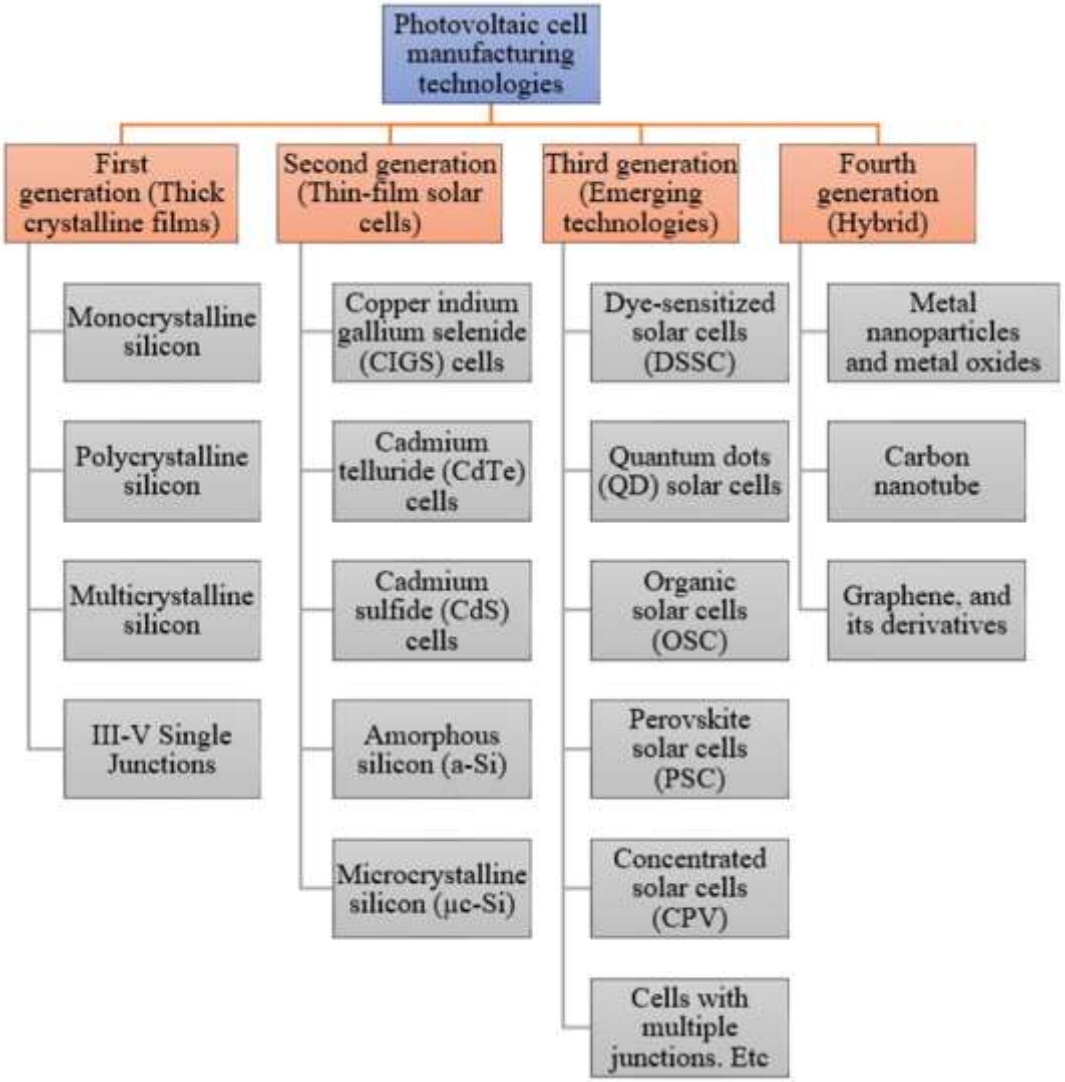

Figure 10. Different types of solar cells and recent advancements in this area.

Different photovoltaic cells' generations basically narrate the phases of their earlier evolution. Since the development of solar cells some decades ago, photovoltaic technology has been categorized into four primary generations.

- **First generation**: The earliest use of photovoltaics was silicon-based PV cells, which drew on the manufacturing knowledge and raw ingredients offered by the microelectronics sector. With a market share of 90%, silicon-based solar cells currently account for more than 80% of installed capacity worldwide. They are the most often utilized cells because of their comparatively high efficiency. Materials based on thick crystalline layers of silicon (Si) are used in the first generation of solar cells. Mono, poly, and multicrystalline silicon as well as single III-V junctions serve as the foundation for this generation (GaAs). The first generation focuses on p-n junction-based photovoltaic cells, the majority of which are silicon photovoltaics built on mono- or polycrystalline wafers.
- **Second generation**: the development of thin film photovoltaic cell technology from "microcrystalline silicon (c-Si) and amorphous silicon (a-Si), copper indium gallium selenide (CIGS), and cadmium telluride/cadmium sulfide (CdTe/CdS) photovoltaic cells" are included in this generation. As a less expensive alternative to crystalline silicon cells, thin film photovoltaic cells based on CdTe, gallium selenide, and copper indium gallium diselenide (CIGS) or amorphous silicon have been developed. Although they have better mechanical qualities that are great for flexible applications, there is a chance that their efficiency may suffer. Unlike the previous generation of solar cells, which were an example of microelectronics, thin films required new techniques for growth and opened the industry up to other disciplines, such as electrochemistry.
- **Third generation**: this generation of solar cells, which also includes tandem, perovskite, dye-sensitized, organic, and emerging concepts, represent a variety of strategies, from affordable low-efficiency systems (dye-sensitized, organic solar cells) to pricey high-efficiency systems (III-V multi-junction cells), for uses ranging from building integration to space applications. Even though some of the third-generation photovoltaic cells have been researched for more than 25 years, they are frequently referred to as "emerging ideas" due to their

limited commercial penetration. The most recent developments in silicon photovoltaic cell design involve techniques that produce extra levels of energy in the semiconductor's band structure. Third-generation solar cells are the focus of the most recent manufacturing technology and efficiency enhancement investigations.

- **Fourth generation**: because they combine the affordability and adaptability of polymer thin films with the stability of organic nanostructures like metal nanoparticles and metal oxides, carbon nanotubes, graphene, and their derivatives, fourth-generation photovoltaic cells are also referred to as hybrid inorganic cells. These items, sometimes known as "nanophotovoltaics," may represent the bright future of photovoltaics[20].

Every year the national Renewable Energy Laboratory (NREL) analyses and updates data and tools to provide a chart of the highest confirmed conversion efficiencies of several photovoltaic technologies such as single and multi-junction cells, crystalline Si cells, thin films technologies and emerging photovoltaics. The different categories are distinguished by colours and symbols. Thin-film solar cell technologies have made significant progress in efficiency in recent years, however, there are still many improvements to be made[21].

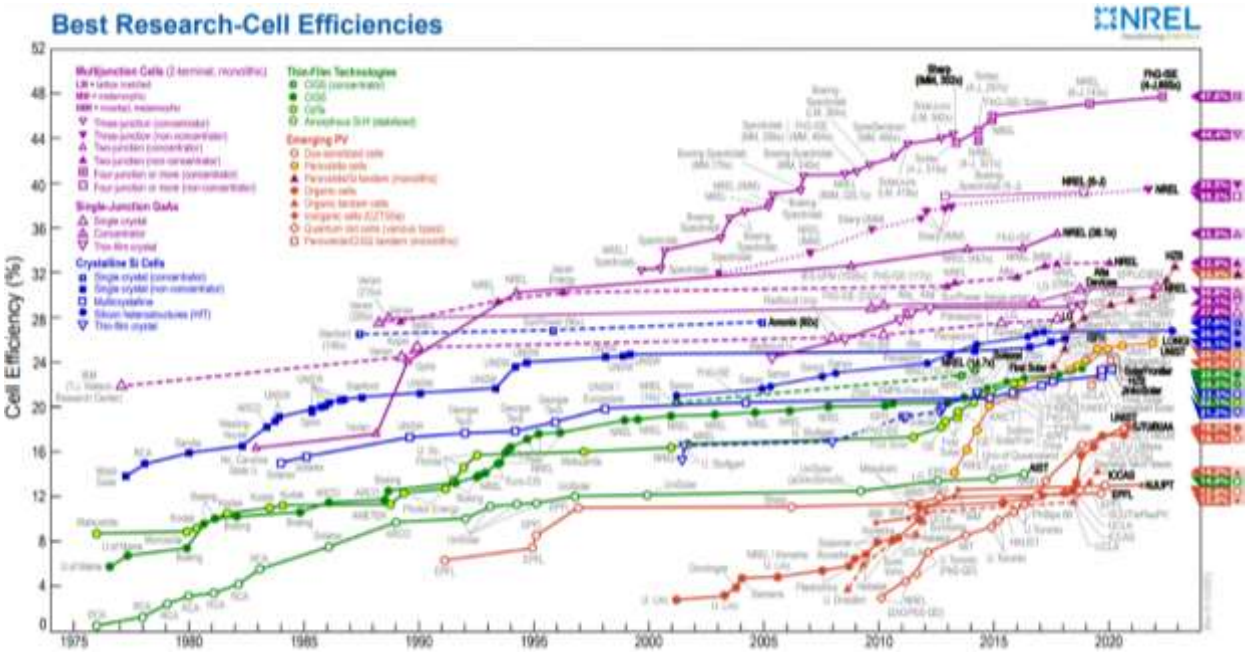

Figure 11. Timeline Chart of the highest confirmed conversion efficiencies for research cells from 1976 to the present.

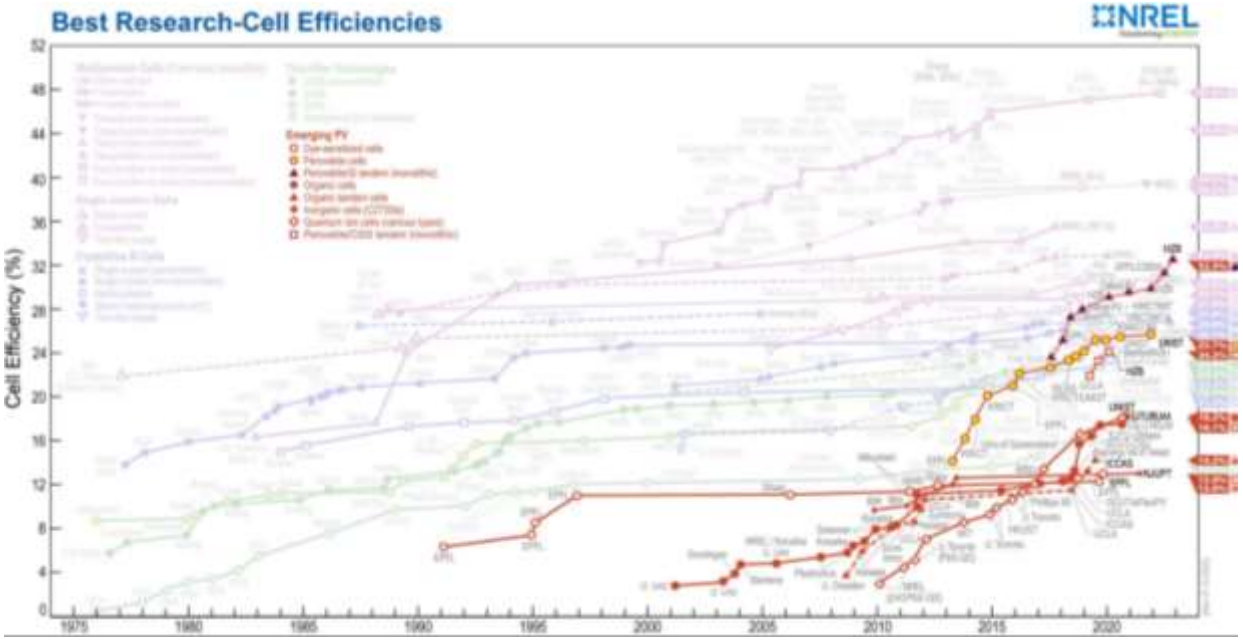

Figure 12. Specific Efficiency Chart for emerging PV technologies.

[21]

1.7 CZTS and CZTSe

CdTe and Cu(In,Ga)Se_2 (CIGSe) solar cells have achieved impressive efficiencies of over 20%. Nevertheless, elements such as indium and tellurium are rare, the presence of cadmium giving a distorted perception of the environmental impact of CdTe, these problems may limit the implementation of these terawatt-scale devices. CZTS have emerged as alternative materials for thin-film solar cells due to their promising optoelectronic properties and the use of non-toxic soil rich elements.

CZTS was first studied as a solar cell material in 1988 in Japan at Shinshu University. The researchers lay down a thin layer of his CZTS by sputtering and in the visible range they measured his p-type conductivity, a direct bandgap of 1.45 eV. The following year, a V_{oc} of 0.165 V for this solar cell was reported, but the J_{sc} was very short. In 1996 was fabricated the first solar cell with a cadmium sulfide/zinc oxide window layer based on his CZTS and his CZTSe ($Cu_2ZnSnSe_4$) absorbers with an efficiency of over 0.6%. During next decade of research, with improvements in processing conditions and with new window layers, the efficiency approached the 7%. IBM's Watson Research Center reach the world record efficiency (12.6%) for CZTSSe-based solar cells using a hydrazine-based solution precursor [22].
Nowadays the highest efficiency for CZTSSe is 13% reached by the NJUPT University [21].

1.7.1 Structure of the material

The kesterite (CZTS), which is widely wanted for solar materials, has the traditional photovoltaic features including direct-band gap, high absorption coefficient, and optical band gap energy of the range 1.4-1.5 eV.
There are different crystallographic structures, depending on how the atoms of the elements are positioned and how the synthesis takes place; the difference in arrangement and tetrahedral voids result in three different structures: Kesterite, Stannite, PMCA.
The first two have a body-centered tetragonal structure, the third one PMCA has a primitive tetragonal structure: a layer of Cu alternates with layers of Zn and Sn in the

ST and PMCA structures, but the KS structure consists of two alternating cation layers, each having Cu and Zn or Cu and Sn.

In particular kesterite (KS) belong to the space group I4 with cations positioned at half of tetrahedral voids after the stacking sequence of zinc mix and sulphur anions arranged as cubic closed packed (CCP) array [23].

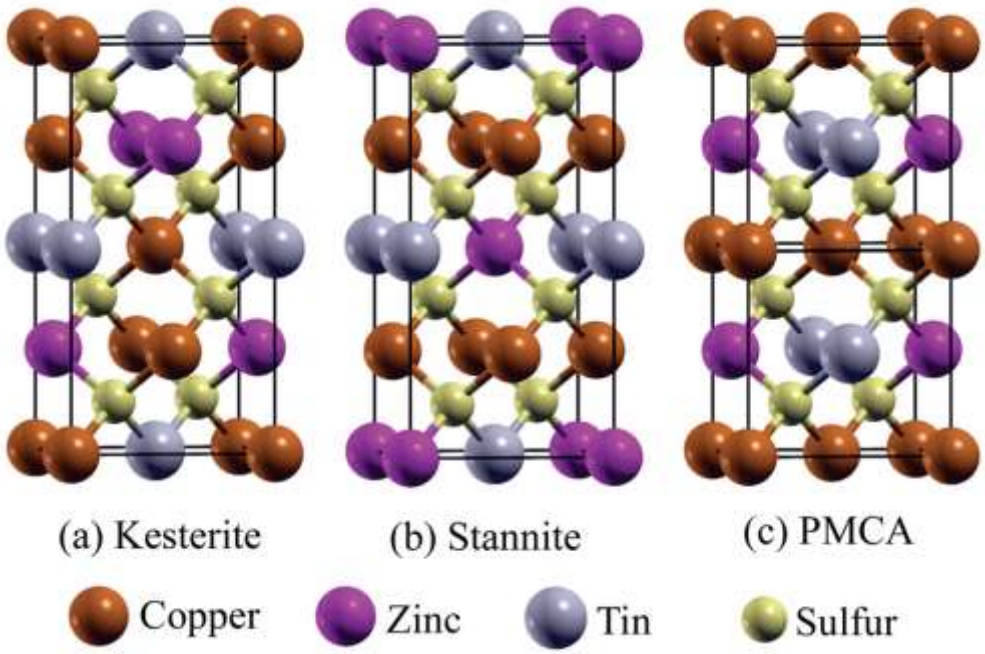

Figure 13. Structures of Kesterite (a), Stannite (b), PMCA (c). The substitution of S atoms wit Se atoms generates the CZTSe structure.

There are several competing theories that attempt to explain the structure of Cu_2ZnSnS_4. Due to the stannite phase's slightly greater energy than the kesterite phase, it is demonstrated by the first principle of research that the kesterite is the more stable compound when compared to mono-crystalline Cu_2ZnSnS/Se_4 stannite structure in an I2-II-IV-VI4 group. Kesterite and stannite are responsible for the Cu-Zn atomic layer's partial disordering. The atomic numbers of Cu and Zn differ just a little from one another. Since these elements have high melting points, the temperature at which molecules develop is high. The CZTS thin film deposition as an absorber layer has typically been carried out at temperatures between 500 and 600°C. This temperature provides enough energy for solid-state chemical reactions, grain development, and the formation of defect-free grain boundaries, as well as for the introduction of volatile species into the solid phase [24].

1.7.2 Phase Diagram

Compared to ternary, binary, and unary phases, the synthesis of the quaternary compound (I2-II-IV-VI4) is more complicated because it is challenging to manage morphology, phase structure, and stoichiometry at the same time. Quaternary (Cu_2ZnSnS_4), ternary (Cu_2SnS_3), and binary compounds (CuS, ZnS, SnS, Cu2S, SnS2) phases are discovered when the quaternary compound Cu_2ZnSnS_4 is synthesized.
The phase equilibrium is interrupted by the creation of these phases. The modification of the element ratio, temperature, and pressure can regulate the phase equilibrium. It is necessary to choose one parameter and make the other parameters variable to optimize the appropriate phase. Numerous studies on kesterite have been conducted under various conditions of element composition, temperature, and pressure. The performance of the solar cell is impacted by the changing of these parameters. As a result, the required ratio for Cu/(Zn + Sn) and Zn/Sn limits of element composition ratio are governing phases and defects for growth of single-phase the kesterite [24].

It is crucial to use the phase diagram in order to achieve phase pure CZTS with no or very few impurities. Since CZTS is a quaternary material system, a quaternary phase diagram was in theory necessary. In order to reduce complexity, a simplified pseudo-ternary diagram is utilized, which relies on the equilibrium of sulphur incorporation with the metals Cu(I), Zn(II), and Sn(IV) and their valences[25]. At 400°C, Olekseyuk et al. reported a phase equilibrium diagram. It has been shown via significant research that just a small portion of this diagram (the area indicated by the cursor) may lead to phase pure CZTS. Different secondary phases might occur here if the composition is not under control.

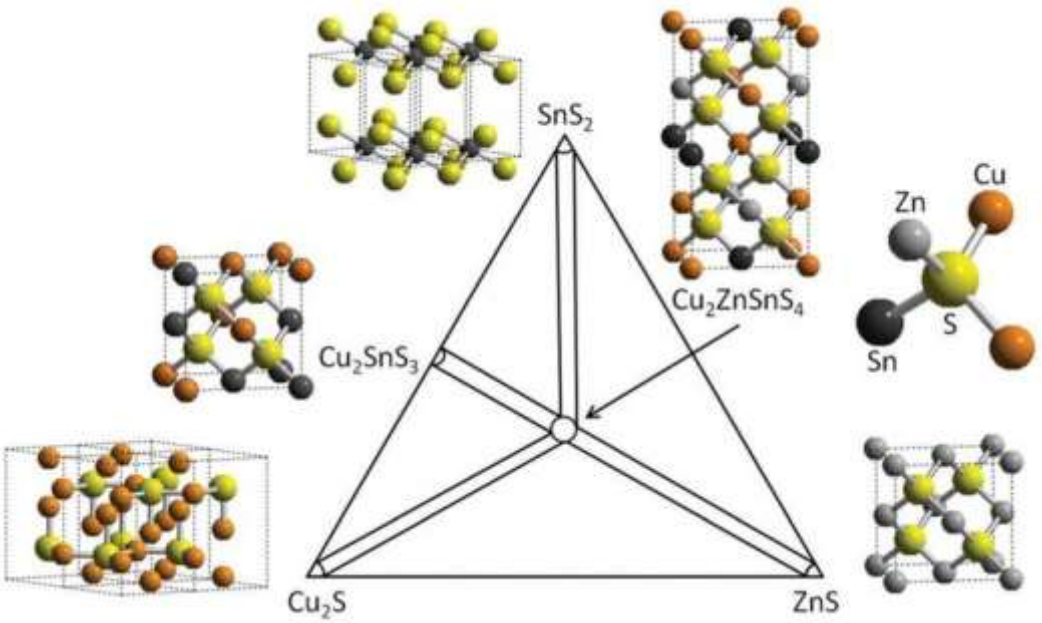

Figure 14. Pseudo ternary phase diagram of CZTS phase and other secondary phases.

If the composition of this region is not controlled, several secondary phases can develop. Components rich in copper, poor in zinc and poor in tin lead to the formation of Cu_xS compounds and ternary CTS. For Zn-rich compositions, monophasic ZnS formation is expected, but ternary phases are not possible. In the case of copper and zinc, the unwanted component $Cu_2ZnSn_3S_8$ can also pass-through tin sulfide (SnS_2) and CZTS at about 700°C [26], [27].

Because of the significant competition between CZTS development and the formation of binary [Cu_2S, ZnS, SnS, SnS_2] and ternary phases [Cu_2SnS_3], the complexity of this quaternary system grows several folds. The volatile nature of Zn and Sn exacerbated the limited phase stability and secondary phase development in the copper-poor situation. Out diffusion of S under advantageous high temperature annealing conditions during CZTS solar cell production generates additional favorable circumstances for the formation of secondary phases, defects, and defect-complexes. Table 1 outlines the secondary phases and their characteristics in CZTS materials that have been described [28].

Table 1. Secondary phase features discovered in CZTS materials.

PROPERTIES	Cu_2ZnSnS_4	ZnS	Cu_2S	SnS_2	Cu_2SnS_3
BAND GAP (EV)	~1.45	3.54-3.68	1.21	2.2	0.98-1.35
ELECTRICAL PROPERTIES	Semiconductor p-type	Insulator	p-type, highly defective	n-type	p-type
STRUCTURAL PROPERTIES	Kesterite	Sphalerite and Wurtzite	Chalcocite	Rhomboedral	Cubic and Tetragonal
IMPACT ON SOLAR CELL PERFORMANCE	Absorbing material	Insulating, reducing active area	Metallic, short solar cell	n-type, diode and barrier for carrier collection	Influence carrier collection efficiency

Because ZnS has a large band gap (3.54 eV) and is insulating in nature, it can lower the active area required to form electron-hole pairs and collect current. Moreover, because ZnS and Cu_2SnS_3 have similar crystal structures, it is difficult to distinguish them in x-ray diffraction experiments.

Due to its high conductivity, Cu_2S has the potential to short solar cells. In addition, SnS_2 has a band gap of around 2.2 eV and is an n-type semiconductor. In the absorbing layer, this may create a secondary diode or it might be insulating, which would lead to increased photocarrier recombination. Other Sn and S phases, such as SnS and Sn_2S_3, have also been found in CZTS solar cells. Compared to the SnS_2 phase, these phases exhibit radically distinct characteristics. Sn_2S_3 is a mixed phase dependent on the Sn and S defects, whereas SnS is p-type with an optical band gap of 1.11 eV. In Zn-poor circumstances, the Cu_2SnS_3 (CTS) phase is another one that may be seen in CZTS materials. Despite the fact that CTS is a p-type semiconductor with a band gap that is similar to that of CZTS-Se and may absorb light in the same solar spectrum range, new research has shown that this material is less effective than CZTS thin film [28].

The forward and backward reactions occur at the same rate at the atomic and molecular levels in the chemical equilibrium of CZTS. As a result, as demonstrated by the equations in the next two phases, there is no net change in the concentration of products and reactants.

$$Cu_2S(s) + ZnS(s) + SnS\ (s) + \frac{1}{2}S_2 \Leftrightarrow CZTS\ (s)$$

$$SnS\ (s) \Leftrightarrow SnS\ (g)$$

The kesterite in the equilibrium state of CZTS must have the standard value of the lattice at a = 0.5435 nm and c = 1.0843 nm. The sulphur to selenium element ratio affects the lattice constants [24].

Chapter II
Materials and methods

The components used in this study are listed in this chapter along with the synthesis's experimental details. Methods for device fabrication are also presented.

2.1 Materials

We focused initially on chloride salt-based reagents using first thioacetamide as the sulfur source, and then thiourea; at a later stage, we joined acetate-based formulations. Production costs for solution-based processes are lower, and if properly tuned, they can still give a strong control over the stoichiometry of the film. The majority of solution-based approaches, however, employ a two-step process and harmful H_2S gas for sulphurization. Copper (II) acetate monohydrate $Cu(CH_3COO)_2$, zinc (II) acetate dihydrate Zn $(CH_3COO)_2 \cdot 2H_2O$, tin (II) chloride $SnCl_2$, and thiourea $SC(NH_2)_2$ were dissolved in 2-methoxy ethanol and diethanolamine to synthetize the precursor solution. Without additional purification, all ingredients were employed. 2-Methoxyethanol $CH_3OCH_2CH_2OH$ was used as a solvent, and diethanolamine (DEA) served as a stabilizer [29].

2.2 Sputtering deposition method

The process of sputter deposition is employed to produce thin coatings on surfaces. The method is based on bombarding a target, or source material, with ions. Ion bombardment produces a vapor as a result of the target material sputtering, which is a purely physical process. This method is a member of the category of physical vapor deposition methods, which also includes pulsed laser deposition and thermal evaporation. Using a magnetron source to spray the target with positive ions from the plasma of a magnetically accelerated glow discharge is the most typical method for generating thin layers via sputter deposition.

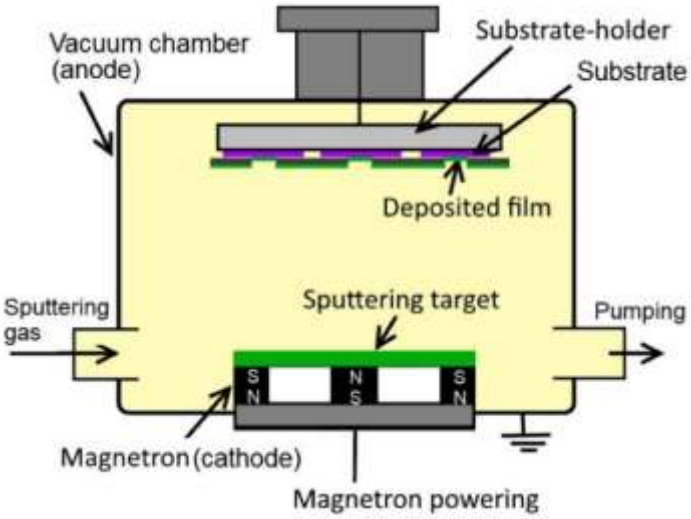

Figure 15. Operating concept for sputtering deposition methods.

[30]

Direct current (DC) for conductive targets, radio frequency (RF) for nonconductive targets, and several other methods of delivering current and/or voltage pulses to the target can all be used to power the target. Sputtering is a purely physical process, therefore reactive sputtering, which adds chemistry to the plasma by mixing in a reactive gas, is the only way to, for instance, deposit a compound layer. The undesired interaction between the reactive gas and the target material causes the deposition parameters to behave nonlinearly as a function of reactive gas flow. The fluxes of the various species toward the target must be identified in order to predict this behavior [31].

2.3 Absorber deposition

In this work we tested different deposition technique: spin coating, inkjet printing, doctor blade, dip coating. Below we present an overview of the deposition techniques tested.

2.3.1 Spin coating

The method of spin coating is frequently used to deposit thin films on surfaces. Is employed in a vast array of technological fields and industrial sectors. Spin coating's main advantage over other techniques is its capacity to manufacture uniform films swiftly and easily.

By coating (casting) a solution of the desired material in a solvent (an "ink") while it is spinning, spin coating entails the application of a thin film (a few nm to a few μm) uniformly across the surface of a substrate [32].

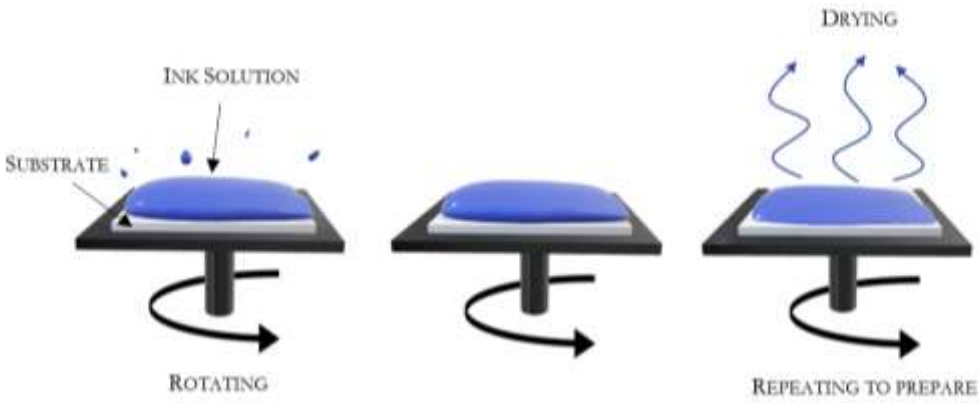

Figure 16. A visual illustration of the various spin coating thinning regimes.

The centripetal force combined with the surface tension of the solution pushes the liquid coating into an even covering while the substrate rotates quickly. The solvent then evaporates during this period, leaving the required substance in a layer on the substrate.

The solution is first cast onto the substrate, usually with the aid of a pipette. Centrifugal force will disseminate the fluid throughout the substrate whether it is already spinning (dynamic spin coating) or being spun after deposition (static spin coating). The substrate then reaches the appropriate rotation speed, either right away or after a spreading step at a lower speed. Most of the solution has now been ejected from the substrate. The fluid may spin more slowly than the substrate at first, but soon the

rotation speeds will match as drag equalizes rotational accelerations, causing the fluid to level out.

As viscous forces now predominate, the fluid starts to thin. Frequently, the film will change color when the fluid is thrown off owing to interference effects (see video below). It will be clear when the film is mostly dry when the color changes stop. Because the fluid must condense into droplets near the edge in order to be flung off, edge effects may occur. Finally, fluid outflow ends, and solvent evaporation takes over as the dominant process in thinning. Vapor pressure, ambient temperature, and solvent volatility all affect how quickly a solvent evaporates. The film will exhibit similar non-uniformities because of differences in the rate of evaporation, such as those seen near a substrate's edge [32].

2.3.2 Printing

Inkjet printing technique, which enables one-step direct patterning of functional elements including conductive, insulating, and semiconducting materials onto the substrate, is one of the most promising alternatives to vacuum procedures.

In this work we used a compact printer with integrated printheads based on the dependable HP TIJ2.5 technology, which delivers reliable, high-quality printing quickly. The user interface of the printer is so simple to operate that it requires little to no training [33].

Figure 17. The compact printer used during this work.

The core of TIJ2.5 inkjet technology is the formation of jets of vapor bubbles by heating tiny droplets of ink in the cartridge chamber where the ink is stored at a certain frequency and voltage. These jets of vapor bubbles are precisely blasted onto the substrate's surface from the ink chamber through holes in the cartridge nozzle known as pixels to produce the desired text or picture [34].

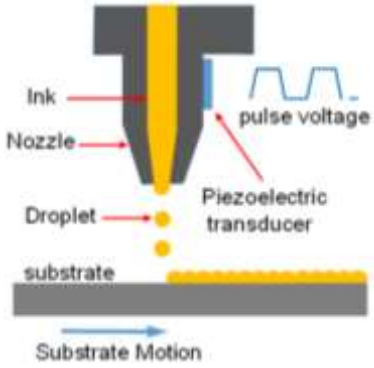

Figure 18. A representation of the inkjet printing process.

[34]

2.3.3 Doctor Blade

A method for creating films with precise thicknesses is doctor blade coating. The method involves positioning a sharp blade at a certain distance from the surface to be coated. The blade is then positioned in front of the coating solution and pushed across the surface in line with the surface, forming a wet film. The approach should, in theory, have solution losses of approximately 5%, but in practice it takes time to find the perfect circumstances [35].

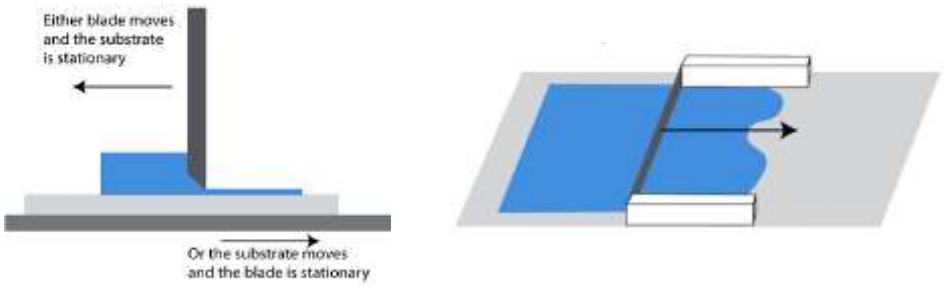

Figure 19. Blade coating: the movement of the blade on the substrate.

[36]

2.3.4 Dip coating

Dip coating is a quick, dependable, and effective method for coating practically any substrate material, however it is not without flaws. These consist of uneven covering (differing thicknesses across the material's surface) or coating accumulation (which is created as the material "drip-dries"). Substrate material is immersed in conformal coating during the dip coating process, removed, and allowed to drip dry. Following the draining of the surplus coating, the substrate material is further dried using a number of methods, most frequently baking [37].

The interplay of several types of forces might be viewed as the withdrawal stage of the dip coating process. Both draining forces and entraining forces can be used to classify these forces. The liquid is drawn away from the substrate and back toward the bath by draining forces. Entraining forces, on the other hand, aim to keep fluid on the substrate. The thickness of the wet film deposited onto the substrate is determined by the balance between these two sets of forces. There are four distinct areas in which the wet film forms during the withdrawal stage (shown in the figure below)[38].

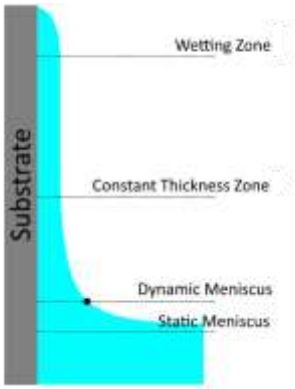

Figure 20. Four separate areas are involved in the production of the dip coating layer. [38]

2.4 Annealing

For the growth of CZTSSe thin films, the selenization procedure is a useful stage in the recrystallization process. Additionally, it impacts the system's defect states and phase purity. The majority of the reported works use high temperature annealing (over 500°C) to boost the crystallite quality and enhance the absorber's optoelectronic capabilities [39].

Annealing is a heat-treatment procedure that modifies a material's physical and occasionally chemical characteristics. This heating process also causes atoms to move about in the crystal lattice and lowers the number of dislocations. As it cools, the heat-treated material recrystallizes. The heating and cooling speeds affect the crystal grain size and phase composition, which in turn affects the material characteristics [40].

In general, the annealing process with sulfur also called sulfurization (or selenization if in presence of selenium) is conducted in furnaces.

Recovery, recrystallization, and grain development are the three phases of an annealing furnace. At the lower temperatures of the process, the recovery phase takes place. By eliminating linear imperfections known as dislocations and the internal stresses they cause, the material being annealed is softened in this process.

To replace the grains that were eliminated in the recovery state, fresh strain-free grains nucleate and develop during the recrystallization stage.

Only until recrystallization is complete and annealing is permitted to proceed can grain growth take place. The material's microstructure begins to deteriorate as grains develop [41].

Figure 21. Example of single zone horizontal tube furnace.

[42]

Chapter III
Characterization Techniques

In this chapter, it is described how the CZTSSe devices were characterized and analyzed using a variety of methods. The background physics of each instrument will, however, be thoroughly covered in this section.

3.1 SEM

One technology used to examine the structure of kesterite is SEM. A concentrated stream of high-energy electrons is utilized by the scanning electron microscope (SEM) to produce a range of signals at the surface of solid objects. In addition to the sample's exterior morphology (texture), the signals resulting from electron-sample interactions also provide information about chemical composition, crystalline structure and orientation of the sample constituent components. Most often, a portion of the sample's surface is chosen for data collection, and a 2-dimensional picture is created to show the spatial changes in these attributes.

Significant quantities of kinetic energy are carried by the accelerated electrons in a SEM, and as the incident electrons decelerate in the solid sample, this energy is released

as a variety of signals. These signals include heat, cathodoluminescence (CL), visible light (secondary electrons), backscattered electrons (BSE), diffracted backscattered electrons (EBSD), characteristic X-rays (used for elemental analysis). Both secondary electrons and backscattered electrons may be used to image samples, with secondary electrons being most useful for displaying the morphology and topography of samples and backscattered electrons being most useful for highlighting compositional differences in multiphase samples (i.e. for rapid phase discrimination).

Inelastic collisions between incoming electrons and electrons in certain atomic orbitals (shells) in the sample result in the emission of X-rays. The accelerated electrons produce X-rays with a defined wavelength when they transition back to lower energy states (that is related to the difference in energy levels of electrons in different shells for a given element). As a result, each element in a mineral that the electron beam "excites" emits distinctive X-rays. SEM examination is regarded as "non-destructive" since the volume of the sample is not lost due to the x-rays produced by electron interactions, allowing for repeated investigation of the same materials[43].

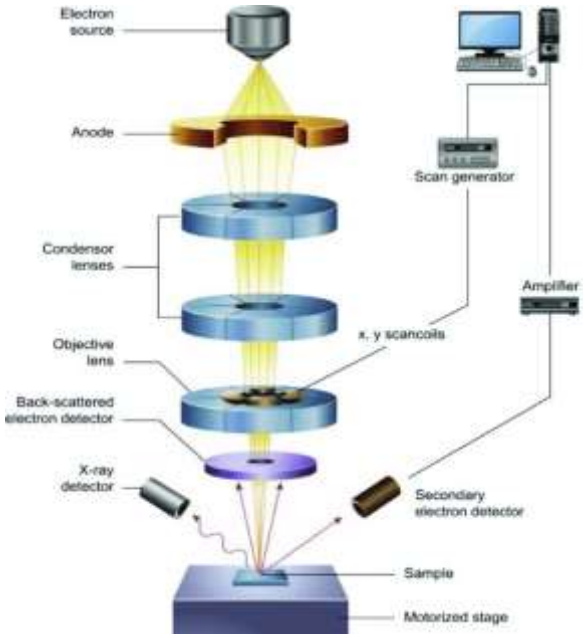

Figure 22. Schematic draw of a SEM instrument.

Depending on the nature of the samples and the data needed, sample preparation for SEM analysis can range from simple to complex. A sample that will fit into the SEM chamber must be acquired, and some accommodations must be made to prevent charge accumulation on electrically insulating substances. A thin coating of conducting substance, frequently carbon, gold, or some other metal or alloy, is coated on the majority of electrically insulating samples. The best conductive coating material depends on the type of data to be collected: carbon is best if elemental analysis is a top priority, whereas metal coatings work best for high-resolution electron imaging applications. An instrument capable of "low vacuum" operation can also be used to evaluate an electrically insulating material devoid of a conductive covering [43].

3.2 AFM

In an atomic force microscope (AFM), a sharp probe is mechanically swept over a surface and the motion of the probe is caught by a computer. The mobility of the probe is then utilized to build a three-dimensional picture of the surface. In AFM, the probe can be scanned over a stationary surface (tip scanning AFM), or the sample can be scanned below a stationary probe (sample scanning AFM)[44].

When the scanning probe microscope raster-scans the probe over a part of the sample while simultaneously measuring its local parameters, an image is created. After the Scanning Tunneling Microscope was created in 1980 by Gerd Binnig and Heinrich Rohler at IBM Research in Zurich, the Atomic Force Microscope was created in 1982 by researchers working for IBM.

By sensing intermolecular forces and viewing atoms on the specimen's nanoscale probed surfaces, the Atomic Force Microscope operates on this concept. Three of its main operating principles are surface sensing, detection, and imaging, enable its operation. Molecular engineering, polymer chemistry, surface chemistry, molecular biology, medicine are just a few of the fields in which this form of microscopy has been employed. It is also utilized in solid-state physics, semiconductor research, and physics[45].

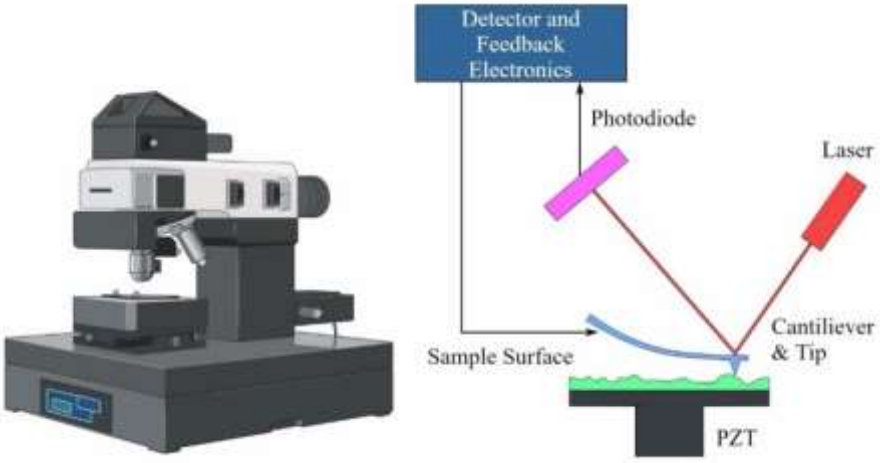

Figure 23. Atomic force microscope (AFM).

[45]

The cantilever deflects when the probe moves across the surface of the sample due to attraction or repulsive forces between the tip and sample, which are typically Van Der Waal forces but can also include electrostatic and hydrophobic/hydrophilic forces. A laser that is reflected off the cantilever and into photodiodes measures the deflection. One of the photodiodes produces an output signal that is analyzed and gives information on the vertical bending of the cantilever as it gathers lighter. The height of the probe is then controlled by a scanner as it goes over the surface using this data. A three-dimensional topographical image of the sample may then be created using the height variance introduced by the scanner [46].

3.3 XRD

Electromagnetic radiation is a mix of alternating electric and magnetic fields that flow in a wave motion over space. Because radiation is a wave, it may be characterized in terms of wavelength or frequency, which are connected by the equation: $\lambda = c/\nu$, where ν is the frequency (in seconds), c is the speed of light ($3 \cdot 10^8$ ms^{-1}) and λ is the wavelength (in meters).

Wavelength is often represented in nanometers (1 nm=10^{-9}m) in UV-Vis spectroscopy. According to the equations, shorter wavelength radiation has more energy, and for

UV-Vis spectroscopy, low (short) wavelength UV light has the most energy. When testing photosensitive materials, this energy may be sufficient to produce undesired photochemical reactions.

A method for examining the atomic or molecular structure of materials is called X-ray diffraction, or XRD. It is non-destructive, works best with fully or partially crystalline materials, and offers thorough details on a material's crystallographic structure, chemical makeup, and physical characteristics.

Electromagnetic radiation with wavelengths that may be measured in nanometers includes X-rays (a nanometer is equivalent to one billionth of a meter). Interferences are produced when monochromatic X-rays scatter from a material with a particular structure. According to Bragg's law, this causes a pattern of increasing and decreasing intensities because of positive and negative interferences. In reaction to X-ray wavelengths, the pattern in crystalline materials produces three-dimensional slices of diffraction that resemble the spacing of planes in a crystal lattice. The method used for investigating crystal structures and atomic spacing is called constructive interference. All diffraction methods begin with x-rays being emitted from a cathode tube or revolving target and then focused on the material. You may examine the structure of the sample by collecting the diffracted X-rays. This is conceivable because each mineral has a unique set of d-spacings. D-spacings are the distances between atom planes that generate diffraction peaks. When utilizing XRD to detect the structure of a sample material, conventional reference patterns of d-spacings can be used as a comparison. Bragg's law is used to explain how X-rays disclose the atomic structure of crystals.

Only when the criteria of Bragg's law are met, diffraction will take place in the interaction between the X-rays and material. In order to achieve maximum intensity, it is necessary that the angle of incidence and angle of scattering be identical, as well as that the path length difference be equal to an integer number of wavelengths. This allows for a computation of the specifics of the crystal structure in question [47].

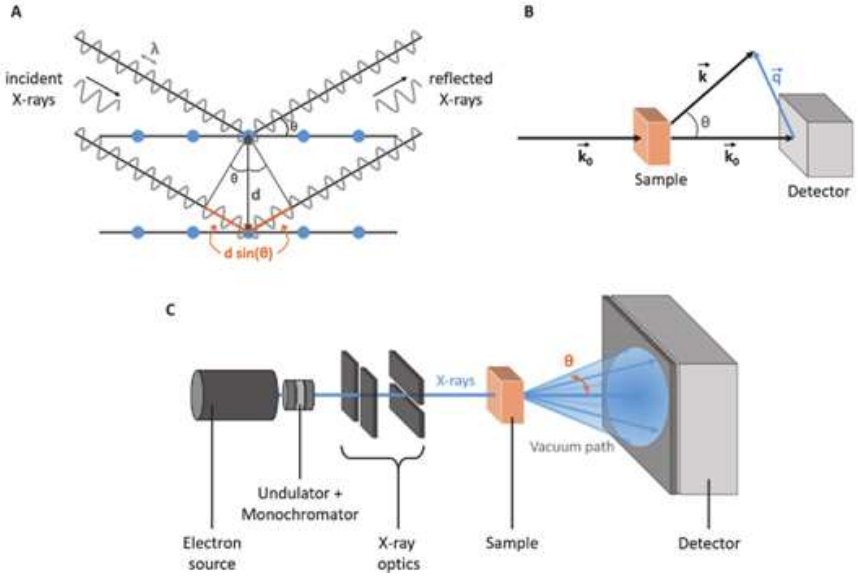

Figure 24. A) Illustration of the Bragg equation B) The incident wave vector k0 and the scattered wave vector k with the half scattering angle are used to geometrically generate the scattering vector q. C) setup of a small-angle X-ray scattering instrument.

[48]

3.4 Raman

Raman spectroscopy is a method for non-destructive chemical examination that offers extensive information about chemical structure, phase and polymorphism, crystallinity, and molecular interactions. It is based on light's interaction with chemical bonds within a substance. Raman is a light scattering method in which a molecule scatters incident light from a powerful laser light source. Rayleigh Scatter occurs when the majority of the scattered light has the same wavelength (or color) as the laser source and does not give relevant information. However, a little quantity of light (usually 0.0000001%) is scattered at various wavelengths (or colors) depending on the chemical structure of the analyte; this is known as *Raman Scatter*.

A Raman spectrum has several peaks that represent the strength and wavelength location of the Raman scattered light. Each peak represents a different chemical bond vibration. Raman spectroscopy investigates a material's chemical structure and offers information on:

- the chemical structure and the identity of the material.
- The polymorphism and the phase.
- The presence of impurities or contaminations.
- The intrinsic stress.

A Raman spectrum is often a distinct chemical fingerprint for a certain molecule or material, and it may be used to swiftly identify the material or distinguish it from others [49].

When photons interact with a molecule, the molecule (more in deep the atoms and their components) may be advanced to a higher energy, a virtual state, as explained by quantum mechanics. There might be several effects from this greater energy level. One such effect might be that the molecule relaxes to a different vibrational energy level than in its initial condition, resulting in a photon with a different energy. The Raman shift is the difference between the energy of the incoming photon and the energy of the scattered photon.

Stokes scattering occurs when the change in energy of the scattered photon is smaller than that of the incident photon. Some molecules may begin in a vibrationally excited state, and when progressed to a higher energy virtual state, they may relax to a lower energy level than the initial excited state. This scattering is known as anti-Stokes scattering [50].

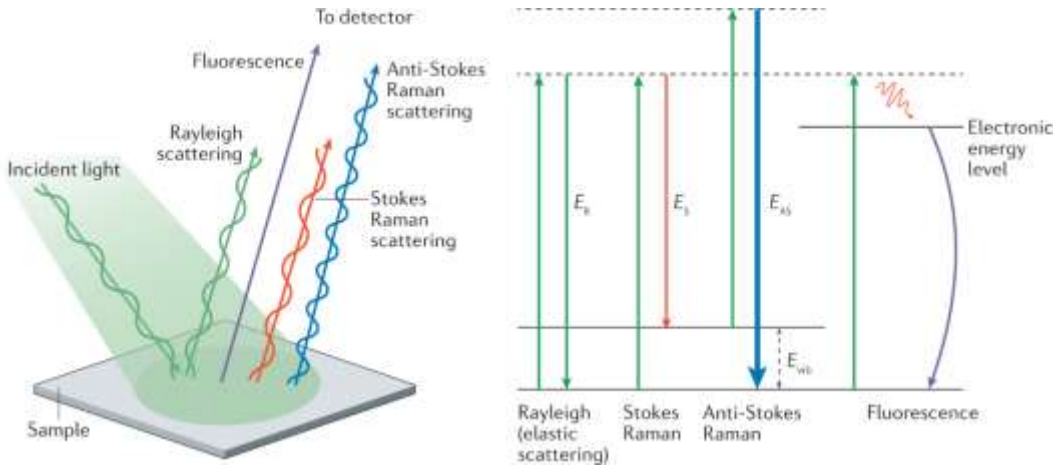

Figure 25. Raman Spectroscopy principles.

[51]

3.5 UV-Vis

UV and visible radiation constitute a minor component of the electromagnetic spectrum, which also includes radio, infrared (IR), cosmic, and X-ray radiation.

$E = h\nu$, where E represents energy (in joules), *h* is Planck's constant ($6.62\ 10^{-34}$ Js), and ν is frequency (in seconds).

Spectroscopy investigates how matter interacts with and emits electromagnetic radiation. Spectroscopy may be classified into several forms based on the wavelength range being measured. The ultraviolet and visible parts of the electromagnetic spectrum are used in UV-Vis spectroscopy. The lower energy infrared section of the spectrum is used in infrared spectroscopy [52].

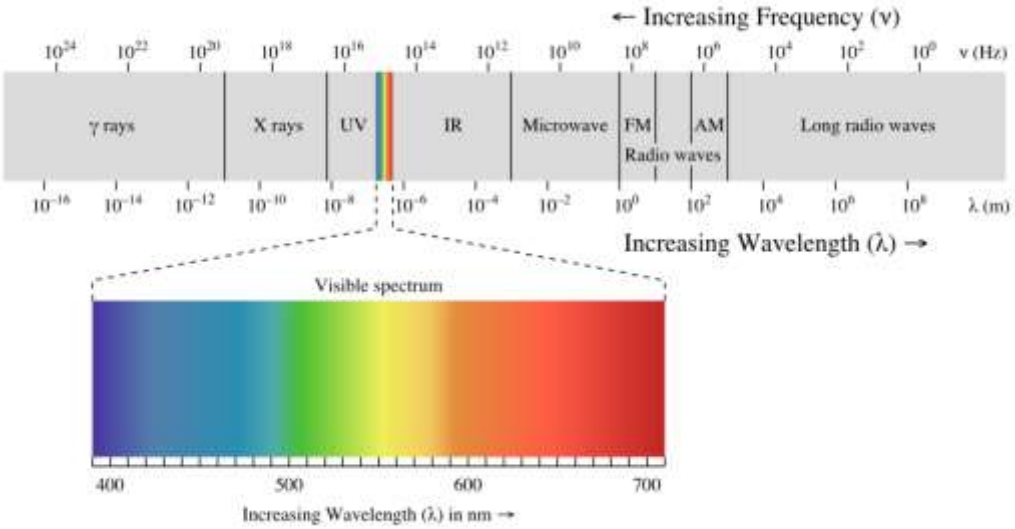

Figure 26. The Electromagnetic Spectrum.

[53]

Several processes may happen when radiation interacts with materials, including reflection, scattering, absorbance, fluorescence/phosphorescence (absorption and re-emission), and photochemical reactions (absorbance and bond breaking). Typically, absorbance is assessed while analyzing materials to determine their UV-visible spectrum.

The quantity of light absorbed when light passes through or is reflected from a sample is the difference between the incident radiation (I_o) and the transmitted radiation (I). Absorbance is the quantity of light absorbed. Transmittance, identified also as the

amount of light that moves through a sample, is often expressed as a fraction of one or as a percentage and is defined as follows:

$$T = \frac{I}{I_0} \text{ or } \%T = \frac{I}{I_0} \cdot 100$$

The following formula describes how absorbance is defined:

$$A = - \log T \quad [52]$$

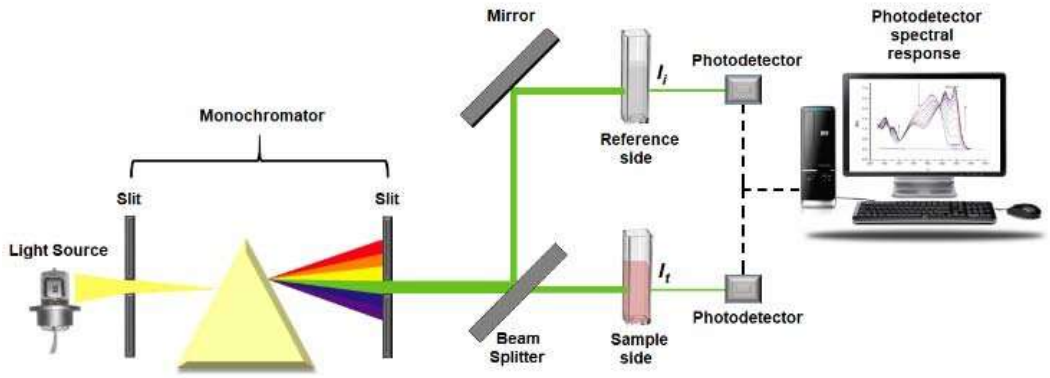

Figure 27. The dual-beam UV-VIS spectrometer is shown schematically.

[54]

UV-Vis spectrophotometers employ a light source to illuminate a sample with light ranging from ultraviolet to visible wavelengths (typically 190 to 900 nm). The light absorbed, transmitted or reflected by the sample at each wavelength is then measured by the equipment. The spectrum acquired can be used to identify the chemical or physical characteristics of the material.

It is also useful to characterize the absorbance or transmittance of a liquid or solid over a wide range of wavelengths, as well as the reflectance qualities of a surface[52].

Characterizing the window materials is very beneficial for improving knowledge of the optical behavior of PV devices under outdoor illumination conditions.

3.6 Current Voltage Measurement

The assessment of their I-V characteristics is one of the crucial measures required for photovoltaic devices. The physical performances of devices, such as photoelectric conversion efficiency, fill factors, and other significant solar cell properties (I_{sc}, V_{oc}, I_{max}, V_{max}, P_{ma} etc.), could be determined by measuring the I-V curves. As already said in paragraph 1.5 one of the most fundamental characterizations of a PV device is the J-V, which is a study of the device's current density voltage graph, from which the parameters for calculating the efficiency of light-energy conversion are retrieved. Ideally, the J-V characteristics are measured with the spectrum of the sun with an illumination density of 100 mW/cm^2, which is the standard value universally used to determine the efficiency of a photovoltaic cell, also called AM 1.5 standard radiation (corresponding at a solar zenith angle of 48.19°, at a standard temperature of 25°C), also considered as "*1 sun*". As a result, a solar simulator or a light capable of reproducing this spectrum, is required.

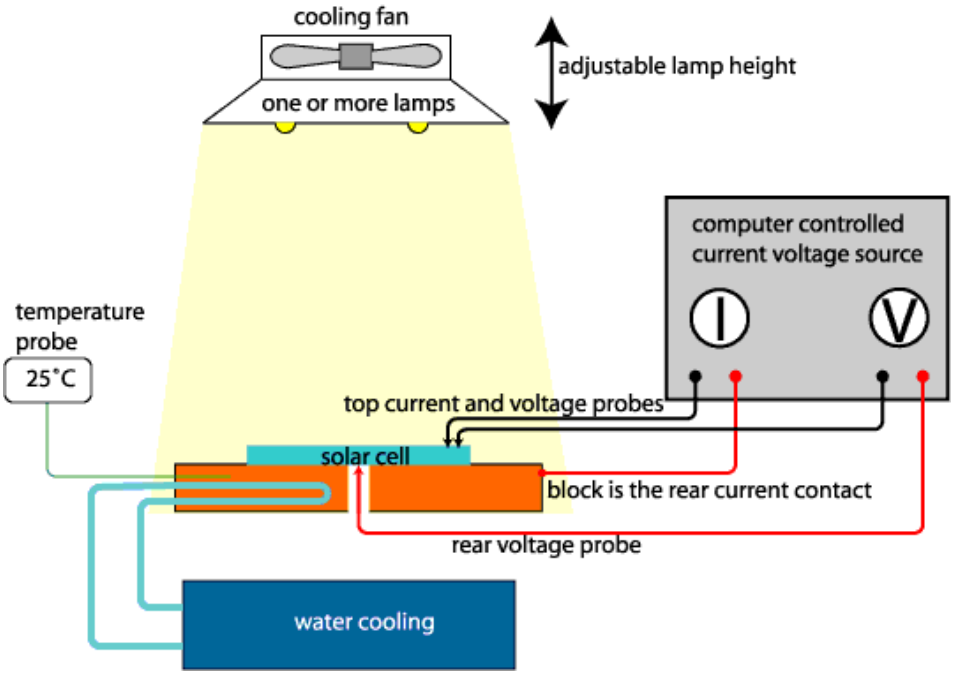

Figure 28. Basic design of a basic IV tester. To get around issues with contact resistance, the current and voltage are monitored independently.

[55]

The measurement of cell efficiency is the most basic method for characterizing solar cells. The comparison of devices produced at various businesses and laboratories using various technologies is made possible by standard testing.

The criteria for testing cells are:

- 100 mW/cm^2 of intensity (commonly referred to one sun's worth of light)
- Standard temperature of the cell: 25°C cell;
- Air mass (AM) 1.5 spectrum for terrestrial cells.

Building a system that simultaneously satisfies all the above-mentioned requirements is challenging and expensive. The modest, custom-built tests used in the majority of research labs only closely resemble the aforementioned circumstances. Results from "in-house" testing are frequently only rough estimates.
A consistent light source that closely resembles sunshine is necessary for measuring solar cells. The spectrum must also match a standard, in addition to the intensity. Utilizing the sun directly is a simple yet effective technique. This is a good solution 1 for sites with low cloud cover, but there are still variances in atmospheric conditions that need for adjustment when comparing readings across time. The period for testing is further constrained by the fact that the spectrum varies during the day.
Utilizing an artificial light source that simulates the sun is the most popular remedy [55].

3.7 External Quantum Efficiency Measurements

The "quantum efficiency" (Q.E.) of a solar cell is the ratio of the amount of carriers collected to the number of photons incident on the solar cell of a certain energy. The quantum efficiency can be expressed as a function of either energy or wavelength. The quantum efficiency at that specific wavelength is unity if all photons at that wavelength are absorbed and the ensuing minority carriers are collected. Photons with energies less than the band gap have a quantum efficiency of zero. The gold color square line depicts a quantum efficiency curve for an ideal solar cell [56].

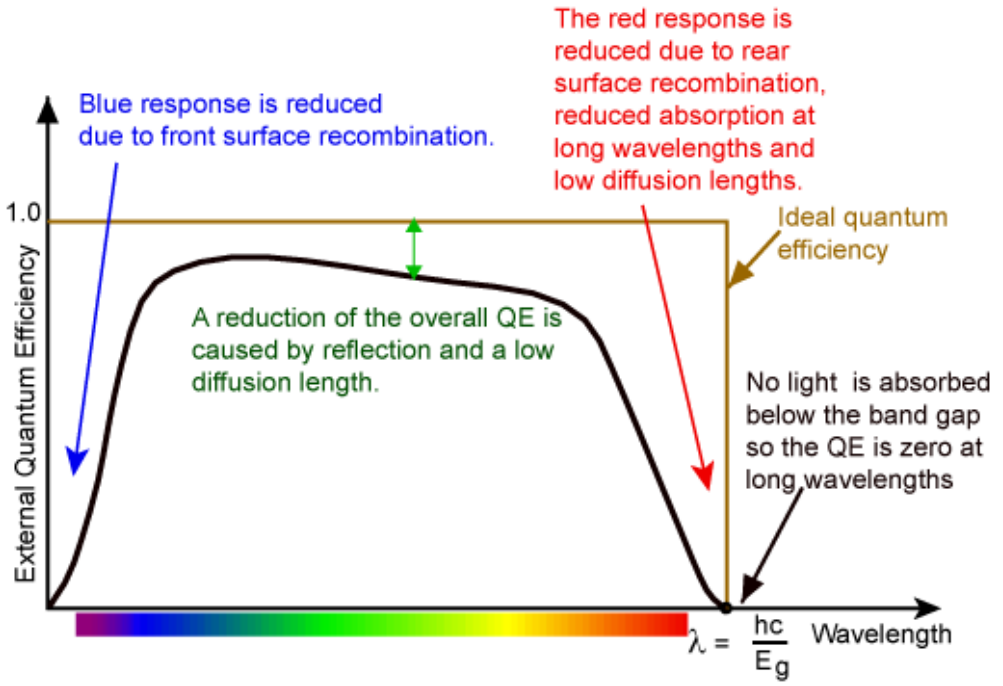

Figure 29. Illustration of an EQE curve.

Although the ideal quantum efficiency has the square form depicted above, recombination problems cause the quantum efficiency of most solar cells to be less than perfect. The quantum efficiency is influenced by the same forces that influence the collection probability. Since blue light is absorbed extremely close to the surface, excessive front surface recombination will have an impact on the "blue" component of the quantum efficiency. For instance, front surface passivation impacts carriers formed at the surface. Similar to how green light is absorbed in a solar cell's bulk, a low diffusion length will decrease the likelihood of green light being collected from the cell's bulk and lower the quantum efficiency in that region of the spectrum.

$$IQE = \frac{EQE}{(1-R)} = \frac{Electrons\ out}{(Photons\ in)\cdot(1-R)}$$

Where

IQE= Internal quantum efficiency and *R*= Reflectivity.

We can have typical values peak between 80-90% from moderate efficiency, IQE is strongly depending on wavelength and light.

The collection probability resulting from the generation profile of a single wavelength, integrated over the device thickness, and normalized to the incident quantity of photons at that wavelength, may be thought of as the quantum efficiency. Examining the quantum efficiency of the light that remains after the light that was reflected and transmitted has been lost is frequently helpful. The efficiency with which photons that are neither reflected or transmitted out of the cell can produce collected carriers is referred to as "internal" quantum efficiency. The exterior quantum efficiency curve may be rectified to produce the internal quantum efficiency curve by measuring the device's transmission and reflection [56].

3.8 Capacitance-Voltage (CV) technique

The capacitance-voltage (CV) and drive-level-capacitance-profiling (DLCP) approaches reveal the density of states in or near a diode's depletion area. This chapter delves into the theoretical foundations, assumptions, strengths and weaknesses, application, and analysis of these two related methodologies, CV and DLCP. The CV approach has received greater modeling attention. Both DLCP and CV profiling techniques are quite valuable; nevertheless, more complex analytical and numerical approaches would be beneficial. CV and DLCP can be effective techniques for analyzing and comparing material characteristics. These approaches have the potential to be improved further. The CV and DLCP approaches have made significant contributions to our understanding of semiconductor electronic characteristics. Given today's analytical, numerical, and experimental capabilities, it will be intriguing to observe how these approaches evolve and are applied to interesting new challenges in the future [57].

3.9 AST – Accelerated Stability Test

While the development cycle for new PV module designs can be as short as six months, photovoltaic (PV) modules have an intended service life of at least 25 years. This presents a challenge to both module makers, who must provide dependable, cost-effective modules, and investors, who must assess and manage the risk associated with unforeseen failures and deterioration, particularly for novel module designs [58].

An accelerated stability test is a valuable technique for determining device stability, but it may also aid in identifying the nature of problems through the interpretation of degradation behavior. The stability and behavior of our final devices were investigated using an accelerated stability test (AST) in a metal box at 80°C with one sun illumination.

Figure 30. Solar box of our laboratory.

Chapter IV
CZTS solar cell fabrication

Given the preliminary state of research and the variety of materials and approaches available, the project has the ultimate goal of achieving the development of a thin-film photovoltaic cell based on the CZTS compound, with new solutions for improved efficiencies and increased stability. This material has already given good results with fewer safety problems than similar compounds; many preparation procedures include a vacuum process, which typically necessitates the use of costly vacuum equipment. Non-vacuum techniques offer the benefit of being low-cost and simple to use. We began our own investigation on how to deposit CZTS thin films in non-vacuum conditions. In this chapter we face the preparation of the Ink solution in detail, the different deposition methods studied, and the detailed fabrication method of the devices.

4.1 Synthesis of the precursor solution

Following preliminary bibliographic research, we decided to start studying different methods for the synthesis of the precursor using different combinations of reagents. To use CZTS as an absorber for high efficiency thin-film solar cells, the manufacturing method for CZTS thin films must be improved. Several techniques are used to fabricate CZTS thin films including chemical vapor deposition, chemical bath deposition, chemical spray pyrolysis, electrochemical deposition, hydrothermal, spin coating, solvothermal, hot injection, solution route, doctor blading, combustion, deep coating, sol-gel, SILAR, sputtering, co-evaporation, pulsed laser deposition, vacuum thermal evaporation, nano-Ink etc. Grain size growth, adhesion, porosity, stoichiometry, thickness sustainability, and purity are the areas of expertise for each process [59].

Progress in the field of solution-processed (CZTSSe) solar cells has demonstrated the technique's promise as a scalable approach for the low-cost, high-throughput production of effective solar cells made from Earth-abundant materials. In fact, solution-processed procedures have demonstrated the highest power-conversion efficiency (PCE) for this material system to date, with record efficiencies reaching 13% vs 9.7% for vacuum-based processes. The advantages of these solution-processed solar cells are several in a variety of ways, including relatively low-energy, non-vacuum processing for the CZTSSe absorber layer and low-cost/high-throughput solution deposition of this layer via roll-to-roll production. Furthermore, the difficulties associated with absorber stability and elemental volatility during high-temperature processing make solution-based approaches especially appealing for CZTSSe production [60].

One of the most crucial components is the solvent, which must dissolve Cu-, Zn-, Sn, and if feasible, chalcogen-containing compounds and not leave any deleterious impurity elements in the CZTS(Se) layer after the annealing stage. Many secondary characteristics should be addressed, including surface tension, volatility, reactivity, toxicity, and cost. Due to the ionic character of the metal compounds to be dissolved, only polar solvents were utilized in the production of "our" kesterite. An appropriate solvent should be able to coordinate metal cations in the precursor solution by creating

soluble complexes that dissolve completely after heat treatment without leaving undesired contaminants [61].

Several organic solvents, including alcohol combinations, ethylene glycol, 2-methoxyethanol, and dimethyl sulfoxide (DMSO), have been investigated for the synthesis of the precursor solution. Metal salt solutions in alcohols and diols tend to leave carbon residues after drying and annealing procedures; 2-methoxyethanol (b.p. 124°C) is a solvent with mixed polar and non-polar properties that may be used to dissolve reagents with varying ionicity/covalency, such as ionic metal salts in the presence of organic additions such as amines.

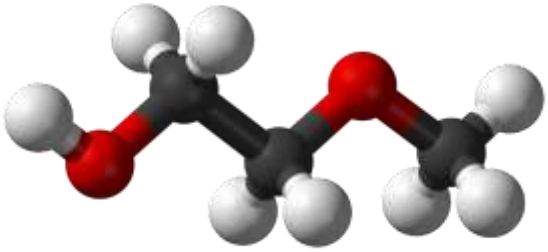

Figure 31. Structure of the 2-methoxy ethanol chosen as final solvent.

DMSO (b.p. 189°C) is a polar aprotic solvent capable of dissolving considerable amounts of thiourea or thioacetamide as well as the required metal salts. DMSO is miscible with most major organic solvents and dissolves a wide spectrum of organic and inorganic compounds.

DMSO acts as a Lewis base, bonding with metals via the oxygen or sulfur atoms to generate metal-organic complexes. It also includes sulfur, which is too inert to serve as a good sulfur source during the sulfurization stage. Thiourea is therefore added to the precursor solution to assure the existence of reactive chalcogen. Cu, Zn, and Sn salts such as chlorides, nitrates, acetates, and iodides are readily accessible in high purity and frequently utilized due to their solubility in a wide range of solvents. Because many salts are hygroscopic, hydrates are frequently used to facilitate processing and prevent weight uncertainties. Copper (II) salts are favored over copper(I) compounds because they are less soluble and can oxidize or disproportionate, resulting in insoluble precipitate. After the final annealing stage with chalcogen, regardless of the original copper oxidation state, it takes the Cu(I) state in the kesterite phase.

Metal losses, such as Zn and Sn, may occur during the annealing stage, thus the initial precursor concentrations must be adjusted appropriately.

Figure 32.Two precursors' solutions tested.

In order to stimulate the production of kesterite during the annealing process, a source of chalcogen (S or Se) should be present in the initial precursor solution. The chalcogen source has been either sulfur, thiourea, or thioacetamide. Thiourea is a popular option because it is soluble in a wide range of polar solvents and can coordinate metal ions in solution. Other than metal compounds, no other solute components are often required in the initial solution, and they are avoided whenever feasible due to the possibility of further carbon or oxygen contamination. However, additives such as complexing agents, binders, pH stabilizers, antioxidants, surfactants, and other rheology-adjustment agents are used to provide good coating qualities. For stable solutions, monoethanolamine (MEA) or diethanolamine (DEA) as a complexing agent was required, especially when the solvent could not properly coordinate metal cations.
The amines breakdown completely and can serve as antioxidants [61].
During this project alternative inks have been developed and applied, the best results are obtained with these experimental details: copper (II) acetate monohydrate (0.574 M), zinc (II) acetate dihydrate (0.375 M), tin (II) chloride (0.3 M), and thiourea (2.4 M) are dissolved in 2-methoxy ethanol to make the CZTS-precursor solution. As a stabilizer, diethanolamine (DEA) is also utilized. Following extensive adjustment, the Cu/(Zn + Sn) and Zn/Sn ratios are set at 0.85 and 1.25, respectively [62].
Thiourea is a simple chemical molecule with a high degree of crystallographic symmetry. Its rhombic system crystal structure makes it a suitable ligand. Thiourea and transition metal complexes can be combined to generate stable complex cations.

4.2 Study of different depositions method

Stable deposition processes are required for the manufacture of solar cells in order to achieve uniformity, stability, and high efficiency. There are several coating processes that are compatible with a wide variety of solutions with varying rheological qualities. In other words, selecting an acceptable coating procedure should not be difficult as long as the chosen solution can be turned into a high-quality kesterite material following the final heat treatment. In our research laboratory relevant coating methods have already been employed on kesterites include spin coating, doctor blading, spray coating, dip coating, different printing techniques[61].

Dip-coating is likely the most basic approach for experimenting with novel solution chemistry. However, this approach is not preferred since both sides of the substrate are coated, and the wet layer is often thin, on the scale of 10-100 nm, necessitating numerous and sometimes inhomogeneous coats.

Another laboratory-scale technique that can be used for highly viscous fluids exceeding 105 cps (liquids are given a viscosity value called centipoise (CPS), it is a measure of dynamic viscosity, which is the kind of viscosity we typically think of) is doctor blading. By coating on hot substrates and by applying multilayer coatings the wetting of the substrate by the precursor is improved and the layer is more homogenous. We applied of the precursors with different additives to improve the surface tension, but the samples showed inhomogeneity in the solution.

Ink jet is a quick printing processes that work well with roll-to-roll deposition on flexible substrates. While mechanical scribing and laser ablation are the most prominent patterning technologies today, patterning by printing can minimize the number of processing stages. It is a flexible deposition technique for creating functional layers from homogenous molecular or colloidal liquid phase dyes. The working concept is based on the controlled characteristics and accurate deposition and fixing of inks as droplets from a nozzle onto a target substrate. Inkjet printing technique, which depends on the production of stable droplets, heavily depends on the ink's qualities.

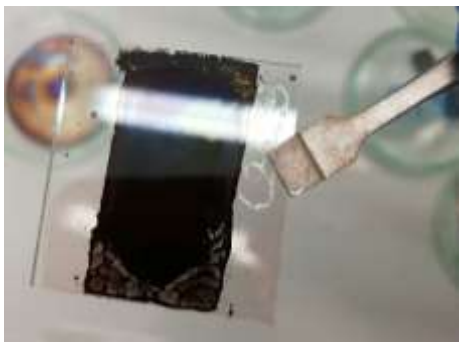

Figure 33. Doctor Blade deposition sample.

The actions that take place once ink-drops successfully land on a substrate are what determine if inkjet printing is effective. During the drying processes that result in a continuous film creation, the interactions between the substrate and droplet might affect the drop spreading, coalescing, solidification, and eventually film uniformity. The process of film formation may be controlled by the interaction of the substrate and ink drop qualities based on certain factors, such as the contact angle of a drop on a substrate and surface roughness. The printing quality may be effectively controlled by adjusting the printing settings, including the delay duration and drop spacing. The capillary, viscous, and gravitational forces, wet ability effects, and the underlying heterogeneous pore geometry are some of the complicated interactions that cause the viscous fingering instability, which can to the creation of preferred flow paths in ramified fingering networks [63].

With the collaboration of a printing company, we printed our ink with a thermal inkjet 2.5 (TIJ) printing machine.

Figure 34. TIJ printing system.

This kind of printers use cartridges which are very easy to replace. We filled the cartridges with our ink and did several printing tests to optimize the printing parameters to obtain a homogeneous layer.

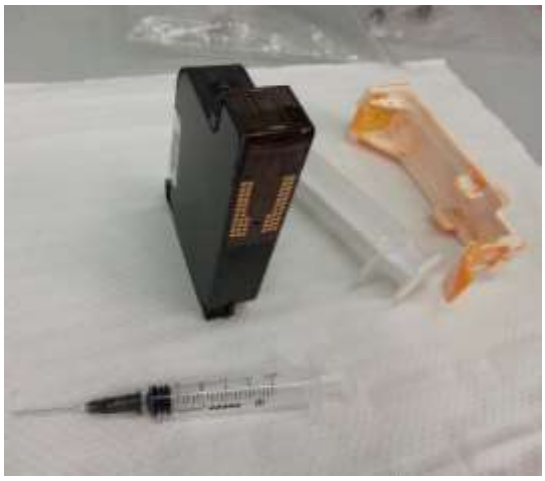

Figure 35. Ink-filled cartridge with precursor solution.

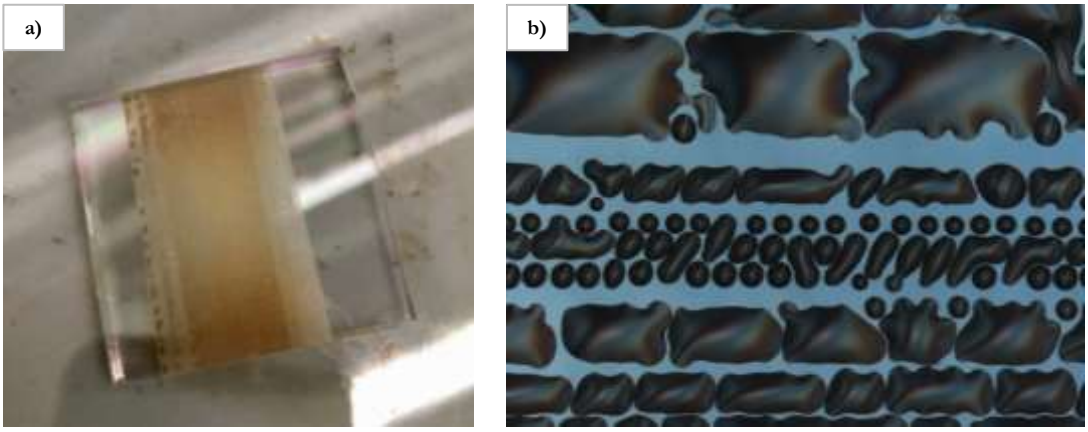

Figure 36. a) Test sample printed with precursor ink 1 layer 300| 600 DPI b) microscope image of ink deposition pattern on substrate surface.

The main parameters that were changed to achieve a homogeneous layer are as follows: resolution, speed, voltage, head position. Each print resolution had a speed limit; if the speed limit for the set resolution is exceeded, your output will not only lose quality but will also be stretched. Several combinations between the above factors and using some innovative wetting additives to reduce the surface tension have been combined, but we found limitations in this technology in arriving at the desired result.

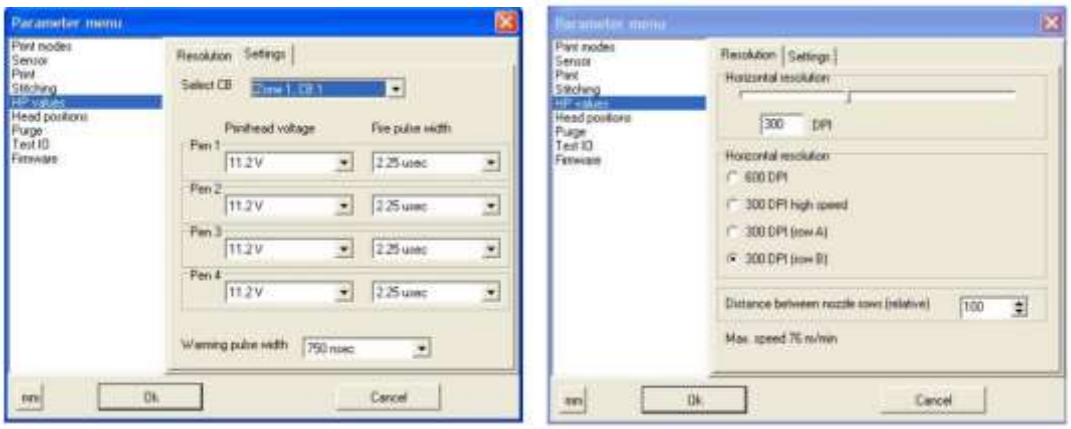

Figure 37. Print modes: some of the modified parameters.

We therefore turned our attention to the spin coating deposition method; thin layers can be placed all at once, and repeated coats with interim drying are used to produce the required layer thickness. After several experiments, we have optimized the process, and we found the best result by carrying out spin coating at 2400 rpm for 15 s and

subsequently drying on a hot plate in air at 300° for several minutes. This technique is applied 5 times to increase the thickness of the film.

Figure 38. The two spin coating system used and the step of the process.

4.3 Device fabrication

CZTS precursor films are made in our laboratory on cleaned soda lime glass (SLG) substrates coated with a molybdenum (Mo) bilayer as a back contact and deposited by RF sputtering (Mo target by Testbourne Ltd 99.95% pure).

Because it does not react significantly with CZTS, Mo produces a low-resistivity ohmic contact to it, and its conductivity is not reduced when CZTS is deposited on hot substrates, Mo has a higher conductivity and is more physically and chemically stable than other materials including W, Ta, Nb, Cr, V, Ti, and Mn.

Figure 39. A molibdenum sample just deposited by RF sputtering, on the right a deposition moment (target).

The vacuum chamber's base pressure is $5 \cdot 10^{-6}$ mbar. A quartz crystal microbalance measures thickness and sputtering rate. The first, stickier 700 nm thick Mo layer is formed at a pressure of $1 \cdot 10^{-2}$ mbar with a power of 100 W, while the second, more conductive 500 nm thick Mo layer is deposited at a pressure of $3 \cdot 10^{-3}$ mbar with a power of 150 W. The substrate temperature is kept constant at 200°C for both layers. To deposit the CZTS thin film, 2-methoxy ethanol is mixed with zinc (II) acetate dihydrate (0.375 M), copper (II) acetate monohydrate (0.574 M), tin (II) chloride (0.3 M), and thiourea (2.4 M).

As a stabilizer, diethanolamine (DEA) is also added. This precursor solution is then spin coated at 2400 rpm for 15 seconds on the Mo stack and dried at 300°C in air for 5 minutes on a hotplate. We measured a 1.6 μm thick absorber layer with a Dektak profilometer after iterating the deposition process for 5 times.

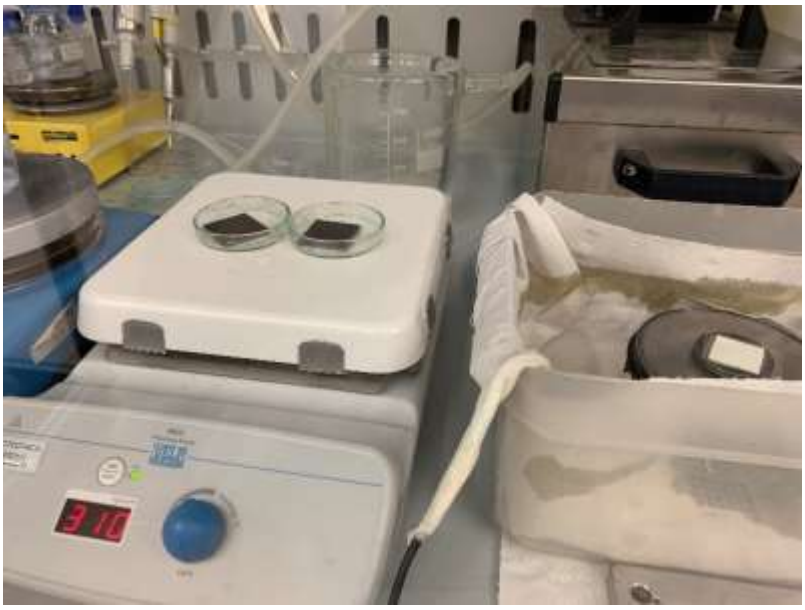

Figure 40. Drying of the samples after spin coating.

The CZTS precursor films were annealed at 450°C in selenium atmosphere to complete the phase formation and to incorporate Se into the CZTS lattice.

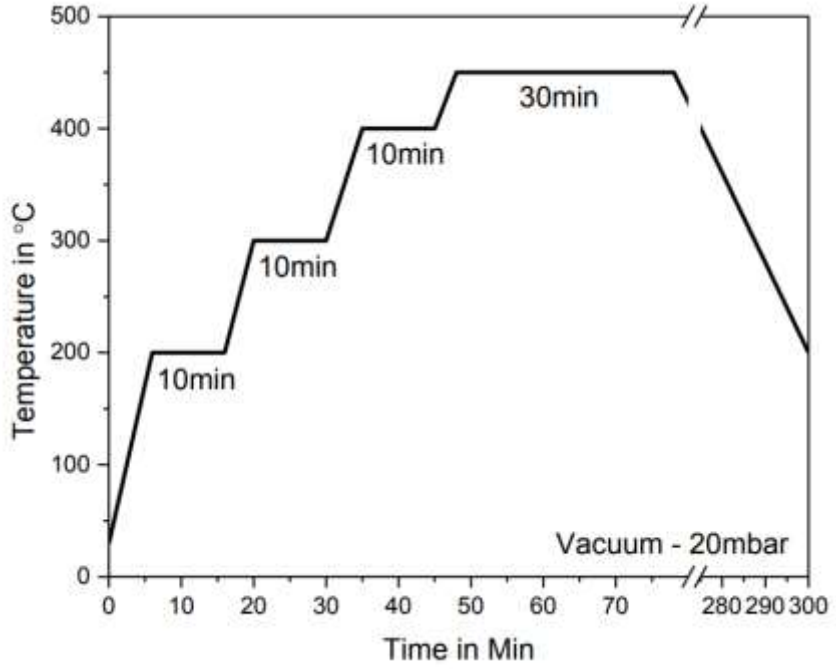

Figure 41. Schematic of the selenization process's annealing phase.

[62]

Figure 42. A detail of the annealing process, samples being cooled.

A 60 nm thick CdS buffer layer is deposited at 60°C by chemical bath deposition, in particular 15 ml of Cd $(CH_3COO)_2$ $2H_2O$ (0.025 M) solution, 10 ml of thiourea (0.422

M) with 25 ml of NH_4OH (20%) solution are mixed into a glass with 200 ml of distilled water [64].

The buffer layer joins the absorber layer while allowing the most light possible to enter the junction area. In heterojunction solar cells, the absorber layer serves as the main component, while the buffer layer does not produce photocurrent. Materials like Zn(O,S), CdS, and In_2S_3 are frequently regarded as the most promising options for buffer layers [63].

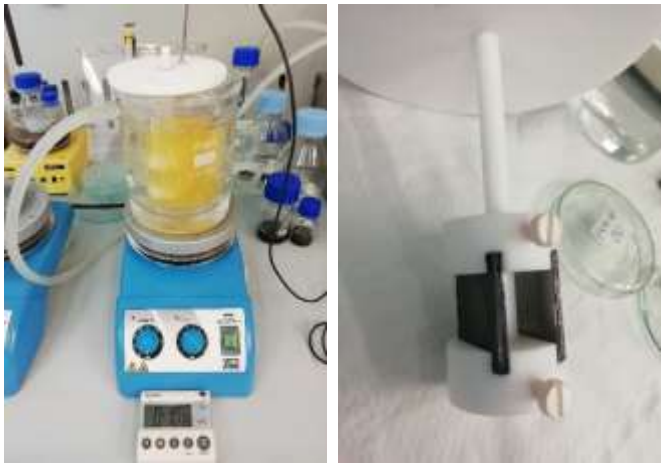

Figure 43. Two samples undergoing chemical bath for buffer layer deposition.

ITO and ZnO layers are deposited in the same RF-sputtering machine, with a substrate temperature of 150°C and with an oxygen flux of 0.5 sccm, respectively with a power of 160 W and 60 W. Finally, the solar cell is fabricated with the following structure: SLG/Mo/CZTSSe/CdS/ZnO/ITO [64].

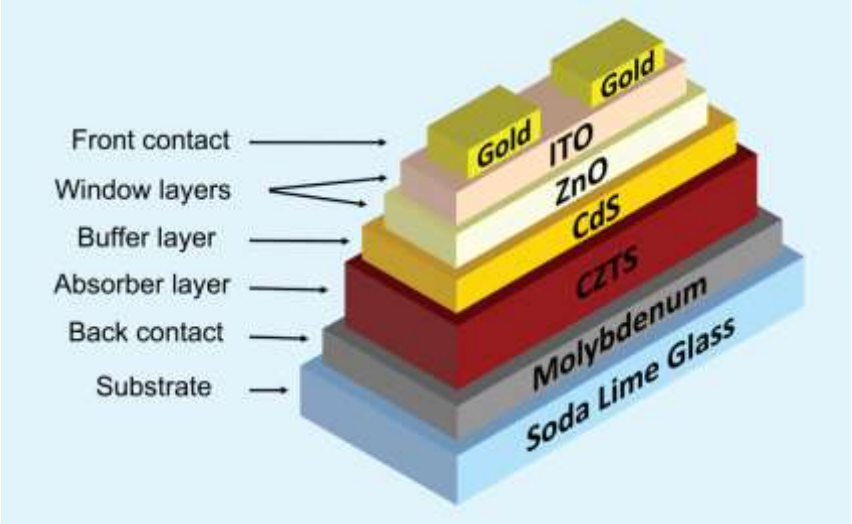

Figure 44. Structure of the device.

To attain high energy conversion efficiency, a solar cell's ohmic losses should be as low as feasible; the quality of solar cell contacts greatly impacts the amount of such losses, hence improving solar cell contacts is a critical step in producing high-performance solar cells [65]. Top-contact metallization is crucial because it reduces shadow loss and enables the use of monolithic interconnection. The front metal grid has traditionally been deposited using evaporation and a shadow mask [63].

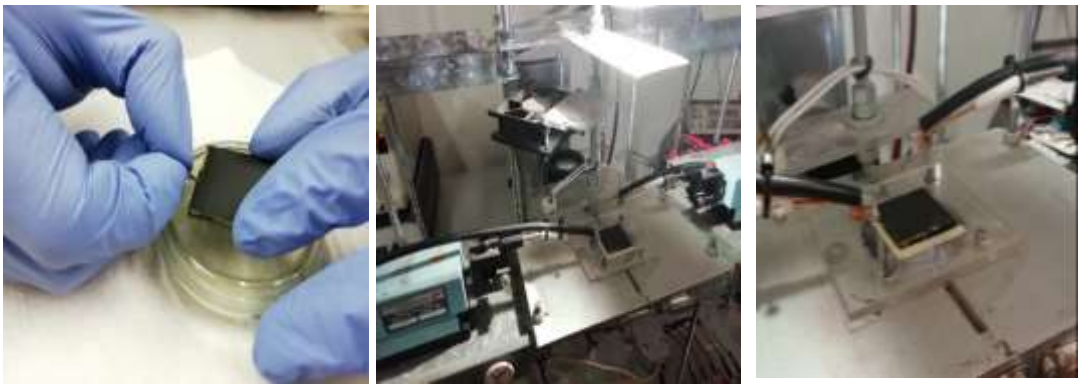

Figure 45. Preparation of the cell for measurement of its optical performance.

Chapter V
Process optimization

Manufacturing of solar devices must be continually updated to enhance the efficiency-to-cost ratio of photovoltaic solar cells. Typically, efficiency optimization is done process by process.

The present chapter act upon device optimization focused to analyze and study the factors that influence the device performance and the physical properties.

The drying time and the annealing temperatures in non-vacuum processes can be very important for the photovoltaic properties of the devices.

A very important role is also played by doping; a very simple method of including doping elements that can positively modify the structure and electrical properties of CZTS has been tested and is presented.

Another window layer is also tested and presented: TiO_2.

5.1 Analysis of the influence of drying time for precursors layers

Although it is true that drying is a basic, conventional step in solvent evaporation, it is shown to be critical for layer shape, homogeneity, and the presence of impurity components and phases in the final CZTS(Se) layer. Drying begins when the wet film is applied, however it is normally done as a distinct phase.

Wet layers are frequently dried over several minutes on a hot plate at temperatures ranging from 200°C to 350°C. On the one hand, the drying temperature is chosen to be as high as feasible in order to enhance solvent evaporation and eliminate carbon, but it is limited by the oxidation of the precursor material as well as the molybdenum substrate.

To guarantee thorough solvent evaporation, it is necessary to use a somewhat high drying temperature. The coffee-ring effect[2] may also be prevented by covering a pre-heated substrate with a thin layer of surfactants to lower surface tension.

Film cracking may result from the tensile tension generated during the removal of the solvent and the organic components. Since they can produce shortcuts between the top and back contacts, microscopic fissures in the dried layer that spread over its whole thickness can be disastrous for the solar cell absorber. If the film thickness surpasses a "critical thickness," which is inversely related to the tensile stress and the film's Young's modulus, the phenomena is quite obvious. The multi-layering strategy used for spin coating has been shown to be a successful means of preventing tiny fractures and enhancing layer uniformity. This is due to the fact that each layer is thinner than the critical thickness, and a drying period in between coatings aids in the complete evaporation and breakdown of solvent species. Compressive stress can also be seen in the final absorber layer if a dried precursor has a volume expansion during the last chalcogenation stage, leading to "bulges" rather than fractures [61].

The current work highlights the impact of precursor drying conditions on device performance and suggests a solution-based method for creating kesterite films that are both cost-effective and of high device quality.

[2] A "coffee ring" is the pattern that an evaporating puddle of liquid with particles leaves behind. The name of the phenomena comes from the distinctive ring-like deposit that forms around a coffee spill. The coffee ring effect, or occasionally the coffee stain effect, or simply ring stain, is the name of the process that results in the production of this and other rings[87].

As we described in paragraph 4.1, copper (II) acetate monohydrate, zinc (II) acetate dihydrate, tin (II) chloride, and thiourea were dissolved in 2-methoxy ethanol and diethanolamine to synthetize the precursor solution. None of the compounds were further purified before usage. Diethanolamine acted as a stabilizer, and 2-methoxy ethanol served as the solvent; the solution was also filtered. Spin coating was performed at 2400 rpm for 15 s, and it was then dried at 300°C for 3, 5, and 10 minutes, respectively.

In order to analyze the effect of the drying process on the device, we considered three different drying times and the samples were named as follows: DT03 (3 minutes), DT05 (5 minutes), and DT10 (10 minutes) where DT stands for drying time.

To complete phase formation and introduce selenium into the CZTS lattice, the CZTS precursor films were annealed at 450°C in a selenium environment. The solar cell is then constructed using the following structure: SLG/Mo/CZTSSe/CdS/ZnO/ITO.

The structural and optical properties of the films were analyzed by X-ray diffraction (XRD) (Thermo ARL X'TRA powder diffractometer in Bragg-Brentano geometry, equipped with a Cu-anode X-ray source (Kα, λ = 1.5418 Å) and Peltier Si (Li) cooled solid-state detector) and Raman (Horiba Jobin-Yvon LabRam HR800 microprobe setup in backscattering geometry, He-Ne laser at 632.8 nm) spectroscopies. SEM and energy dispersive X-ray spectroscopy (EDXS) were used to examine the surface shape and composition of the films (Philips FEI XL30 Scanning Electron Microscope). We also performed atomic force microscopy (AFM) analysis (NT-MDT Solver Pro).

CZTSSe absorbers on Mo/glass substrates were examined and compared in terms of structural and compositional properties using the same process steps but with the aforementioned differing drying durations. The XRD patterns were analyzed using ICDD (international center for diffraction data), specifically the files PDF N° 066-0163 (CZTSe), PDF N° 026-0575 (CZTS), and PDF N° 42-1120 (Mo).

The figure below (Figure 46 (a)) shows XRD patterns of CZTSSe layers dried at various time intervals before to annealing in selenium environment (as deposited).

We can see that the dried precursor has a CZTS structure even before annealing. The as-deposited films do, in fact, display the normal CZTS compound peaks, but without selenium. The XRD peaks produced by the samples with various drying durations are comparable. The stoichiometry and structure are independent of the drying periods.

The low reflection intensity and large peak shapes for all three samples show that the CZTS compound has very poor crystallization quality. The underlying molybdenum substrate's peaks are also identified. After selenization, the films (deposited at various drying times) were examined; the XRD patterns are shown in Figure 46 (b).

One peak of the molybdenum substrate is once more observed, and all of the reflections are consistent with the CZTSSe compound, thus demonstrating the existence of selenium in the matrix. This pattern exhibits sharper, higher-intensity peaks than the previous one; it is evident that the compound recrystallized as a result of the annealing process in the presence of selenium. The existence of secondary phases, however, might not be distinguished by XRD [62].

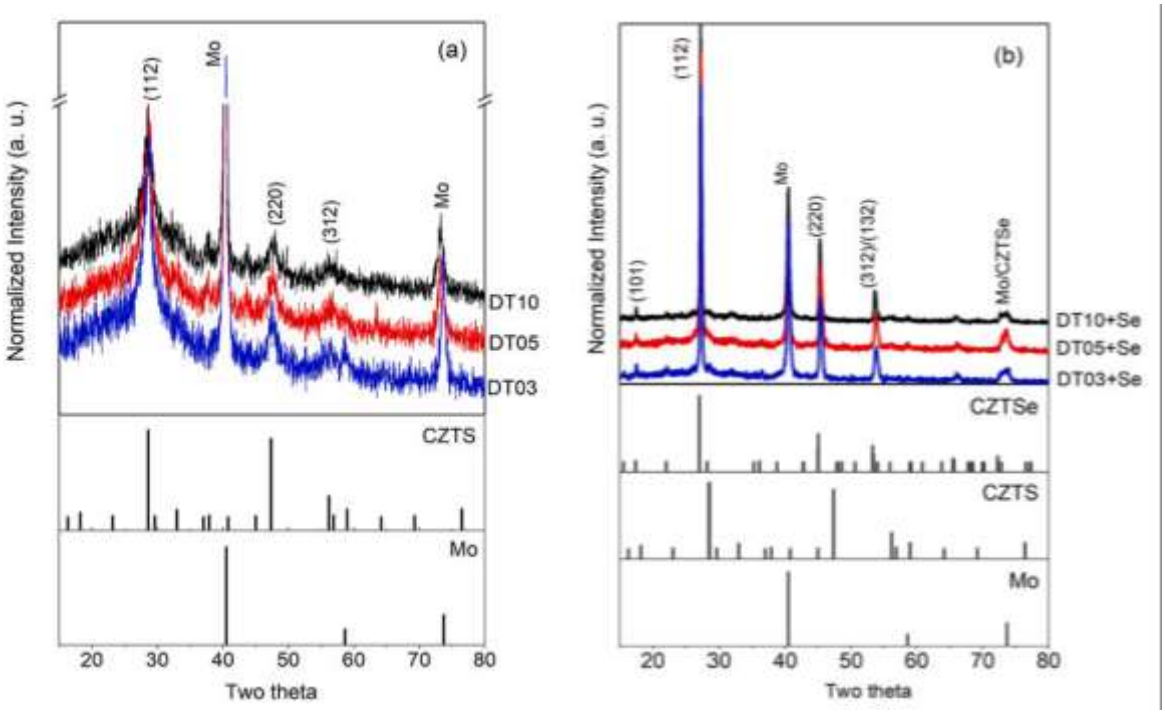

Figure 46. XRD spectra: (a) Spin coated sample at 3 different drying conditions (b) Selenized samples.

We examined the surface with AFM and SEM spectroscopies. Figure 47 displays the AFM images of dry CZTS films that have been deposited and selenized after 3, 5, and 10 minutes. In comparison to the samples made using the other two DT, the films that were deposited at 3 min display bigger conglomerations. Additionally, the

morphologies of the DT05 and DT10 samples vary. The grains are bigger (with an average grain size of one micron) after selenization.

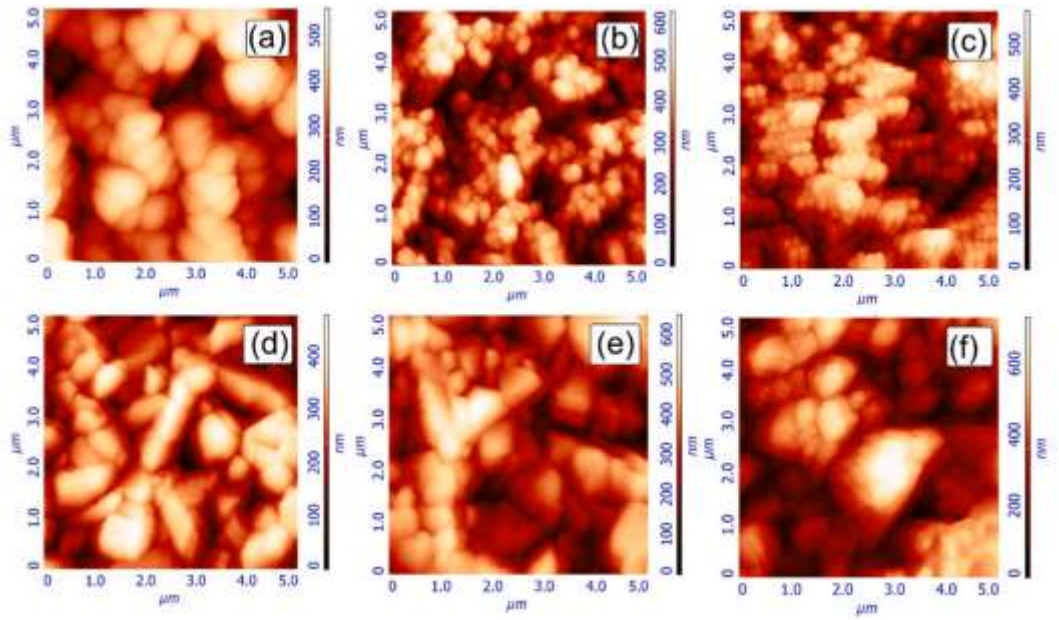

Figure 47. AFM pictures of the films after deposition (a) drying time 3 minutes DT03, (b) drying time 5 minutes DT05, (c) drying time 10 minutes DT10, (d) DT03 +Se, (e) DT05 + Se, (f) DT10 + Se.

Figure 48 displays SEM images of dried selenized CZTS films after 3, 5, and 10 minutes. The morphology significantly changes as drying time increases. Compared to films dried for 10 min, those dried for 3 min and 5 min display a more compact shape. Therefore, prior to annealing, the samples exhibit poor crystallization and an uneven structure (as shown by EDX). All three examples exhibit crystallization after annealing, however the DT05 sample exhibits a more compact and substantial structure, whereas the DT10 sample exhibits more porosity and the DT03 sample exhibits smaller grains. Point flaws make up the majority of the kesterite material's inherent p-type (vacancies, anti-sites and interstitials). An off-stoichiometric sample preparation is responsible for the generation of necessary point defects.

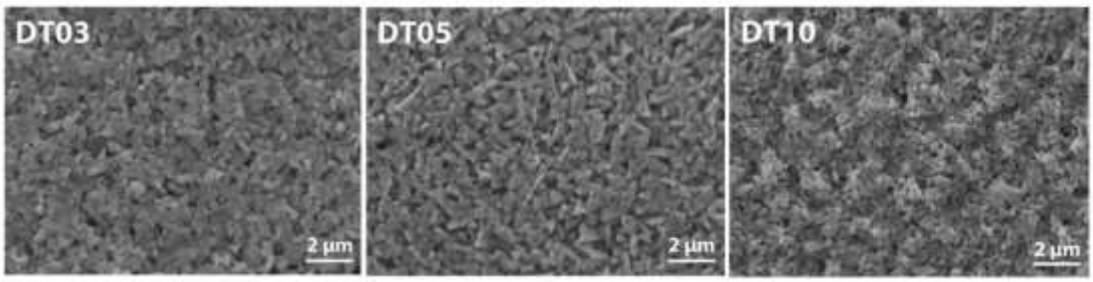

Figure 48. SEM photos of the DT03, DT05, and DT10 selenized CZTS films.

The typical CZTS structure as seen by SEM has grains that are compact with few grain borders and polycrystals that are roughly one micrometer in size. The 5-minute drying time absorber's EDXS analysis reveals a Sn-rich composition with a 0.56 Zn/Sn ratio. The tests also show that selenium treatment significantly incorporated Se into the crystal lattice (S/Se=0.14) (Figure 49) [64].

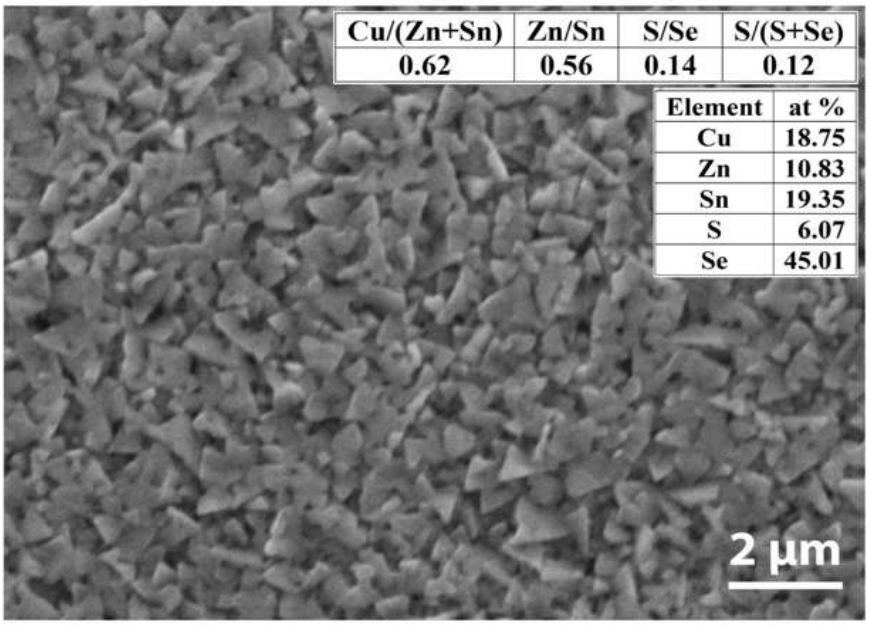

Figure 49. CZTS films selenized at 450°C with precursors dried for 5 minutes: SEM picture and EDXS results.

Table 2. EDX results of the selenized films.

	Atomic percentage of elements and calculated ratio (at %)								
Sample	Cu	Zn	Sn	S	Se	Cu/(Zn+Sn)	Zn/Sn	S/Se	S/(S+Se)
DT03	20.95	12.53	11.07	19.16	36.27	0.89	1.13	0.53	0.35
DT05	18.75	10.83	19.35	6.07	45.01	0.62	0.56	0.13	0.12
DT10	18.89	8.41	22.61	2.46	47.63	0.61	0.37	0.05	0.05

The Raman spectra of as-deposited CZTS films with various drying times are shown in Figure 50(a), normalized to the (1 1 2) peak. We can see three peaks, corresponding to the Cu_2SnS_3 (CTS), Cu_2ZnSnS_4, and Cu_2-xS phases respectively at 297 cm^{-1}, 335 cm^{-1}, and 470 cm^{-1}.

The DT10 case has very little CTS peak. Raman peaks at 335 cm^{-1} are present in both CZTS and tetragonal CTS structures, making the contribution unclear based on a superficial study [66].

The peaks at 297 and 335 cm^{-1} are different for the three situations, however, if we pay closer attention to the spectra DT10's primary peak is at 332 cm^{-1}, whereas DT03's is at 339 cm^{-1}. The peak that is displaced to the right can be assigned to CZTS, whereas the peak that is relocated to the left should be attributed to CTS.

Additionally, DT03 and DT05 have a peak at 289 cm^{-1}, which is once more associated with the CZTS structure; however, CTS is also associated with a peak that looks similar but approaching 297 cm^{-1}. In summary, DT03 and DT05 have a CZTS structure, but DT10 has a greater relationship to CTS [67].

The three distinct drying times for the selenized CZTS films are shown in figure 50(b) at an excitation wavelength of 632 nm. Seven peaks are observed at 175 cm^{-1}, 197 cm^{-1}, 238 cm^{-1}, 330 cm^{-1}, and 349 cm^{-1} that correspond to the B, A, B(LO), A, and E (TO) vibrational modes of the CZTSSe phase, which is a combination of the CZTS and CZTSe phase[68][69][70][71][72].

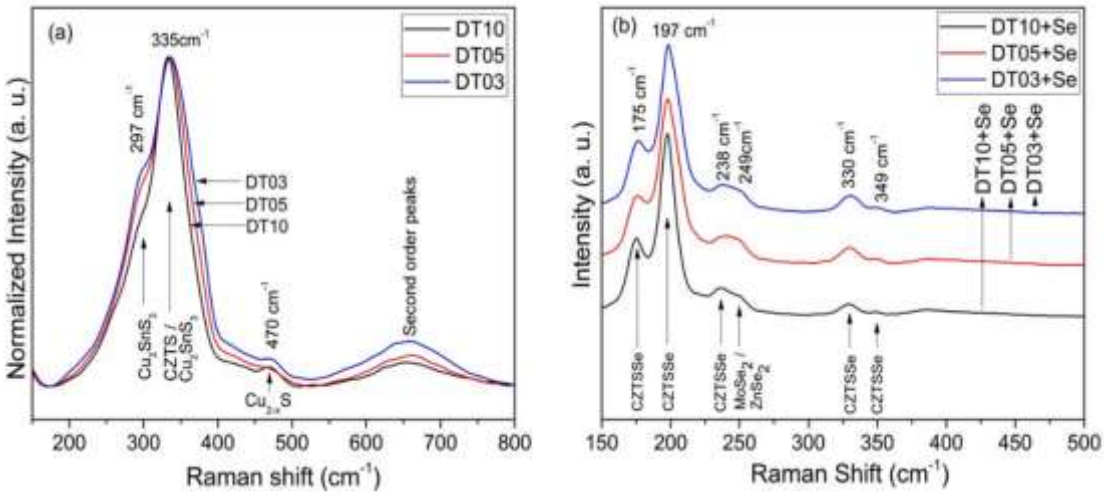

Figure 50. CZTS thin films (a) as-deposited and (b) selenized varying drying-time Raman spectra (excitation wavelength of 632.8 nm). The selenization change radically the pattern.

Both $MoSe_2$ and $ZnSe_2$ structures contain Raman peaks at this wavenumber, although it is unclear what role this new peak at 249 cm^{-1} plays. In any event, it is obvious that this additional peak results from the interaction with selenium [73].

The scattering from $MoSe_2$, which develops at the CZTSSe/Mo interface during the selenization process, is the primary cause of the Raman peak in this range (Khare et al., 2012). The three patterns are quite similar in relation to the three drying durations, however DT10 exhibits a sharper A vibrational mode and DT05 exhibits a shift of the B vibrational mode towards higher cm^{-1}[74].

If we take a deeper look at this Raman spectrum, focusing on the 175 cm^{-1} and 197 cm^{-1} peaks (Figure 51), the DT03 sample clearly shifts these two peaks, indicating a greater quantity of S and, thus, a higher S/Se ratio in this instance [67].

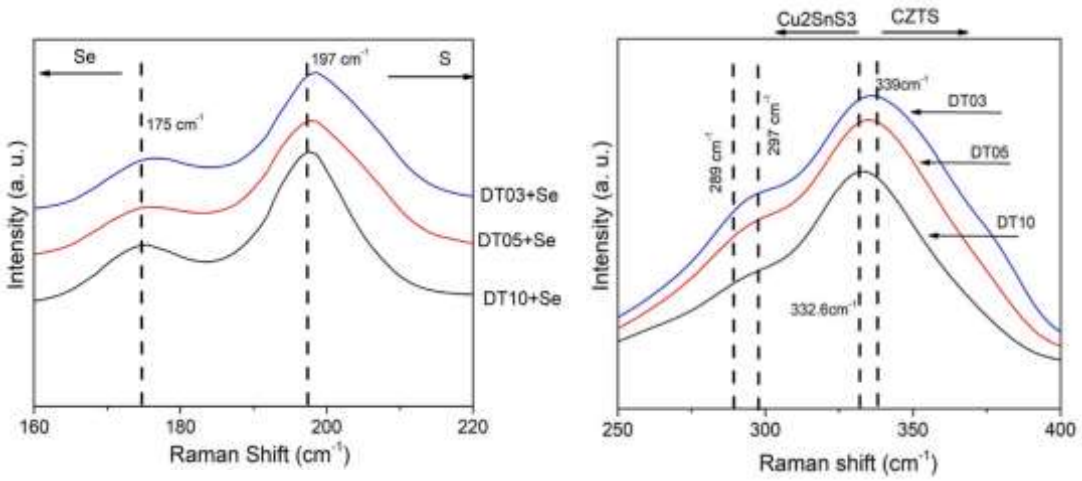

Figure 51. Spectrum of Raman upscaled from Figure 50: the shift of the 175 cm^{-1} peak show a greater suflur content for the DT03 sample.

With this last extra wavelength, a shallower profile is feasible since the penetration depth of 632.8 nm is greater than that of 514.5 nm laser; the penetration depth would be 20–30 nm deeper with the longer wavelength.

A larger view of the potential various phases is also provided by using a different wavelength. The characteristic CZTSSe phase peaks can be seen in the Raman spectra produced with a 514.5 nm laser, although DT03 has a somewhat higher peak for 236 and 329 cm^{-1}, whereas DT10 and DT05 have fairly comparable (relative) peak intensities. With a shorter excitation wavelength, the 249 cm^{-1} peak vanishes proving that the peak was ultimately caused by the $MoSe_2$ phase that was seen at the Mo/CZTSSe contact [66].

On a lower wavelength scale, the micro-raman maxima at 174 cm^{-1}, 197 cm^{-1}, and 235 cm^{-1} are shown. With the exception of DT05, where the 174 cm^{-1} and the 235 cm^{-1} are displaced, the peaks are all in the same location. This indicates that the DT05 case has a greater sulfur content.

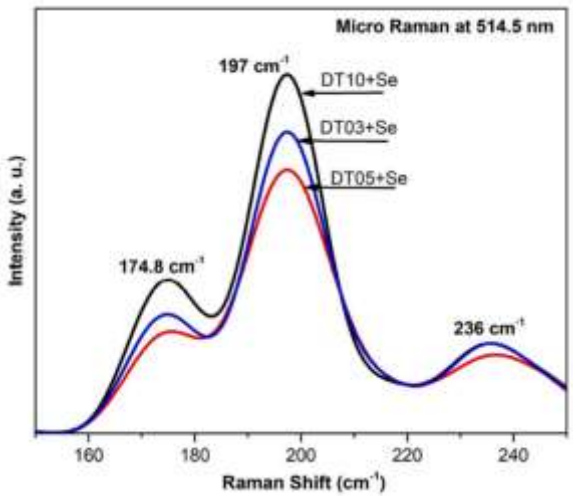

Figure 52. Upscaled micro Raman spectra of selenized CZTS with different drying time; the DT05 sample show a greater sulfur content.

The aforementioned standard device structure was used to set up CZTSSe solar cells, which have an active area of 0.16 cm^2 and have been measured under AM 1.5. According to the graph (Figure 53), the best results are obtained with a drying period of 5 minutes and the following values for V_{oc}, J_{sc}, and FF: 321 mV, 30 mA/cm^2, 51%,

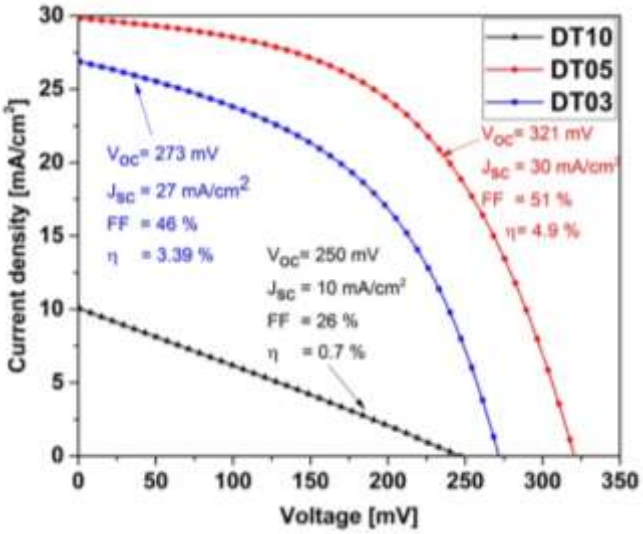

Figure 53. The JV properties of CZTS thin films dried after 3, 5, and 10 minutes.

and 4.9%, respectively. This demonstrates unequivocally that process stages that might appear inconsequential, such as the precursor's drying time, can contribute to the optimization of the CZTS process.

Additionally, cells have been tested at 80°C and one sun in a specific enclosure for hundreds of hours. Due to this, a light soaking effect that increases efficiency has been demonstrated. Particularly, the fill factor increases significantly, indicating the passivation of several potential carrier traps while also demonstrating the great stability of the devices.

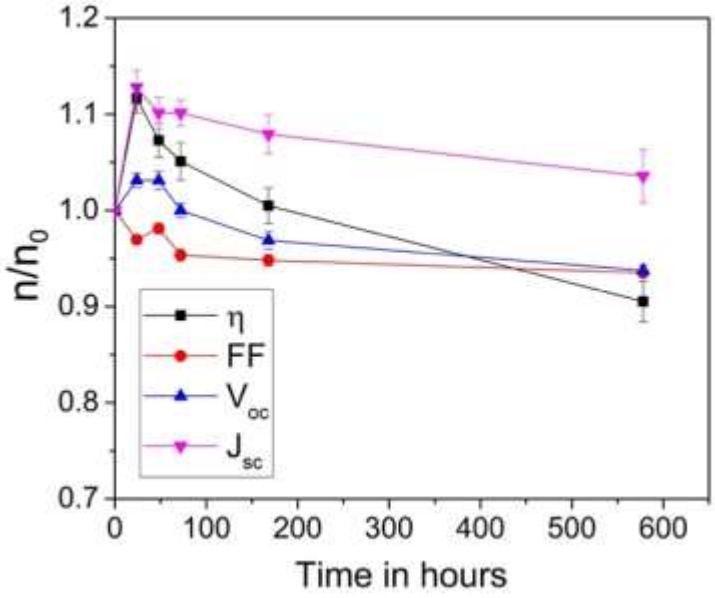

Figure 54. Tests of the CZTSSe solar cell's accelerated lifespan stability with a 5-minute drying period; data adjusted to beginning values.

5.2 Analysis of the annealing temperature at different atmosphere

The last processing step, annealing, can be carried out in either a reactive or inert environment. The reactive, chalcogen-containing environment has a variety of effects. First, by increasing the S(Se)/Me ratio to 1:1, reactive annealing can make up for the lack of chalcogen in the dried precursor layer. Due to the negative effects that anion vacancies might have on deep donor levels, this requirement is essential for a phase-pure material with appropriate electrical characteristics. Second, during annealing, the interaction with chalcogen may cause a volume expansion and densification, eradicating the layer porosity and enlarging the grain size. The chalcogen vapor overpressure is also necessary to avoid the breakdown of the kesterite phase into volatile SnS(Se) and SnS(ZnS) and binary copper and zinc chalcogenides (Se). The maximum annealing temperature normally falls between 470 and 550°C. However, the kesterite phase can develop via intermediary phases and begins at a lower temperature [61].

At the beginning of this study, we designed an annealing chamber to perform heat treatment in the furnace. The resulting samples were not satisfactory because the chamber could not perfectly support the vacuum generated and part of oxygen flow into the chamber thermally damaging the samples.

Figure 55. Home-made annealing chamber.

After that the annealing process, as explained in paragraph 4.3 has been conducted in a single zone furnace.

Phase purity and surface morphology were extensively investigated as we investigated the impact of selenization temperature and annealing environment on the CZTS films. By using X-Ray diffraction (XRD) and Raman spectroscopy, structural characteristics and phase purity of the CZTS precursor thin films selenized and/or sulphurized at various temperatures were methodically examined in particular the influence of the annealing was conducted and studied at 450, 480, 500, and 550°C.

The ICDD files PDF No. 066-0163 (CZTSe), PDF No. 026-0575 (CZTS), and PDF No. 42-1120 were used to index the peaks (Mo). All of the films have peaks that correspond to the CZTS/Se phase and the Mo phase in the XRD pattern (from the substrate). In contrast to films selenized at 450°C, which only display peaks that correspond to the CZTSSe phase, films that were deposited revealed a wide peak at 28° and two Mo peaks at 40.3° and 73.6°. There are multiple peaks that correspond to secondary or ternary phases at temperatures of 480°C, 500°C, and 550°C. The phase-pure film generation at 450°C is confirmed by XRD. Films were sulphurized/selenized at 450°C to further investigate the impact of the annealing environment on the CZTS film. The XRD patterns of CZTS films annealed at 450°C for 30 min in atmospheres containing either selenium, sulfur, or sulfur+selenium are shown in Figure 56(b). There are no secondary or ternary phases identified, instead the layers exhibit XRD peaks that match to the CZTS/Se phase. Using Scherrer's formula, the crystallite size of the CZTS films was determined. For films that were annealed in the Se, S+Se, and S atmospheres, respectively, crystallite sizes were determined to be 14 nm, 21 nm, and 13 nm. The phases move to a lower angle for films annealed in a S+Se environment, but the peaks correspond to CZTS, confirming the addition of Se to the CZTS lattice. The (112) peak of the CZTS phase is more shifted to a lower angle in CZTS films that were selenized at 450°C [29]. Our CZTS/Se films underwent an extra study by Raman spectroscopy to further assess the phase purity in order to discover the potential secondary phases in our absorbers.

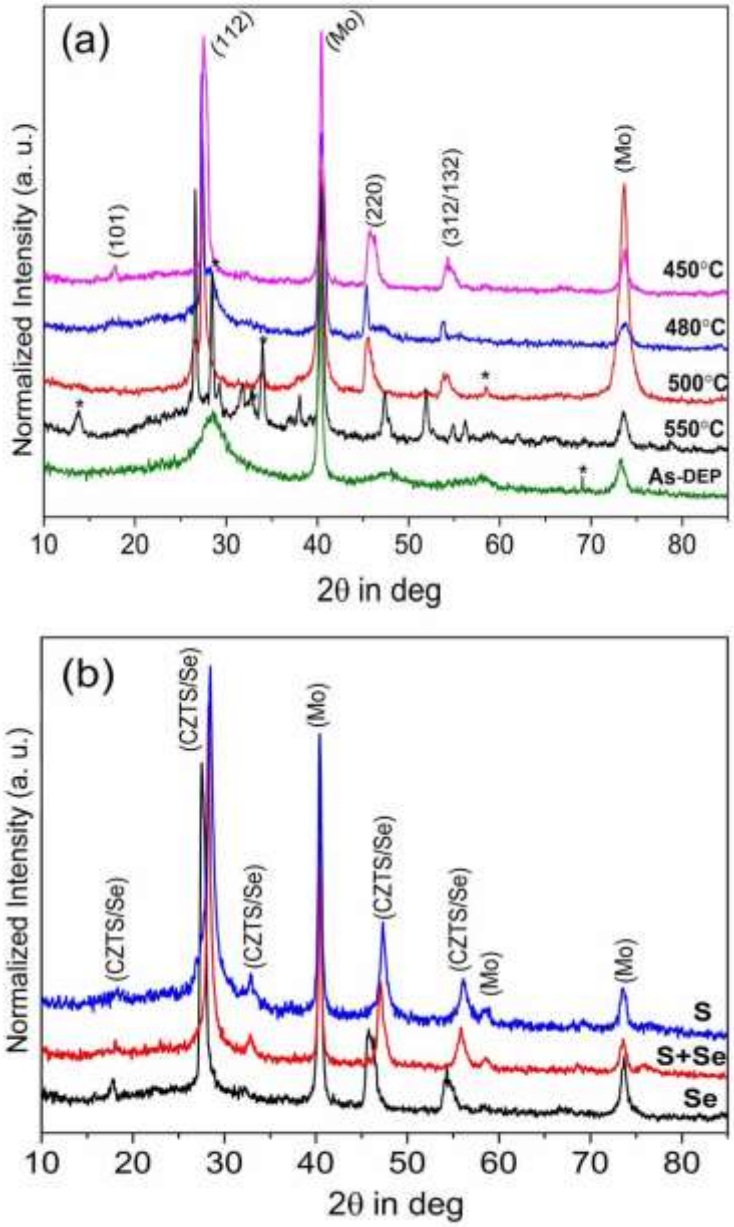

Figure 56. (a) CZTS thin film XRD pattern of selenization at various temperatures, (b) CZTS films annealed in various atmospheres at 450°C.

The Raman spectra of CZTS/Se films that were selenized and sulfurized at 450°C are shown in Figure 57. Observing the system, we assume to see binary and ternary secondary phases such as CuS(Se), ZnS(Se), SnS(Se), and CuSnS(Se) that, depending on the composition, may have negative impacts on the properties of the devices (these phases can be identified by the appearing of peaks shoulders nearby the characteristic peaks in the various characterizations). All of the films exhibit the distinctive CZTS

peaks at 332 cm^{-1}, 285 cm^{-1}, and 368 cm^{-1} in the Raman spectra. Along with these distinctive CZTS peaks, films sulfurized at 450°C exhibit Raman peaks at 235 cm^{-1} that are indicative of the Cu_2ZnS_3 phase.

The CZTSe phase is represented by the peak at 190 cm^{-1}, whereas the contribution of the peak at 219 cm^{-1} is uncertain because both the CZTSe phase and the SnS secondary phase do contain a peak at 219 cm^{-1}. Films selenized at 450°C additionally exhibit two additional peaks at 190 cm^{-1} and 219 cm^{-1}.

Films that were annealed in a sulphur + selenium environment in their Raman spectra seem to show no secondary phases, however, these are difficult to identify so we cannot entirely say that they are not present, we rather think that they are present but in small concentrations [29].

We perform AFM analysis of all the films annealed at different temperatures: the CZTSSe film's grain size and density increase as the selenization temperature rises, yet the average grain size is determined to be around 1 µm.

On the other hand, we have demonstrated above that only the films selenized at 450°C are devoid of secondary and ternary phases using XRD and Raman analyses.

Films annealed in S and S+Se atmospheres exhibit greater grain sizes and significantly better crystallinity as compared to those made in pure selenium atmospheres, as demonstrated in Figure 58 of a comparison of films annealed in various atmosphere compositions [29].

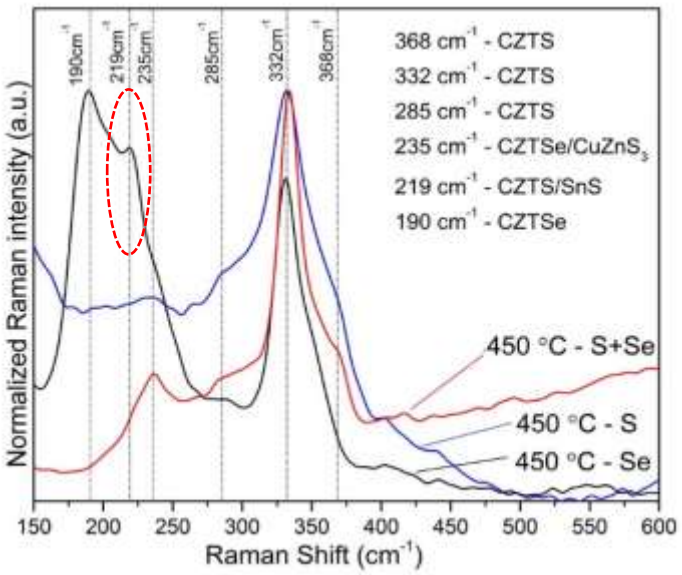

Figure 57. CZTS/Se films that were selenized and sulphurized at 450°C: Raman spectra.

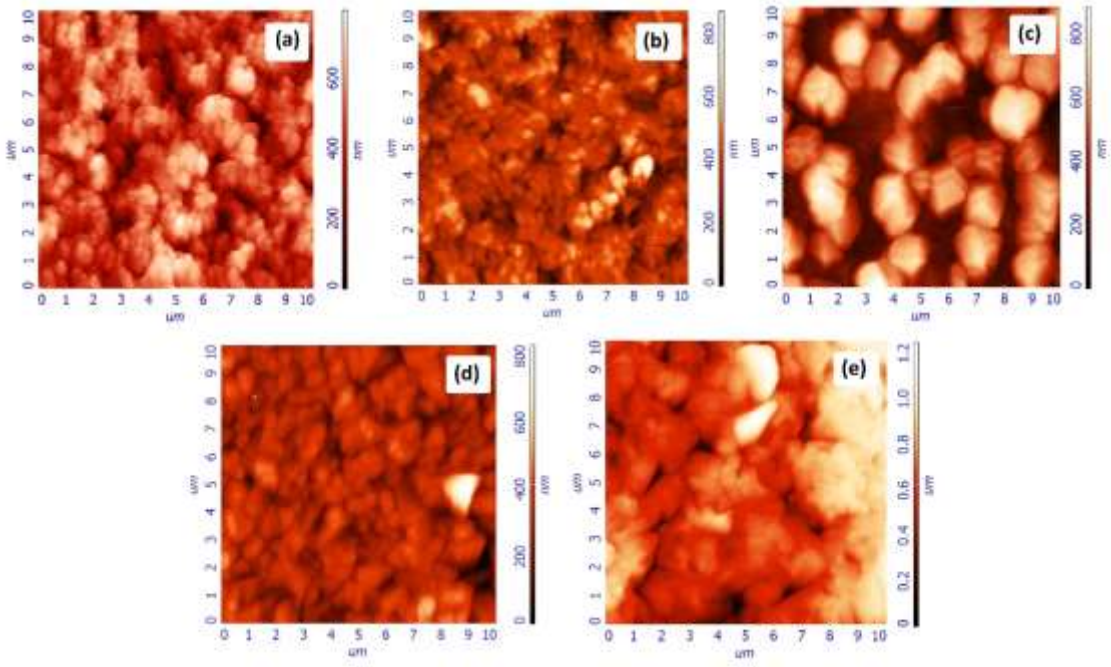

Figure 58. AFM pictures of (a) as deposited film (b) selenized at 450°C (c) 480°C (d) 500°C (e) 550°C CZTS films.

The films annealed in S and S+Se atmospheres exhibit greater grain size and significantly better crystallinity when compared to those made in pure selenium atmospheres, as demonstrated in figure below, which compares films annealed in various atmosphere compositions. The selenized film's decreased crystallinity and smaller grain size may be very likely the result of sulphur being lost during annealing.

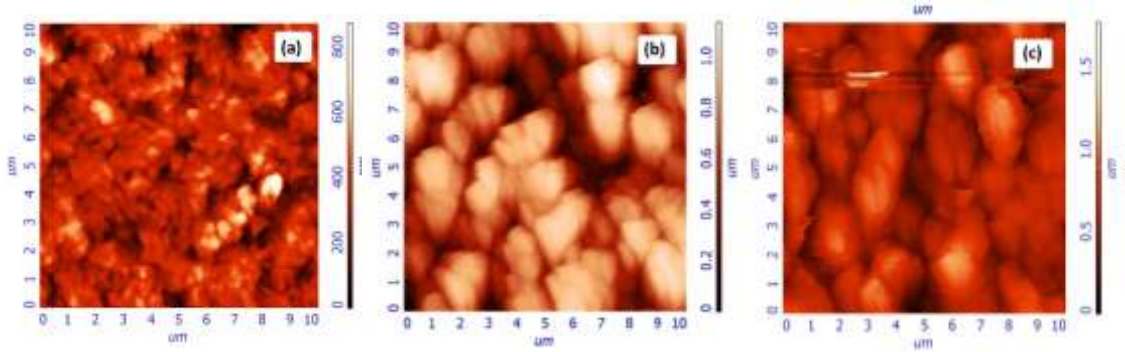

Figure 59. AFM pictures of the CZTS thin films annealed at 450°C in the atmospheres of (a) Se (b) S, and (c) S+Se.

Devices with the aforementioned selenization atmosphere were made, and the solar cell performances of those devices were examined.

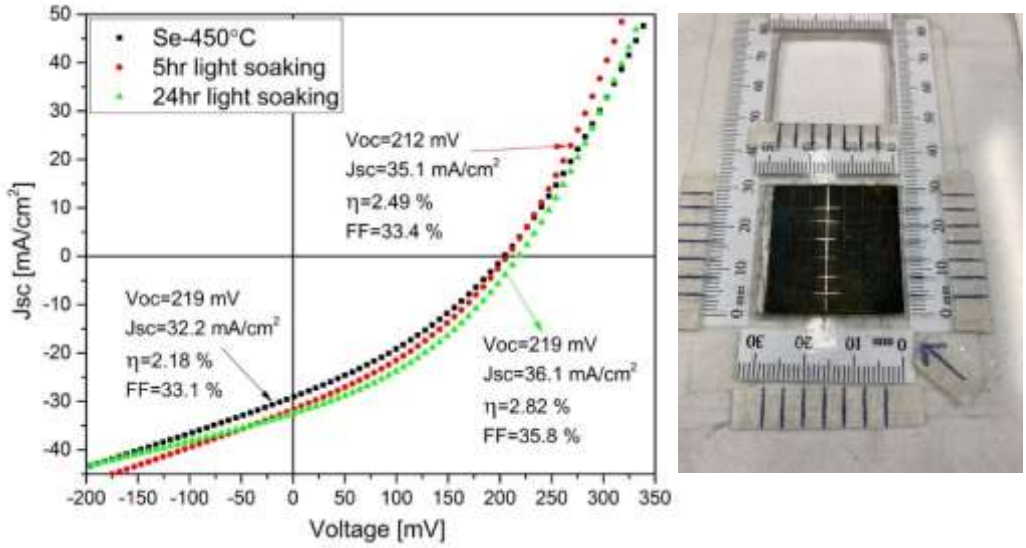

Figure 60. JV features of the CZTS solar cell.

The JV properties of the CZTSSe solar cell are displayed in Figure 60. Device parameters displayed by prototype CZTSSe films include Voc=212 mV, Jsc=35.1 mA/cm^2, FF=33.4%, and efficiency of 2.2%. The finished cells were also subjected to light soaking treatment. The best device was treated for 5 hours and 24 hours under standard light soaking conditions (1 sun illumination), and the results are shown in Figure 60. Light soaking increases device performance, reaching an efficiency of 2.8% with a significant improvement in the J_{sc} after the first 5 hours and the fill factor after 24 hours [29].

5.3 Analysis of selenization temperature

After these initial results and after improving the reproducibility of the devices, we focused our research on the annealing step in selenium atmosphere.

The above-mentioned selenization method is followed by the spin coating approach for depositing CZTS precursors. A 30-minute selenization at different temperatures (450°C, 500°C, and 550°C) was conducted to examine more in detail the effects of selenization temperature. All the devices were completed as already described.

The polycrystalline tetragonal chalcopyrite crystal structure of CZTS thin films selenized at different temperatures (CZ450 at 450°C, CZ500 at 500°C, and CZ550 at 550°C) exhibits a dominating peak along (112) reflection plane (Figure 61). The diffractogram reveals again the presence of (101), (110), (103), (121), (220), and (132) distinctive diffraction peaks, which indicate the development of a CZTSSe material with an ordered cation sublattice (ICDD PDF # 01-082-9159). The S/Se ratio may be anticipated to be 0.25 by comparing the location of the (112) plane with the common ICSD pattern file, suggesting that the film is Se rich.

The computed lattice parameters and crystallite sizes for the films are as follows for films selenized at 450°C, 500°C, and 550°C, respectively, a=b=5.6515 Å, c=11.3143 Å, 30 nm, a=b=5.6439 Å, c=11.3339 Å, 36 nm, and a=b=5.6515 Å, c=11. A small increase in the size of the crystallites is shown by raising the selenization temperature. All films have peaks ascribed to Mo, particularly the (110) orientation, in addition to the CZTSSe phase. More intriguingly, for the 500°C-case, the secondary phase of $SnSe_2$ is responsible for a peak that appears at roughly 31°. Instead, the secondary phase is minimized when selenization is carried out at 550°C.

The position of (112) peak in the three XRD patterns is consistent with the rise and fall of this peak caused by increasing selenization temperature. In fact, a shift in the (112) peak can be seen as shown in Figure 62. Typically, pure CZTSe shows a peak at 27.16°; however, when sulphur begins to replace Se, the peak shifts to higher values, reaching a two theta of 28.44 °, which corresponds to pure CZTS.

In comparison to the 450 °C- and 550 °C-cases, the strata are therefore richer in Se as the blue peak (500°C) moves to the left of the graph at lower wavenumbers (red and black peaks).

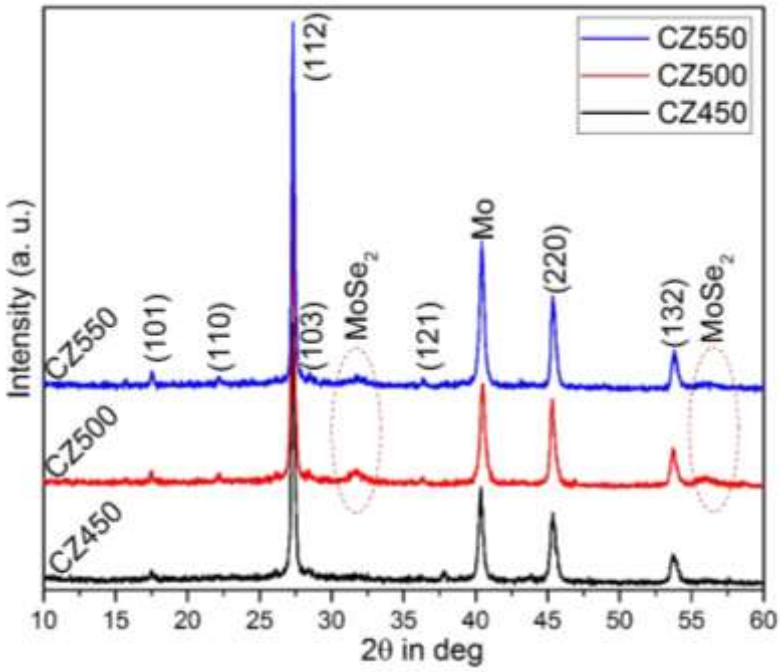

Figure 61. CZTSSe films selenized at various temperatures, as shown in the XRD pattern.

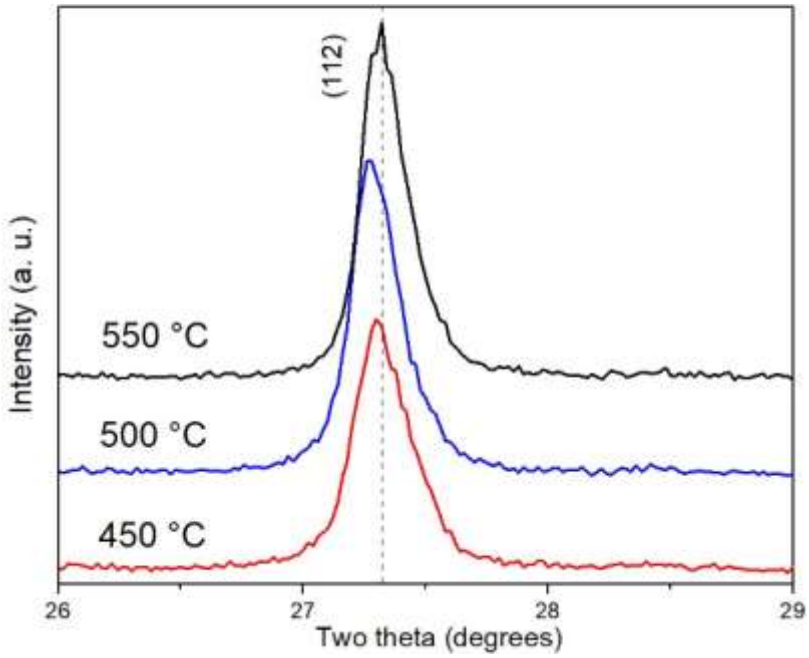

Figure 62. XRD pattern of CZTSSe films selenized at various temperatures, in the 26° to 29° range pure CZTSe shows a peak at 27.16°; when sulphur begins to replace Se, the peak shifts to higher values.

The Raman spectra of the films that were selenized at various temperatures are shown in Figure 63. The typical CZTSSe peaks can be seen in all films at 56 cm^{-1}, 80–82cm^{-1}, 174–177 cm^{-1}, 196–198 cm^{-1}, 235–250 cm^{-1}, and 329–332 cm^{-1}, which correspond to the E–A–A–B–A vibrational modes of the CZTSSe phase, respectively. Comparing the three spectra reveals a shift in the peaks in this instance as well. Similar to the XRD, the rise in sulfur relative to selenium is caused by the shift towards higher wavenumbers in Raman.

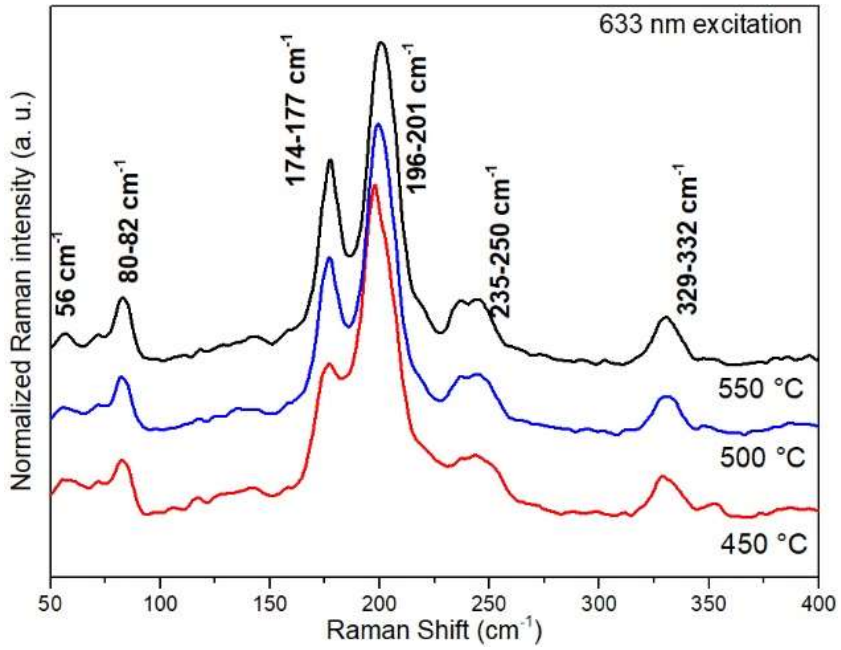

Figure 63. Raman spectra of CZTSSe selenized at various temperatures at 633 nm laser illumination; it is evident as in the XRD analysis the shift towards higher wavenumbers.

By enlarging the spectra in the 180 cm^{-1} - 225 cm^{-1} region in Figure 64, we emphasize the shift of the 196-198 cm^{-1} peak. In this instance, when temperature rises, the peak's rightward shift is more pronounced. The unusual behavior, compared to XRD, can be explained by the fact that the Raman is strongly surface sensitive. Hence, the shifts show less Se at the CZTSSe surface, proving that the more Se that is lost on the top of the absorber, where CdS is formed, the higher the annealing temperature.

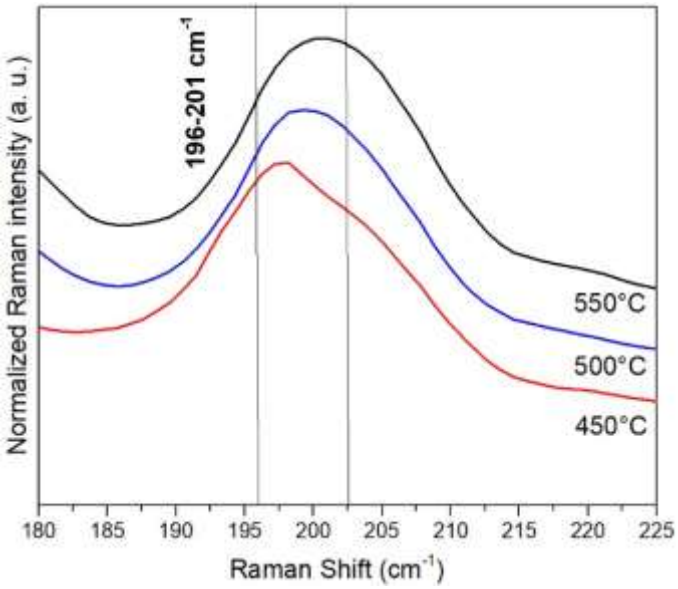

Figure 64. Raman spectra at 633 nm laser illumination in the 180 cm^{-1} to 225 cm^{-1} range.

The performance of the completed devices was evaluated after the absorbers were selenized at various temperatures. The JV curves of three typical solar cells with CZTSSe absorber layers that were selenized at 450°C, 500°C, and 550°C are shown in Figure 65.

The efficiency of the devices is enhanced by raising the selenization temperature, mostly due to an increase in J_{sc}. On the other hand, the V_{oc} exhibits its greatest value at 500°C and is somewhat lower at the other temperatures, while the FF steadily drops.

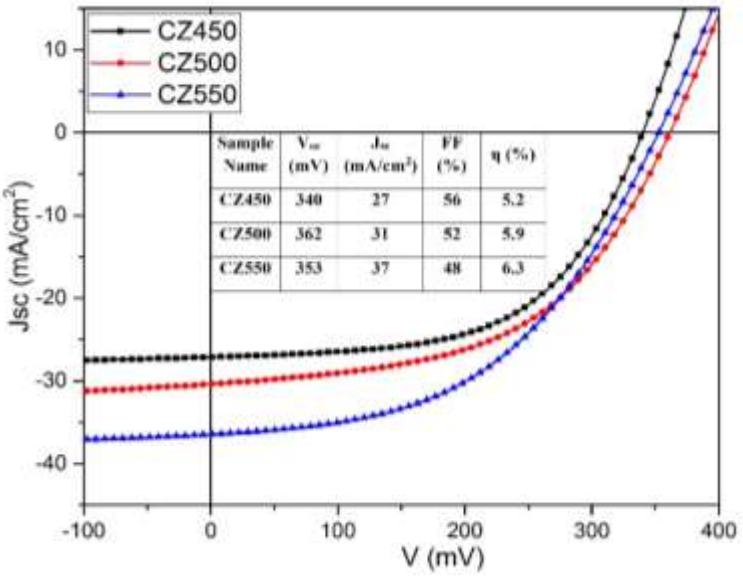

Sample Name	V_{oc} (mV)	J_{sc} (mA/cm²)	FF (%)	η (%)
CZ450	340	27	56	5.2
CZ500	362	31	52	5.9
CZ550	353	37	48	6.3

Figure 65. JV characteristics of CZTSSe devices fabricated.

5.4 Doping effects on the cell performances

When semiconductor materials from group IV are doped with group V atoms, *n-type* material is produced. When semiconductor materials from group IV are doped with group III atoms, *p-type* materials are produced.

P-type materials enhance conductivity by increasing the number of holes present, whereas n-type materials increase the conductivity by increasing the number of electrons in a semiconductor [75].

It became evident from the various combinatorial investigations carried out since the ground-breaking study of Katagiri in 2005 [76] that it was not feasible to further improve the device performance by just modifying the absorber stoichiometry. In order to improve the electrical characteristics of kesterite absorbers, the addition of extrinsic materials to the kesterite matrix in varying proportions has become a hot issue. This strategy has also been influenced by related CIGS and CdTe technologies, where bandgap engineering by substitutional doping (alloying) was paired with the use of extrinsic species to passivate intrinsic defects and give shallow dopants to improve the solar cell efficiencies to 22%.

In contrast, alloying refers to the introduction of ionic size mismatch by an isoelectronic cation substitution, which might be especially interesting for band engineering of the absorber.

Most of the published works employ vacuum deposition methods, and doping is accomplished in two ways: either by providing the dopant during deposition or by applying treatments after deposition. As an alternative, in this study we describe an unique and significantly less complicated method that involves drop casting a solution containing an impurity element onto a CZTSSe film, followed by annealing in a selenium environment. Alkali elements (such as Na, and K), as well as metals like Ge, have been already introduced in solution processed CZTSSe solar cells [25], [77], [78]. In specifically, we employ chlorine as an impurity conveyor.

We examine and discusses the effects of the procedure with Na, K, and Ge inclusion on the mechanical and electrical characteristics of the CZTSSe absorber.

5.4.1 Effect of alkali metals and Germanium doping

The devices have been fabricated as mentioned above. The newly developed inclusion procedure is based on chloride compounds' capacity to function as effective conveyors. We specifically selected germanium chloride ($GeCl_4$), potassium chloride (KCl), or sodium chloride (NaCl) to be dissolved in methanol and placed on the absorber surface. The sample is then placed on a hot plate and heated to 150°C for 3 minutes before being rinsed with distilled water. This solution is then drop-casted onto the CZTS film. On the samples doped with germanium an additional washing with distilled water was tested (samples named with CZ-Ge and CZ-Ge without washing). An extra test with drop casting of a chlorine solution has been performed, but it will not be mentioned because is patent pending.

It is important to identify if the impurities are formed as secondary phases, integrated into the crystal structure of the crystal, separated in the grain boundaries, or are altering the crystal structure of the absorber. For this reason, we have used XRD and Raman analyses to analyze and contrast CZTS absorbers that had been impurity-treated and those that were not. According to ICDD file number 01-082-9159, which specifically refers to a specific kesterite structure called the $Cu_2ZnSn\,(S_{0.2}\,Se_{0.8})_4$ phase, the XRD patterns of treated and untreated Mo/CZTSSe films display the characteristic peaks for CZTSSe compound, indicating that Se is incorporated in the compound with an excess of Se over S. A further reflection at 31.6 degrees is seen in Ge-treated films, and it can be attributed to either the SnSe [79] phase or the GeSe [80] phase. This was identified by Neuschitzer et al. as the SnSe phase in the Ge-treated CZTSe; they showed that the strength of the SnSe peak increased with the Ge concentration. This describes how Ge is absorbed into the matrix by replacing Sn, and how the extra Sn combines with Se to generate a secondary phase called SnSe [81].

The (112) peak of the treated samples exhibits a little shift, therefore we emphasized the shift by enlarging the pattern in the 2 range between 26.8 and 28° (Figure 66 (b)). Typically, the peak of pure CZTSe is located at 27.16°; however, when sulphur replaces Se, the peak changes to higher 2 values, eventually reaching 28.44°, which is the peak of pure CZTS [66].

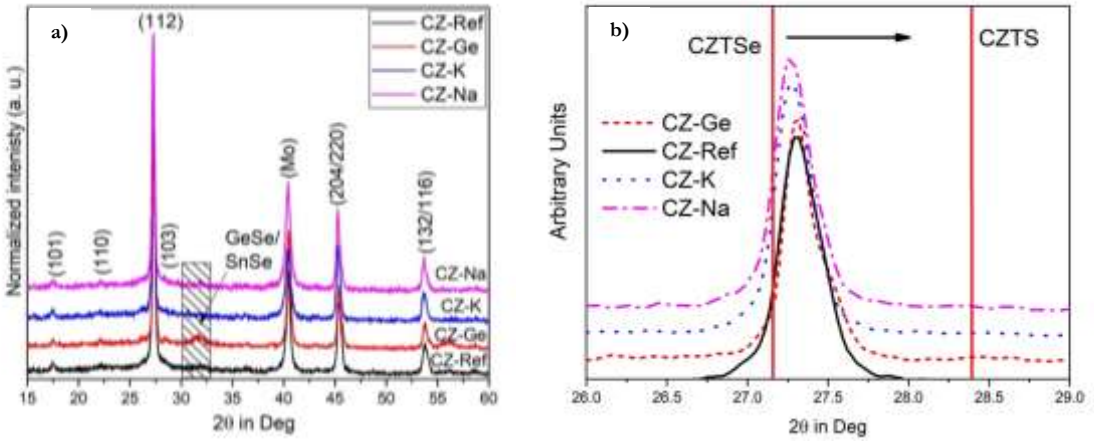

Figure 66. (a) Untreated and treated samples' XRD patterns, (b) XRD pattern of untreated and treated samples in the 26.8-28 2θ-range.

In our example, the (112) peak is displaced away from the direction that is Se-rich, indicating that Se is a common element in the absorber. In the lines that follow, we'll talk more about this. The lattice parameter (derived from the tetragonal structure) for the untreated absorber matches the standard values obtained from the ICDD data accurately (see Table I). The lattice parameters instead rise from the conventional values when impurities are added, with a minimum increase for the Ge case and a maximum for the K case. Since each of these elements effectively occupies the Sn position and has an atomic radius of 125 pm, 190 pm, and 243 pm, respectively we may infer that they are all present in the lattice structure [79], [80], [82].

We considered the (112) and (204/220) planes when calculating the average crystallite size, and the results are shown in Table 3.

Table 3. Structure of the CZTSSe absorber material after treatment and without treatment.

Sample	Crystallite size (nm)	Lattice parameters (Å)		Strain S	Texture coefficient (TC(112))
		a=b	c		
CZ-Ref	28	5.649	11.285	0.0012	0.696
CZ-Ge	40	5.655	11.302	0.0009	0.613
CZ-Na	34	5.661	11.324	0.001	0.794
CZ-K	32	5.662	11.327	0.0011	0.695
(ICDD:01-082-9159)		5.642	11.250		

Figure 67 displays the Raman spectra of CZ-Ref, CZ-Ge, CZ-K, and CZ-Na films produced at 633 nm and 532 nm laser excitation wavelengths. All of the films have the distinctive CZTSSe peaks at 56 cm^{-1}, 80 cm^{-1}, 174 cm^{-1}, 196 cm^{-1}, 235 cm^{-1}, and 329 cm^{-1}, which correspond to the E, A, A, B, and A vibrational modes of the CZTSSe phase, respectively. A secondary phase at 215 cm^{-1}, which corresponds to the GeSe, is only seen in the CZ-Ge case [32], supporting the theory from the XRD study that Ge and Se are combining to produce a secondary phase. With a lower shift for CZ-Na and a bigger shift for CZ-Ge, the treated absorbers' CZTSSe peaks are displaced to higher wavenumbers. This demonstrates that a greater S/Se ratio is seen with Ge inclusion, indicating a lower selenium content [81].

The same reflections are confirmed by Raman spectra that were run at 633 nm laser excitation wavelength [37]. Additionally, as you will see in Figure 68, an obvious shift in the Ge-treated CZTSSe is verified, once again confirming a lower quantity of Se. The changes in the XRD and Raman graphs, as well as the extra GeSe peak in the XRD, indicate that Ge combines with Se to generate GeSe, which in turn restricts the Se diffusion in the lattice during the selenization process.

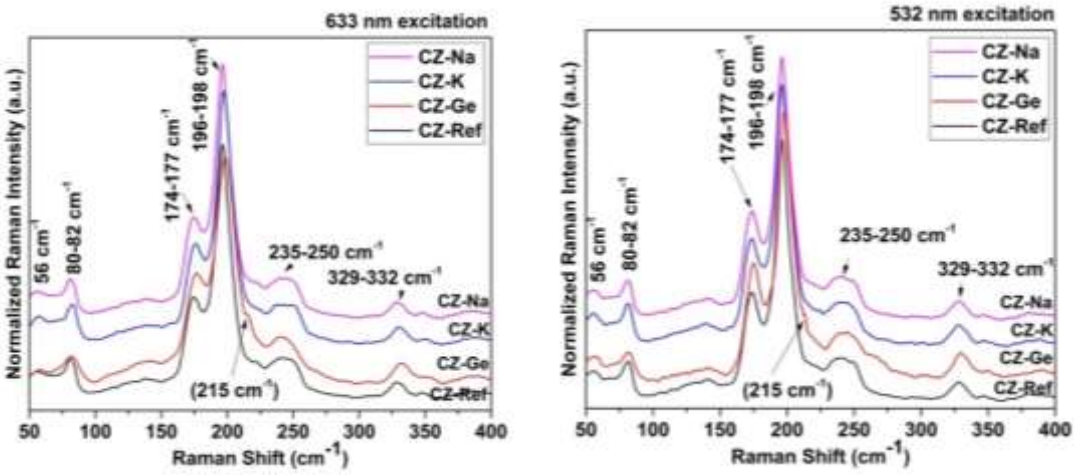

Figure 67. Raman spectra of untreated and treated materials excited by lasers at 633 nm and 532 nm: these spectra confirm for the treated absorbers a shift of the CZTSSe peaks with a larger shift for CZ-Ge and a smaller shift for CZ-Na (see figures 68 and 69).

By altering the crystallite size and the lattice route, contaminants become a component of the crystal lattice.

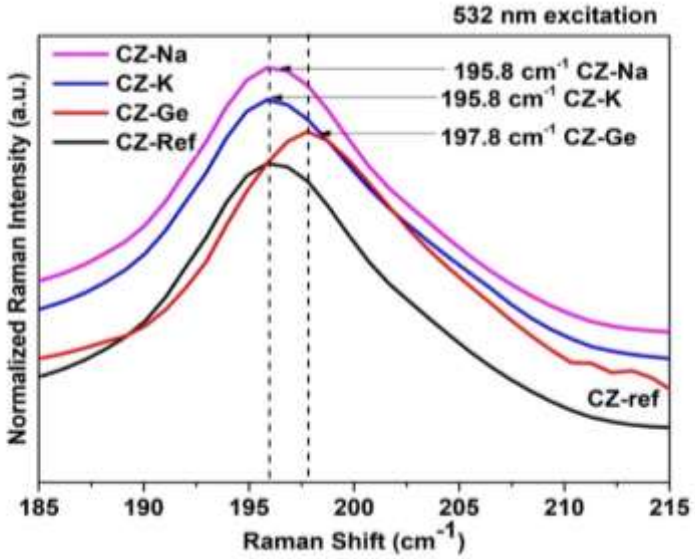

Figure 68. Raman spectra in the 185-215 cm^{-1} range under 532 nm laser illumination.

Only Ge alters the S/Se ratio and the compound's stoichiometry by interacting with Se to generate an extra secondary phase, whereas only Na marginally changes the crystal structure of the film by strengthening the (112) preferred orientation [81].

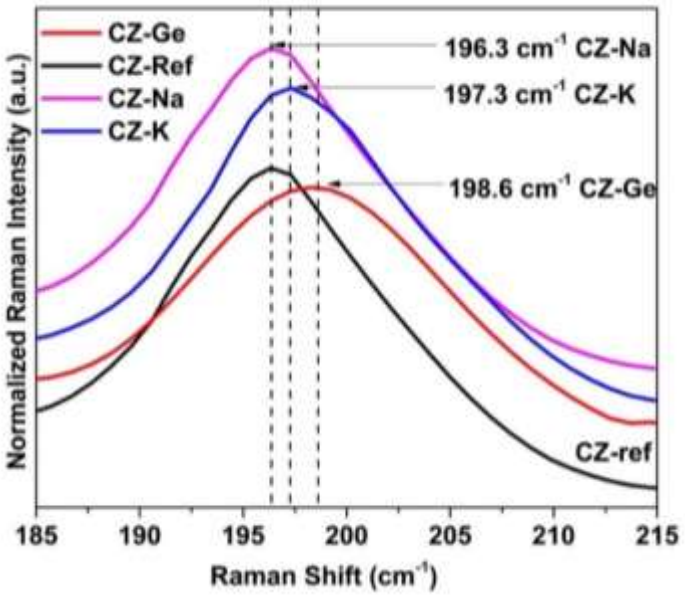

Figure 69. Raman spectra in the 185-215 cm^{-1} range under 633 nm laser illumination.

Figure 70 of the samples' SEM examination displays images of the giant grains comprised of clusters of little grains (which have been observed by AFM). With somewhat greater compactness for Na-incorporated absorber, the big clusters are identical in all instances. There are many dark grey contrasts in the Ge-CZTSSe samples [81].

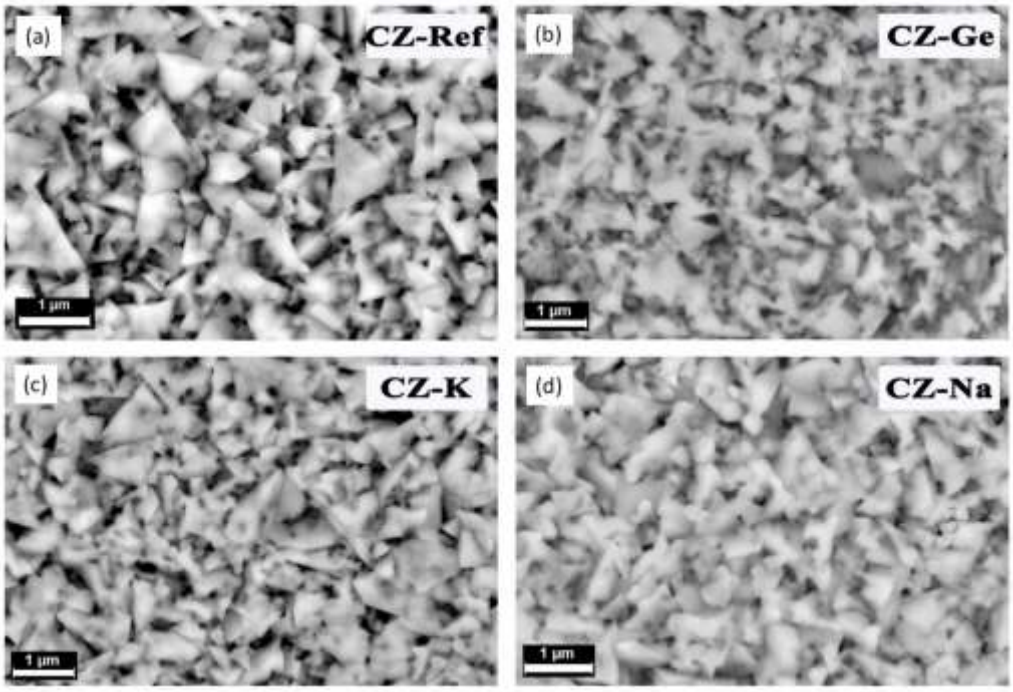

Figure 70. SEM examination of reference and experimentally modified CZTSSe absorbers: (a) CZTS sample undoped, (b) sample treated with germanium, (c) sample treated with potassium, (d) sample doped with sodium.

The EDXS analysis performed in conjunction with the SEM analysis (see Table 4) is more intriguing because it reveals that the impurity concentration for Na and K is very low and below the detectable level. Since the structural analysis attests to the incorporation of these into the matrix, we can conclude that this process only incorporates a very small quantity of impurities based on the drop casting of the chlorine compounds. To confirm that the treatment method has an impact on stoichiometry, it is determined for these situations that the Cu/Zn+Sn concentration is somewhat different from the reference value. Because K and Na are undetectable on the surface, KCl and NaCl are very soluble in water. As seen in the Raman and XRD analyses, the samples with Ge inclusion demonstrate a different stoichiometry; the impurity is found at a lower selenium content. When we eliminate the surface

cleaning step from the impurity inclusion procedure (by rinsing the absorber after the annealing at 150°C), the O presence increases more than the Ge presence does (indicated in the table as CZ-Ge without washing). This is explained by an increased oxidation of extra Ge [81].

Table 4. Data from the EDXS analysis of untreated and treated samples.

Element	CZ-Ref (at %)	CZ-K (at %)	CZ-Na (at %)	CZ-Ge (at %)	CZ-Ge without washing (at%)
Cu	24.57	25.45	25.96	24.96	20.08
Zn	14.47	13.6	13.36	13.47	12.12
Sn	12.58	12.88	12.94	13.1	9.95
S	7.02	7.82	6.56	6.87	8.69
Se	41.35	40.25	41.18	39.76	32.88
Impurity	0	0	0	1.11	8.48
O	0	0	0	0.76	7.79
Cu/Zn+Sn	0.91	0.96	0.99	0.94	0.91
Zn/Sn	1.15	1.06	1.03	1.03	1.22
S/Se	0.17	0.19	0.16	0.17	0.26

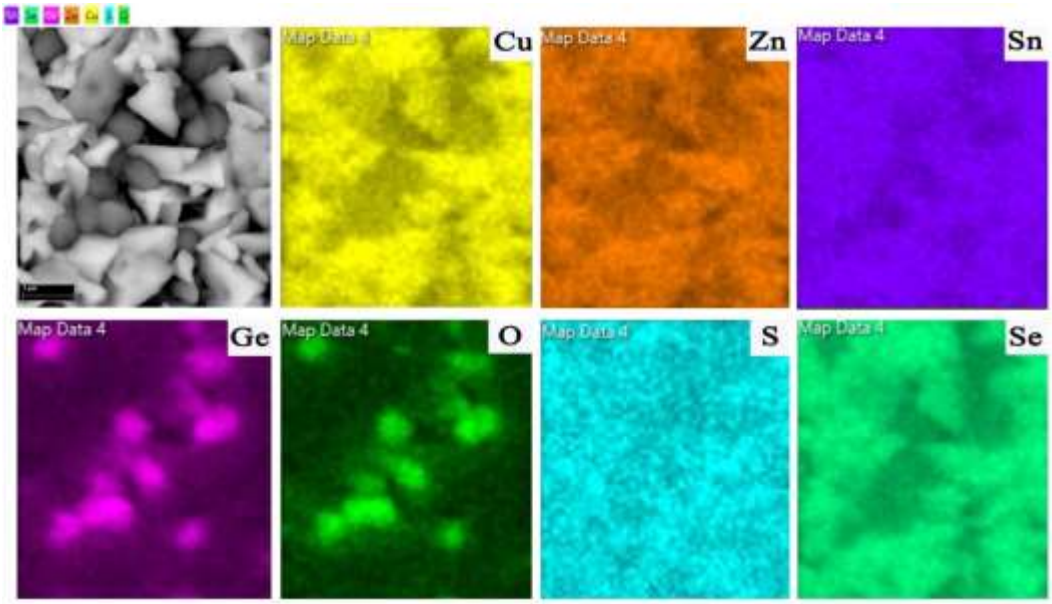

Figure 71. Ge-incorporated CZTSSe EDX analysis.

The addition of K, Na, and Ge impurities alters the structure, stoichiometry, and some of the physical characteristics of the CZTSSe absorber. This shows that the suggested method of using chlorine compounds is effective in introducing impurities into the matrix and particularly effective in the case of germanium [81].

As shown in figure below (Figure 72), the performances of the final devices treated with various solutions have been studied and contrasted with the benchmark devices manufactured using absorbers that have not been treated (CZ-Ref).

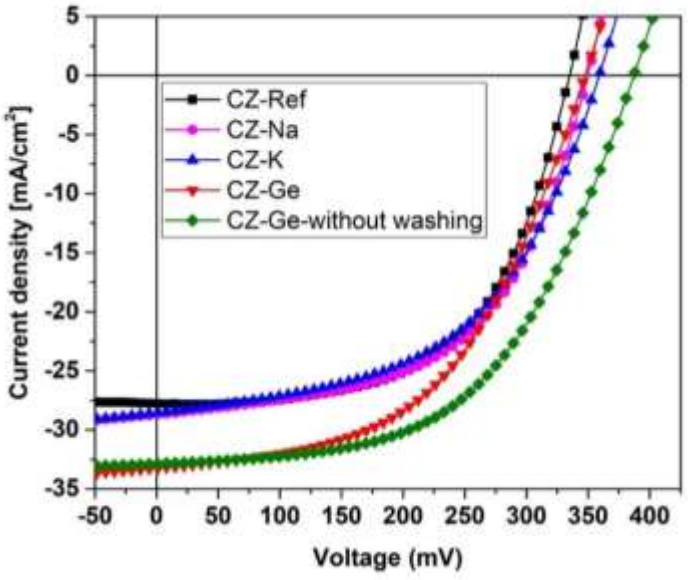

Figure 72. JV properties of treated and untreated CZTSSe-based devices.

The largest conversion efficiency for reference devices is 5.42% (V_{oc}=334 mV, J_{sc}=28 mA/cm^2, and FF=58%). The open circuit voltage, which should be in the 600 mV range, is the key factor limiting this rather low efficiency. If we take into account that this process is not only non-vacuum hydrazine-free but also carried out at temperatures below 450°C and with only one selenization step, the efficiency is only moderately poor. The introduction of certain contaminants improves conversion performance, as was predicted in the initial section of the paper. For Na, K, and Ge inclusion, the top cells performed at 5.43%, 5.60%, and 5.87%, respectively. The improvement is specifically linked to the rise in both V_{oc} and J_{sc} (see Table 5).

We have also examined Ge-included samples where the treatment method has been changed by omitting the surface cleaning after drop casting and heating, as indicated in the EDXS section. This has advantages and disadvantages: it raises the quantity of

integrated Ge while increasing the process's irreproducibility, potentially leading to faults at the CZTSSe/CdS interface. However, with this adjustment, the efficiency increases to 7.1%, with a 20% improvement in V_{oc}, suggesting that $GeCl_4$ is a feasible technique for enhancing efficiency by lowering defect density.

Table 5. The performance metrics of the best treated and untreated CZTSSe samples.

Sample	V_{oc} (mV)	J_{sc} (mA/cm^2)	FF (%)	η (%)	Rs (Ω)	Rsh (Ω)
CZ-Ref	334	28	58	5.42	17	2990
CZ-Ge	349	33	51	5.87	23	884
CZ-Ge- without washing	**390**	**33**	**55**	**7.1**	**25**	**1797**
CZ-Na	360	29	52	5.43	18	733
CZ-K	351	29	55	5.60	23	645
AST-CZ-Ref	339	31	55	5.78	17	999
AST-CZ-Ge	362	32	52	6.02	21	670
AST-CZ-Ge- without washing	390	32	54	6.74	24	1264
AST-CZ-Na	352	30	55	5.81	18	697
AST-CZ-K	352	30	52	5.49	22	551

For this study we have also performed External Quantum Efficiency (EQE) analysis, recorded using a SpeQuest quantum efficiency system. This parameter often used as performance indicator as it provides the ratio of photons extracted over the charges injected. In our case all the curves in the graph seems to show the same response that decreases with increasing wavelength. What could happen in this case is that all the carriers generated especially those with higher λ are not collected: if defects are present

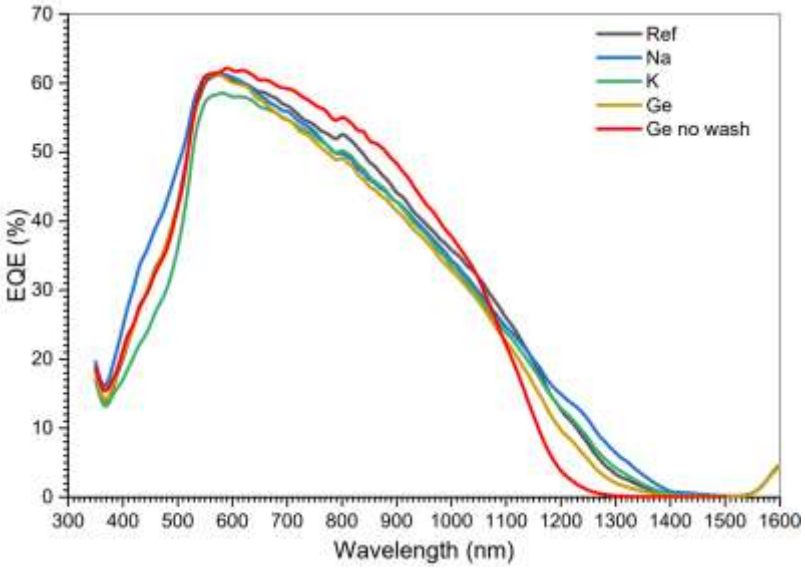

Figure 73. Comparison of EQE samples with different doping elements.

in areas far from the p-n junction it happens that carriers disperse. In particular in the samples doped by germanium without the washing procedure in distilled water we think there is less recombination or less collection: the band gap seems to be changed and to be higher.

The stability and behavior of the final devices were investigated using an accelerated stability test (AST) in a metal box at 80°C and one solar light. This is a valuable technique for determining device stability, but it may also aid in identifying the nature of problems through the interpretation of degradation behavior, as explained below.
There is a modest improvement in efficiency after 24 hours of AST for CZ-ref, CZ-Na, and CZ-Ge samples. Non-washed Ge-CZTSSe absorber also has a minor reduction in efficiency after AST. This might imply that light soaking is passivating some defects that were not present in the unwashed Ge sample.
Despite a significant rise in V_{oc} and J_{sc}, the fill factor decreases when impurities are added. This might be due to a variety of factors, including a probable decline in

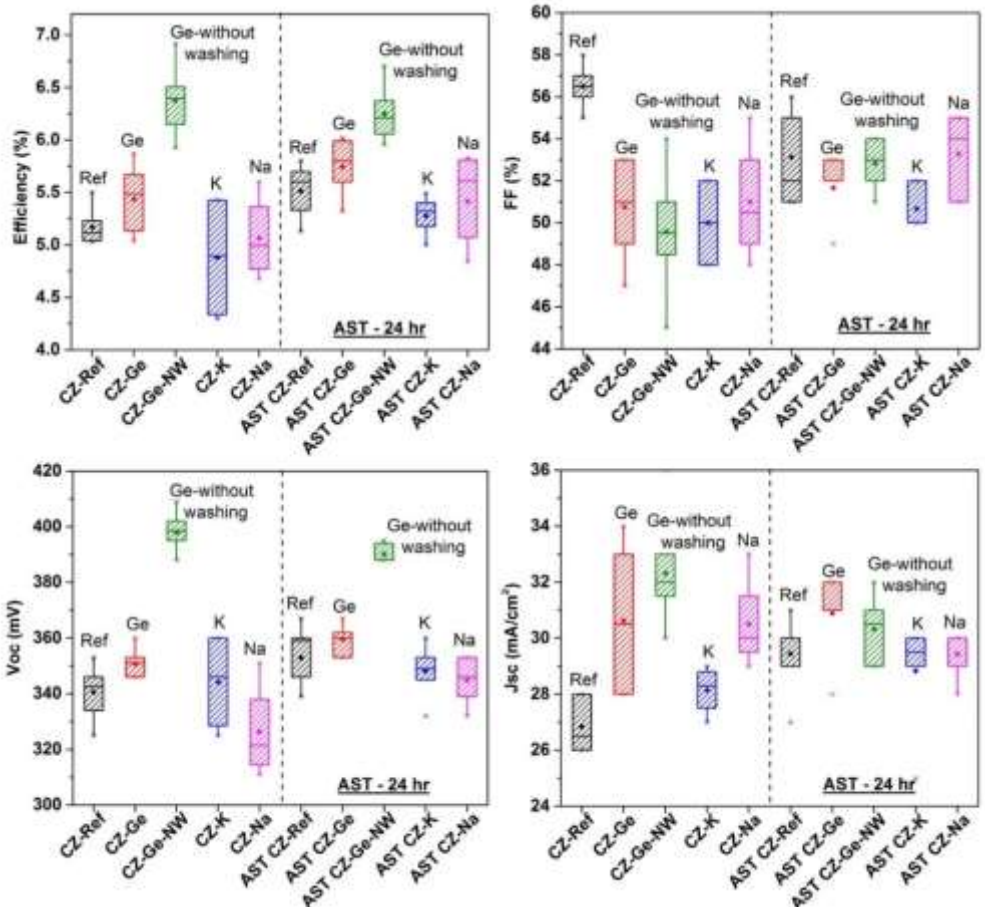

Figure 74. Before and after AST statistical box plot of JV features in untreated and treated samples.

junction quality or the existence of various defects caused by the change in carrier density [81].

We then investigated the device's carrier concentration and defect density using capacitance-voltage methods, as detailed in Chapter III. Figure 75 depicts the net charge density profiles of acceptor minus donor states retrieved from CV and DLCP measurements of Ge- and K-treated and untreated CZTSSe-based solar cells as a function of distance from the junction.

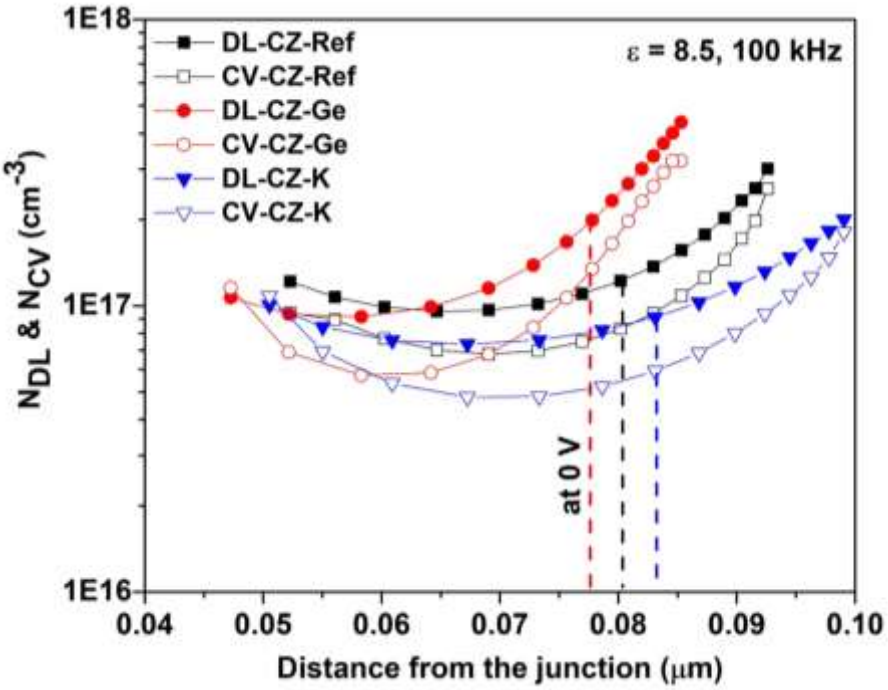

Figure 75. Profiles of CV-DLCP in untreated and treated samples.

Table 6. At 0 DC bias voltage, CV-DLCP analysis of untreated and treated devices was performed.

Sample	N_{CV} (cm^{-3})	N_{DL} (cm^{-3})	N_{IT} (cm^{-3})	χ_d (nm)
CZ-Ref	8.3×10^{16}	1.2×10^{17}	3.7×10^{16}	80.2
CZ-Ge	1.3×10^{17}	2.0×10^{17}	7×10^{16}	77.6
CZ-K	6.0×10^{16}	9.1×10^{16}	3.1×10^{16}	83.2

Table 6 shows the carrier density extracted by CV measurements (open dots) and the carrier density derived by DLCP measurements (closed dots) (full dots). Imperfections at the interface and in the bulk impact CV readings, but DLCP is less subject to interface defects. The carrier concentration indicated by DLCP (NDL) for the reference sample is about $1.2 \cdot 10^{17}$ cm^{-1}, the density of deep interface defects is $3.7 \cdot 10^{16}$ cm^{-1}, and the depletion width (at zero bias) is 80 nm. Surprisingly, the CV curves for all devices are lower than the DLCP curves, indicating that there are compensatory flaws at the interface that diminish the overall number of effective defects discovered by CV. The low fill factor obtained for the treated samples supports the idea of compensating defects at the interface. The DLCP defects density for Ge-treated samples is larger than the densities retrieved for CZ-ref and CZ-K, indicating a higher carrier concentration, which is further corroborated by a lower depletion width of 77.6 nm. Furthermore, the CV value is larger, which means that, in addition to the increased defect states that improve device performance in terms of V_{oc} and J_{sc}, the number of compensating defects at the interface is reduced. Interestingly, after treatment with alkali elements, the defect concentration is decreased, most likely due to the creation of compensating defects.

5.5 Study and synthesis of a new window layer: TiO_2

Because of its significant potential in pollution treatment and self-cleaning qualities, the synthesis and optimization of TiO_2 thin films is a rapidly expanding area in the field of environmental engineering. Transparent glass offers a wide range of applications. It is commonly applied in our houses (in windows, doors, and shower enclosures), automotive windshields, electronic device displays, and new skyscraper building materials. Keeping the surface of the glass clean is a difficult chore; because of its optical transparency, all dirt particles, stains, and fingerprints on the surface are visible. Covering the surface of buildings with a thin layer of TiO_2 can replace external glass cleaning and save money (along with water and chemicals). When exposed to light with an energy content equivalent to or greater than the band gap of TiO_2, it exhibits photocatalytic and hydrophilic capabilities. It is critical however to discover a cost-effective and efficient thin film deposition process for commercial application. Chemical vapor deposition [4], sputtering, hydrothermal, electrophoretic, sol-gel, and spray pyrolysis have all been used to produce TiO_2 films [83].

In this study having selected the precursor solution, to develop a new transparent window layer, changes were made to the precursor solution and the deposition method in the current investigation.

By basing on previous works [84], [85], spin-coating was used to fabricate TiO_2 window layer. With stirring at room temperature, two titanium-isopropoxide solutions in ethanol were prepared at concentrations of 0.15 and 0.3 M. These were spun progressively at 3000 r/min onto the TEC10 substrate, with each layer drying for 10 minutes at 120°C. The finished substrate was then sintered in air for 30 minutes at 450°C. Initially, we kept the solution concentrations comparable to the articles mentioned above, 0.15 and 0.3M by testing on two different supports: glass and TEC. However, we have also worked with higher concentrations.

In terms of deposition techniques, spin coating was applied also for 10 seconds at a speed of 2000 rpm, depositing 200 µl of solution.

During the first synthesis of the precursor solution, it was observed that after a certain amount of stirring time at room temperature (around 6 minutes of stirring), the solution became turbid; this phenomenon could coincide with the compound's instability, with subsequent precipitation of TiO_2 (which is typically white) in solution. The maximum stirring time was then established at 2 minutes. We then decided to employe also acetylacetone (AcacH) used as a stabilizing agent. The interaction of TTIP (titanium isopropoxide) with AcacH has been extensively researched in the literature. Acetylacetone acts as a nucleophilic reactant, replacing the alkoxy group and forming a new molecular precursor.

Figure 76. Samples of TiO_2 solution at different stirring times.

A comparison was made between samples with different solvents (ethanol and IPA) at the same concentration, between 1 and 2 layers of TiO_2, with the deposition rate varying. It is worth noting that speed influences transmittance, most likely because less material is deposited on the support, improving its transparency. However, the solvent isopropanol gave better results in terms of transmittance.

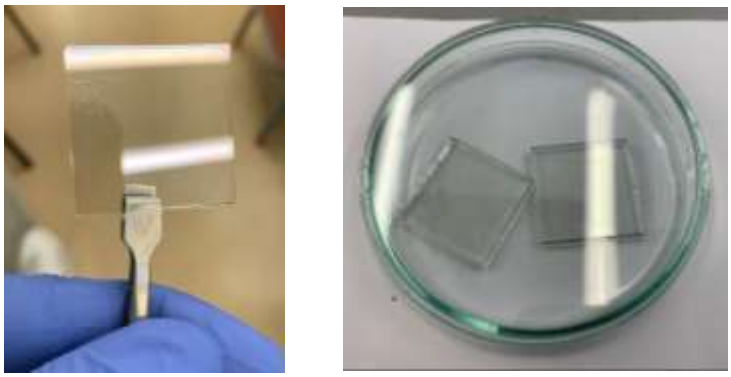

Figure 77. Samples of deposited TiO_2 film.

The crystallinity, phase composition, and mean crystallite size of TiO_2 thin film were investigated using X-ray diffraction (XRD). The reflection planes from (101), (103), (004), (112), (200), (105), and (211), respectively, correspond to the diffraction peaks at 2 theta of 25.3°, 37.0°, 37.8°, 38.6°, 48.1°, 53.9°, and 55° [83].

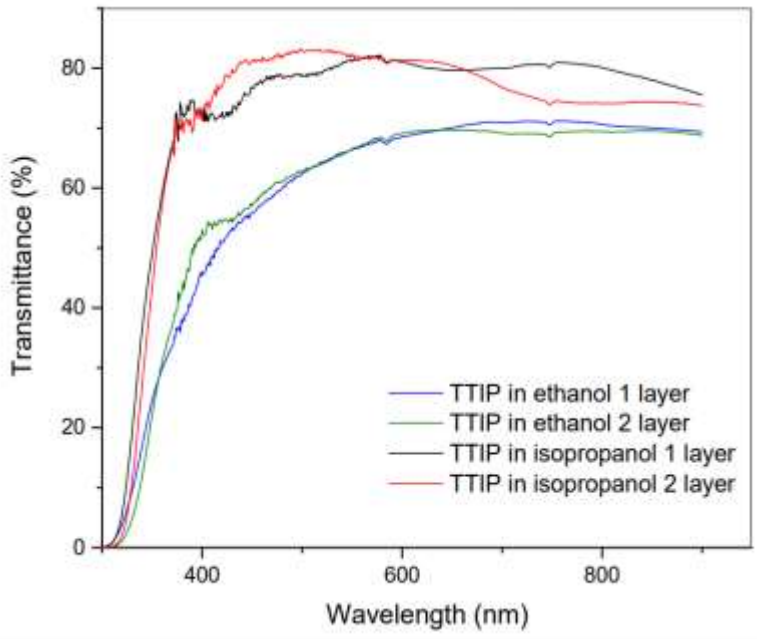

Figure 78. Transmittance measurements on FTO solutions in various solvents and with varying numbers of layers at the same concentrations.

We perform images of TiO_2 thin films synthetized with TTIP with or without the addition of AcacH at different molar ratios obtained using atomic force microscopy (AFM). In general, it is possible to see that when acetylacetone is present in the precursor solution the surface of the thin film becomes flatter, smoother, and more uniform.

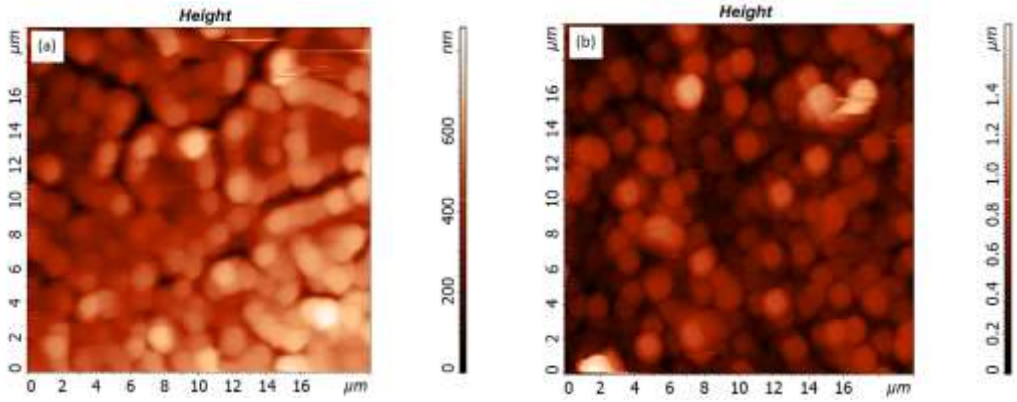

Figure 79. AFM pictures of (a) solution 1M 1 layer no AcacH, (b) solution 0.3 M 1 layer with AcacH.

We have fabricated photovoltaic cells with such a layer but with limited results. The humidity level during spin coating has a significant impact on the TiO_2 structure and hence the device performance. This simply means that process parameters like RH and temperature must be regulated throughout the manufacturing of these devices.

For this reason, the realization of a good performing TiO_2 layer is very tricky and investigation needs to be further implemented in the future.

Chapter VI
Conclusions

This thesis work aimed to investigate and study the synthesis parameters of a low cost processed CZTS-based photovoltaic cell and with their optimization to improve conversion performances by a deep understanding of the features of CdS/CZTS p/n junction. In particular, the current work contributes to our understanding of the non-vacuum, low-cost manufacturing of kesterite absorbers: the impact of CZTS production parameters such as drying time and annealing temperatures on the structure and optical properties are examined in detail.

In this work, CZTSSe thin films were prepared by spin coating technique by a non-vacuum process. Finished solar cells have been fabricated with the structure of SLG/Mo/CZTSSe/CdS/ZnO/ITO; different techniques have been used to confirm the nature of the compound and the morphology of the layers.

We developed a process while stabilizing it we encounter different issues: reproducibility of the devices, stabilization of the precursor solution, optimization of selenization, and the formation of secondary phases.

It is true that this is a low-cost procedure that does not use vacuum processes, but it needs fine-tuning to have acceptable reproducibility.
During the optimization steps it was seen that drying time and annealing temperature can affect the stoichiometry and morphology of the compound, generating secondary phases.
Faster drying periods lead to increased sulphur concentrations. In section 5.1 we have observed that three distinct types of samples with 3 different drying times (3, 5 and 10 minutes) have substantially dissimilar compositions after annealing, as shown by EDX analysis; the Raman analysis detected a shift in sulphur concentration, with a higher quantity for shorter drying durations. When drying time increases, the efficiency decreases dramatically. The intermediate drying period (5 minutes) has produced the best results, with an efficiency of over 5%. The calculated efficiency change considerably as the drying time increases. While the J-V curve for 10 minutes drying is characterized by a high series resistance, the efficiencies for 3 minutes of drying remain in the 3% region, marked by a low current density [62].
In addition to the CZTSSe phase, the Raman spectra revealed the $MoSe_2$ phase [64].

Regarding the influence of annealing temperature (topic addressed in section 5.2), the CZTSSe quality is improved by raising the selenization temperature, however, this can have distinct effects on the surface and bulk Se contents. It was found that one potential remedy is controlling the Se flow, during the annealing process, to make up for the Se loss at higher temperatures and Se surplus at lower temperatures (see section 5.3).

To increase the performance of the cell, in section 5.4 different elements have been used to dope the absorber layers using a unique and considerably easier method: the drop-casting of a chloride solution on the surface of the CTZS film.
Testing with different elements such as sodium, potassium, and germanium; the latter showed the greatest impact with larger crystallite, larger grain, lower Se incorporation, and higher carrier concentration, which ultimately explains the better efficiency.
An additional doping test was performed with a solution of cadmium chloride, this process is under patent pending.
This innovative and simpler method offers the advantage of easier industrialization.

The development of a new TiO_2 window layer discussed in section 5.5 has not yielded good results; this material is not easy to handle and would need more optimization, especially when applied in non-vacuum processes: the repeatability of device preparation and stability was assumed to be limited due to variances in preparation circumstances, relative humidity in fact during spin-coating of the TiO_2 precursor solution (TTIP, titanium isopropoxide) has a major impact on TiO_2 stability and morphology.

The process optimized in the lab, done during my PhD thesis, should be in future be transferred to the industrial level. This is not a trivial process since it requires to be extended at a large scale and with shorter processing times. The first thing that needs to be done is to transfer the spin coating process step to spray coating, which allows for homogeneous coating in large areas. Other process steps will need to be adapted, for example the annealing process, which is still very slow and it does not reach the required reproducibility.
In this sense we plan to introduce in the next months: 1) high frequency ultrasonic based spray deposition, 2) rapid thermal annealing with heating lamps, 3) graphite box as substrate holder in the oven with fixed position of Se sources and substrate plates.

Another variant to consider is to replace CdS, used as the window layer, with ZnS; which is a promising window layer for thin film solar cells. It is easily accessible less hazardous and it has a very good optical band gap.

List of Figures

List of Tables

List of Abbreviations

AcacH	acetylacetone
AFM	atomic force microscope
AST	accelerated stability test
BJTs	bipolar junction transistors
b.p.	boiling point
CBD	chemical bath deposition
CCB	cubic closed packed
CdS	cadmium sulfide
CdTe	Cadmium Telluride
CIGS	$Cu(In,Ga)Se_2$
CPS	centipoise
CTS	Cu_2SnS_3
CV	capitance voltage
CZ450	kesterite sample annealed at 450°C
CZ500	kesterite sample annealed at 500°C
CZ550	kesterite sample annealed at 550°C
CZTS	Cu_2ZnSnS_4
CZTSe	$Cu_2ZnSnSe_4$
CZTSSe	$Cu_2ZnSn(S,Se)_4$ an alloy of the previous two compounds
DEA	diethanolamine
DLCP	drive level capacitance profiling
DMSO	dimethyl sulfoxide
DPI	the unit of dynamic viscosity
DT03	drying time 3 minutes
DT05	drying time 5 minutes
DT10	drying time 10 minutes
EDXS	energy-dispersive x-ray spectroscopy
FTO	fluorine-doped tin oxide glass
IPA	isopropyl alcohol
IQE	internal quantum efficiency
ITO	Sn-doped In_2O_3

IV	current vs voltage
JV	current density vs voltage
MEA	ethanolamine
PCE	power conversion efficiency
PLD	pulsed laser deposition
PMCA	pre-mixed Cu-Au
PV	photovoltaics
QE	quantum efficiency
RF	radio-frequency
rpm	rounds per minute
SEM	scanning electron microscopy
SLG	soda lime glass
ST	stannite
TC	texture coefficient
TEC	FTO glass substrate
TIJ	thermal inkjet
TTIP	titanium isopropoxide
UV-Vis	Ultraviolet–visible spectroscopy
XRD	x-ray diffraction
ZnO	zinc oxide
ZnS	zinc sulfide

List of Symbols

AM	air mass coefficient
E	electric field
ε	permittivity
E_G	band gap energy
FF	fill factor
I_0	saturation current of the diode
I_L	light generated current
I_m	current at maximum power point
I_{sc}	short circuit current
J	current density
k_B	Boltzmann's constant
η	power conversion efficiency
N^+_D, N^-_A	ionized impurities concentrations
n_j	intrinsic carrier concentration
p, n	charge carrier densities
P_{max}	maximum power
q	fundamental unit of charge
ρ	charge density concentration
T	temperature
V	voltage
V_m	voltage at maximum power point
V_{oc}	open circuit voltage

List of Publications

- Analysis of the drying process for precursors of $Cu_2ZnSn(S,Se)_4$ layers by low cost non vacuum fabrication technique.
  *Prabeesh Punathil, Solidea Zanetti [1], Elisa Artegiani, Vikash Kumar, Alessandro Romeo**
  Solar Energy 224 (2021) 992–999 - https://doi.org/10.1016/j.solener.2021.06.063

- Analysis of environmentally friendly and low cost non vacuum process for $Cu_2ZnSn(S,Se)_4$ solar cells.
  *Prabeesh Punathil, Solidea Zanetti [1], Elisa Artegiani, Vikash Kumar, Alessandro Romeo**
  38th European Photovoltaic Solar Energy Conference and Exhibition

- Annealing temperature and post sulphurization/selenization effects on solution-based CZTS devices
  *Prabeesh Punathil, Solidea Zanetti [1], Elisa Artegiani, Vikash Kumar, Alessandro Romeo**
  37th European Photovoltaic Solar Energy Conference and Exhibition

- Analysis of selenization temperature for the performance improvement of spin coated CZTSSe solar cells.
  *Prabeesh Punathil, Solidea Zanetti[1], Elisa Artegiani, Narges Torabi and Alessandro Romeo**
  Proceedings of 8th World Conference on Photovoltaic Energy Conversion

- A simple method for Ge incorporation to enhance performance of low temperature and non-vacuum based CZTSSe solar cells.
  *Prabeesh Punathil, Elisa Artegiani, Solidea Zanetti [1], Luca Lozzi [2], Vikash Kumar, Alessandro Romeo**
  Solar Energy 236 (2022) 599–607 - https://doi.org/10.1016/j.solener.2022.03.027

- Method to enhance the kesterite solar cell performance.
  Inventors: Solidea Zanetti[1], Alessandro Romeo, Elisa Artegiani, Prabeesh Punathil.
  2021 - PATENT PENDING

LAPS-Laboratory for Applied Physics, Department of Computer Science, University of Verona, Ca' Vignal 1, Strada Le Grazie 15, 37134 Verona, Italy
* Corresponding author.
E-mail address: alessandro.romeo@univr.it (A. Romeo).
1 Also at Isopan S.p.A., via Giona 5, Trevenzuolo, Italy
2 Department of Physical and Chemical Sciences, University of L'Aquila, Via Vetoio, 67100 L'Aquila, Italy.

References

[1] Isopan website.

[2] S. , K. R. and W. S. Capstick, "Chapter 6. Bridging the gap: The role of equitable low-carbon lifestyles. In Emissions Gap Report 2020. United Nations Environment Programme. Nairobi.," 2020.

[3] S. , K. R. and W. S. Capstick, "Chapter 6. Bridging the gap: The role of equitable low-carbon lifestyles. In Emissions Gap Report 2020. United Nations Environment Programme. Nairobi.," 2020.

[4] https://opendevelopmentmekong.net/topics/sdg7-affordable-and-clean-energy e foto qui https://www.unep.org/explore-topics/sustainable-development-goals/why-do-sustainable-development-goals-matter/goal-7. https://opendevelopmentmekong.net/topics/sdg7-affordable-and-clean-energy e foto qui https://www.unep.org/explore-topics/sustainable-development-goals/why-do-sustainable-development-goals-matter/goal-7 (accessed Nov. 26, 2022).

[5] https://www.enerdata.net/publications/reports-presentations/world-energy-trends.html.

[6] p-n junction https://www.pveducation.org/pvcdrom.

[7] Semiconductor materials - https://www.pveducation.org/pvcdrom/pn-junctions/semiconductor-materials.

[8] S.M. Sze, *Semiconductor devices - Physics and technology* , 2nd ed. 2008.

[9] Band Gap - https://www.pveducation.org/pvcdrom/pn-junctions/band-gap.

[10] Doping - https://www.pveducation.org/pvcdrom/pn-junctions/doping.

[11] Cell operation - https://www.pveducation.org/pvcdrom/solar-cell-operation/light-generated-current.

[12] Poisson's Equation - https://eng.libretexts.org/Bookshelves/Materials_Science/Supplemental_Modules_(Materials_Science)/Solar_Basics/C._Semiconductors_and_Solar_Interactions/V._Equations_of_Device_Physics.

[13] Absorption of light - https://www.pveducation.org/pvcdrom/pn-junctions/absorption-of-light.

[14] https://www.britannica.com/technology/solar-cell.

[15] P. Sidi, D. Sukoco, W. Purnomo, H. Sudibyo, and D. Hartanto, "Electric Energy Management and Engineering in Solar Cell System," in *Solar Cells - Research and Application Perspectives*, InTech, 2013. doi: 10.5772/52572.

[16] T. Markvart and L. Castañer, "Principles of Solar Cell Operation," in *McEvoy's Handbook of Photovoltaics*, Elsevier, 2018, pp. 3–28. doi: 10.1016/B978-0-12-809921-6.00001-X.

[17] FF - https://www.pveducation.org/pvcdrom/solar-cell-operation/fill-factor.

[18] Image FF - https://ecowowlife.com/fill-factor-of-solar-cell/.

[19] Solar efficiency - https://www.pveducation.org/pvcdrom/solar-cell-operation/solar-cell-efficiency.

[20] Photovoltaic Cell Generations - https://encyclopedia.pub/entry/26456.

[21] NREL https://www.nrel.gov/pv/cell-efficiency.html.

[22] https://www.pveducation.org/pvcdrom/materials/cztsse#footnote1_b0xks60, "PVeducation."

[23] A. Khare, B. Himmetoglu, M. Johnson, D. J. Norris, M. Cococcioni, and E. S. Aydil, "Calculation of the lattice dynamics and Raman spectra of copper zinc tin chalcogenides and comparison to experiments," *J Appl Phys*, vol. 111, no. 8, p. 083707, Apr. 2012, doi: 10.1063/1.4704191.

[24] K. Pal, P. Singh, A. Bhaduri, and K. B. Thapa, "Current challenges and future prospects for a highly efficient (>20%) kesterite CZTS solar cell: A review," *Solar Energy Materials and Solar Cells*, vol. 196, pp. 138–156, Jul. 2019, doi: 10.1016/j.solmat.2019.03.001.

[25] G. Rey *et al.*, "Post-deposition treatment of Cu2ZnSnSe4 with alkalis," *Thin Solid Films*, vol. 633, pp. 162–165, Jul. 2017, doi: 10.1016/j.tsf.2016.11.021.

[26] I. D. Olekseyuk, L. D. Gulay, I. V. Dydchak, L. V. Piskach, O. V. Parasyuk, and O. V. Marchuk, "Single crystal preparation and crystal structure of the Cu2Zn/Cd,Hg/SnSe4 compounds," *J Alloys Compd*, vol. 340, no. 1–2, pp. 141–145, Jun. 2002, doi: 10.1016/S0925-8388(02)00006-3.

[27] D. M. Berg *et al.*, "Discrimination and detection limits of secondary phases in Cu2ZnSnS4 using X-ray diffraction and Raman spectroscopy," *Thin Solid Films*, vol. 569, pp. 113–123, Oct. 2014, doi: 10.1016/j.tsf.2014.08.028.

[28] M. Kumar, A. Dubey, N. Adhikari, S. Venkatesan, and Q. Qiao, "Strategic review of secondary phases, defects and defect-complexes in kesterite CZTS–Se solar cells," *Energy Environ Sci*, vol. 8, no. 11, pp. 3134–3159, 2015, doi: 10.1039/C5EE02153G.

[29] S. Z. E. A. V. K. and A. R. Prabeesh Punathil, "Annealing temperature and post sulphurization/Selenization effects on solution-based CZTS devices," in *37th European Photovoltaic Solar Energy Conference and Exhibition*, 2020.

[30] H. Skliarova *et al.*, "Medical Cyclotron Solid Target Preparation by Ultrathick Film Magnetron Sputtering Deposition," *Instruments*, vol. 3, no. 1, p. 21, Mar. 2019, doi: 10.3390/instruments3010021.

[31] D. Depla, S. Mahieu, and J. E. Greene, "Sputter Deposition Processes," in *Handbook of Deposition Technologies for Films and Coatings*, Elsevier, 2010, pp. 253–296. doi: 10.1016/B978-0-8155-2031-3.00005-3.

[32] Spin coating - https://www.ossila.com/en-eu/pages/spin-coating .

[33] HSASystems, "https://www.hsasystems.com/products/thermal-inkjet-printers/minikey."

[34] Inkjet exemple-https://phys.org/news/2015-05-inkjet-kesterite-solar-cells.html.

[35] R. Cherrington and J. Liang, "Materials and Deposition Processes for Multifunctionality," in *Design and Manufacture of Plastic Components for Multifunctionality*, Elsevier, 2016, pp. 19–51. doi: 10.1016/B978-0-323-34061-8.00002-8.

[36] Dr Blade - https://www.ossila.com/pages/solution-processing-techniques-comparison.

[37] Dip coating - https://www.advancedcoating.com/blog/what-is-dip-coating.

[38] Dip coating - https://www.ossila.com/en-eu/pages/dip-coating.

[39] S. Z. E. A. N. T. and A. R. Prabeesh Punathil, "Analysis of selenization temperature for the performance improvment of spin coated CZTSSe solar cells," in *8th World Conference on Photovoltaic Energy Conversion* ,

[40] Annealing-https://www.twi-global.com/technical-knowledge/faqs/what-is-annealing.

[41] Annealing - https://thermcraftinc.com/working-principle-of-annealing-furnaces/.

[42] Elite Furnaces - https://www.elitefurnaces.com/eng/products/furnaces/1200%20Single%20Zone%20Tube%20Furnaces.php.

[43] https://serc.carleton.edu/research_education/geochemsheets/techniques/SEM.html.

[44] AFM Theory - https://www.afmworkshop.com/learning-center/atomic-force-microscopy.

[45] AFM - https://microbenotes.com/atomic-force-microscope-afm/.

[46] AFM- https://chem.libretexts.org/Bookshelves/Analytical_Chemistry/Physical_Methods_in_Chemistry_and_Nano_Science_%28Barron%29/09%3A_Surface_Morphology_and_Structure/9.02%3A_Atomic_Force_Microscopy_%28AFM%29.

[47] XRD - https://www.scimed.co.uk/education/what-is-x-ray-diffraction-xrd/.

[48] S. Seibt and T. Ryan, "Microfluidics for Time-Resolved Small-Angle X-Ray Scattering," in *Advances in Microfluidics and Nanofluids*, IntechOpen, 2021. doi: 10.5772/intechopen.95059.

[49] Raman - https://www.horiba.com/int/scientific/technologies/raman-imaging-and-spectroscopy/raman-spectroscopy/.

[50] Mettler Toledo - https://www.mt.com/au/en/home/applications/L1_AutoChem_Applications/Raman-Spectroscopy.html#:~:text=The%20Raman%20Spectroscopy%20Principle,elastic%20scattering%2C%20or%20Rayleigh%20scattering.

[51] S. Mosca, C. Conti, N. Stone, and P. Matousek, "Spatially offset Raman spectroscopy," *Nature Reviews Methods Primers*, vol. 1, no. 1, p. 21, Mar. 2021, doi: 10.1038/s43586-021-00019-0.

[52] Uv-Vis Agilent - https://www.agilent.com/cs/library/primers/public/primer-uv-vis-basics-5980-1397en-agilent.pdf.

[53] Image Electromagnetic spectrum - https://chem.libretexts.org/Bookshelves/Introductory_Chemistry/Map%3A_Introductory_Chemistry_%28Tro%29/09%3A_Electrons_in_Atoms_and_the_Periodic_Table/9.03%3A_The_Electromagnetic_Spectrum.

[54] UV Vis Spectrometer - The dual-beam UV-VIS spectrometer is shown schematically.

[55] PVeducation I-V - https://www.pveducation.org/pvcdrom/characterisation/measurement-of-solar-cell-efficiency.

[56] PVeducation - https://www.pveducation.org/pvcdrom/solar-cell-operation/quantum-efficiency.

[57] J. v. Li and G. Ferrari, Eds., *Capacitance Spectroscopy of Semiconductors*. Jenny Stanford Publishing, 2018. doi: 10.1201/b22451.

[58] S. Spataru, P. Hacke, and M. Owen-Bellini, "Combined-Accelerated Stress Testing System for Photovoltaic Modules," in *2018 IEEE 7th World Conference on Photovoltaic Energy Conversion (WCPEC) (A Joint Conference of 45th IEEE PVSC, 28th PVSEC & 34th EU PVSEC)*, IEEE, Jun. 2018, pp. 3943–3948. doi: 10.1109/PVSC.2018.8547335.

[59] S. A. Khalate, R. S. Kate, and R. J. Deokate, "A review on energy economics and the recent research and development in energy and the Cu2ZnSnS4 (CZTS) solar cells: A focus towards efficiency," *Solar Energy*, vol. 169. Elsevier Ltd, pp. 616–633, Jul. 15, 2018. doi: 10.1016/j.solener.2018.05.036.

[60] Kentaro Ito, *Copper Zinc Tin Sulfide-Based Thin-Film Solar Cells*. John Wiley & Sons, Ltd, 2015.

[61] Y. E. Romanyuk *et al.*, "Recent trends in direct solution coating of kesterite absorber layers in solar cells," *Solar Energy Materials and Solar Cells*, vol. 119, pp. 181–189, Dec. 2013, doi: 10.1016/j.solmat.2013.06.038.

[62] P. Punathil, S. Zanetti, E. Artegiani, V. Kumar, and A. Romeo, "Analysis of the drying process for precursors of Cu2ZnSn(S,Se)4 layers by low cost non vacuum fabrication technique," *Solar Energy*, vol. 224, pp. 992–999, Aug. 2021, doi: 10.1016/j.solener.2021.06.063.

[63] S. K. Karunakaran *et al.*, "Recent progress in inkjet-printed solar cells," *J Mater Chem A Mater*, vol. 7, no. 23, pp. 13873–13902, 2019, doi: 10.1039/C9TA03155C.

[64] S. Z. E. A. V. K. and A. R. Prabeesh Punathil, "Analysis of Environmentally Friendly and Low Cost Non Vacuum Process for Cu2ZnSn(S,Se)4 Solar Cells.," 2021, pp. 454–457.

[65] J. A. Silva *et al.*, "Improving front contacts of n-type solar cells," *Energy Procedia*, vol. 8, pp. 625–634, 2011, doi: 10.1016/j.egypro.2011.06.193.

[66] P. M. P. Salomé *et al.*, "Growth and characterization of Cu2ZnSn(S,Se)4 thin films for solar cells," *Solar Energy Materials and Solar Cells*, vol. 101, pp. 147–153, Jun. 2012, doi: 10.1016/j.solmat.2012.02.031.

[67] J. He, L. Sun, S. Chen, Y. Chen, P. Yang, and J. Chu, "Composition dependence of structure and optical properties of Cu2ZnSn(S,Se)4 solid solutions: An experimental study," *J Alloys Compd*, vol. 511, no. 1, pp. 129–132, Jan. 2012, doi: 10.1016/j.jallcom.2011.08.099.

[68] F. Liu *et al.*, "Kesterite Cu $_2$ ZnSn(S,Se) $_4$ Solar Cells with beyond 8% Efficiency by a Sol–Gel and Selenization Process," *ACS Appl Mater Interfaces*, vol. 7, no. 26, pp. 14376–14383, Jul. 2015, doi: 10.1021/acsami.5b01151.

[69] S. Ahn *et al.*, "Determination of band gap energy (Eg) of Cu2ZnSnSe4 thin films: On the discrepancies of reported band gap values," *Appl Phys Lett*, vol. 97, no. 2, p. 021905, Jul. 2010, doi: 10.1063/1.3457172.

[70] G. Altamura, M. Wang, and K.-L. Choy, "Improving efficiency of electrostatic spray-assisted vapor deposited Cu2ZnSn(S,Se)4 solar cells by modification of Mo/absorber interface," *Thin Solid Films*, vol. 597, pp. 19–24, Dec. 2015, doi: 10.1016/j.tsf.2015.11.027.

[71] M. Dimitrievska *et al.*, "Raman scattering quantitative analysis of the anion chemical composition in kesterite Cu2ZnSn(SxSe1−x)4 solid solutions," *J Alloys Compd*, vol. 628, pp. 464–470, Apr. 2015, doi: 10.1016/j.jallcom.2014.12.175.

[72] M. Grossberg, K. Timmo, T. Raadik, E. Kärber, V. Mikli, and J. Krustok, "Study of structural and optoelectronic properties of Cu2Zn(Sn1−xGex)Se4 (x = 0 to 1) alloy compounds," *Thin Solid Films*, vol. 582, pp. 176–179, May 2015, doi: 10.1016/j.tsf.2014.10.055.

[73] Z.-Y. Xiao *et al.*, "Significantly enhancing the stability of a Cu $_2$ ZnSnS $_4$ aqueous/ethanol-based precursor solution and its application in Cu $_2$ ZnSn(S,Se) $_4$ solar cells," *RSC Adv*, vol. 5, no. 125, pp. 103451–103457, 2015, doi: 10.1039/C5RA23015B.

[74] A. Khare, B. Himmetoglu, M. Johnson, D. J. Norris, M. Cococcioni, and E. S. Aydil, "Calculation of the lattice dynamics and Raman spectra of copper zinc tin chalcogenides and comparison to experiments," *J Appl Phys*, vol. 111, no. 8, p. 083707, Apr. 2012, doi: 10.1063/1.4704191.

[75] Doping: https://www.pveducation.org/pvcdrom/pn-junctions/doping.

[76] H. Katagiri, *Thin solid films - Cu2ZnSnS4 thin films solar cells*, vol. 480–481. 2005.

[77] B. H. Lee *et al.*, "Effect of Ge nanolayer stacking order on performance of CZTSSe thin film solar cells," *Mater Lett*, vol. 284, p. 128981, Feb. 2021, doi: 10.1016/j.matlet.2020.128981.

[78] Y. E. Romanyuk *et al.*, "Doping and alloying of kesterites," *Journal of Physics: Energy*, vol. 1, no. 4, p. 044004, Oct. 2019, doi: 10.1088/2515-7655/ab23bc.

[79] M. Neuschitzer *et al.*, "V_{oc} Boosting and Grain Growth Enhancing Ge-Doping Strategy for Cu $_2$ ZnSnSe $_4$ Photovoltaic Absorbers," *The Journal of Physical Chemistry C*, vol. 120, no. 18, pp. 9661–9670, May 2016, doi: 10.1021/acs.jpcc.6b02315.

[80] J. Li, H. Shen, J. Chen, Y. Li, and J. Yang, "Growth mechanism of Ge-doped CZTSSe thin film by sputtering method and solar cells," *Physical Chemistry Chemical Physics*, vol. 18, no. 41, pp. 28829–28834, 2016, doi: 10.1039/C6CP05671G.

[81] P. Punathil, E. Artegiani, S. Zanetti, L. Lozzi, V. Kumar, and A. Romeo, "A simple method for Ge incorporation to enhance performance of low temperature and non-vacuum based CZTSSe solar cells," *Solar Energy*, vol. 236, pp. 599–607, Apr. 2022, doi: 10.1016/j.solener.2022.03.027.

[82] G. Altamura, M. Wang, and K.-L. Choy, "Influence of alkali metals (Na, Li, Rb) on the performance of electrostatic spray-assisted vapor deposited Cu2ZnSn(S,Se)4 solar cells," *Sci Rep*, vol. 6, no. 1, p. 22109, Feb. 2016, doi: 10.1038/srep22109.

[83] J. Spiridonova, A. Katerski, M. Danilson, M. Krichevskaya, M. Krunks, and I. Oja Acik, "Effect of the Titanium Isopropoxide:Acetylacetone Molar Ratio on the Photocatalytic Activity of TiO2 Thin Films," *Molecules*, vol. 24, no. 23, p. 4326, Nov. 2019, doi: 10.3390/molecules24234326.

[84] T. D. C. Hobson *et al.*, "Isotype Heterojunction Solar Cells Using n-Type Sb_2Se_3 Thin Films," *Chemistry of Materials*, vol. 32, no. 6, pp. 2621–2630, Mar. 2020, doi: 10.1021/acs.chemmater.0c00223.

[85] L. J. Phillips *et al.*, "Current Enhancement via a TiO2 Window Layer for CSS Sb2Se3 Solar Cells: Performance Limits and High V_{oc}," *IEEE J Photovolt*, vol. 9, no. 2, pp. 544–551, Mar. 2019, doi: 10.1109/JPHOTOV.2018.2885836.

[86] AM - https://en.wikipedia.org/wiki/Air_mass_(solar_energy).

[87] Coffee ring - https://en.wikipedia.org/wiki/Coffee_ring_effect.